Analysis of in-cylinder processes of an internal combustion engine with direct-injection using high-speed laser diagnostics

Vom Fachbereich Maschinenbau
an der Technischen Universität Darmstadt
zur
Erlangung des Grades eines Doktor-Ingenieurs (Dr.-Ing.)
genehmigte

D i s s e r t a t i o n

vorgelegt von

Dipl.-Ing. Sebastian Heinrich Roman Müller

aus Seeheim-Jugenheim

Berichterstatter:	Prof. Dr. rer. nat. A. Dreizler
Mitberichterstatter:	Prof. Dr. rer. nat. V. Sick
Tag der Einreichung:	06.12.2011
Tag der mündlichen Prüfung:	20.01.2012

Darmstadt 2012

D17

Hiermit erkläre ich an Eides Statt, dass ich die vorliegende Dissertation selbstständig verfasst und keine anderen als die von mir angegebenen Hilfsmittel verwendet habe. Ich erkläre außerdem, dass ich bisher noch keinen Promotionsversuch unternommen habe.

Sebastian H. R. Müller

Bickenbach, den 06.12.2011

Faber est suae quisque fortunae.

APPIUS CLAUDIUS CAECUS,
CA. 340 BC - 273 BC

Contents

Nomenclature

This thesis combines the fields of physics, chemistry and mechanical engineering. As an overall consistent use of variables has not been feasible within the scientific disciplines some variables will be used multiple times. The Einstein summation convention was used when using lowercase latin indices $i,\ j,\ k$.

The convention of timing engine relevant phases in crank angle degrees (360°[1] equals one revolution) is used. The standard reference is top dead center (TDC) between the compression and expansion stroke and defined as 0° CA. BTDC references to events before top dead center (compression stroke) and ATDC events after top dead center, respectively.

Uppercase latin letters		**Unit**
A_L	Laminar flame area	m^2
A_T	Turbulent flame area	m^2
D_α	Binary diffusion coefficient	$\mathrm{m}^2 \,/\, \mathrm{s}$
E	Energy	J
E	Kinetic energy	$\mathrm{m}^2 \,/\, \mathrm{s}^2$
E_a	Activation energy	$\mathrm{J} \,/\, \mathrm{mol}$
E_e	Electronic energy of an atom / molecule	J
E_r	Rotational energy of an atom / molecule	J
E_v	Vibrational energy of an atom / molecule	J
G	Gain factor of intensifier	–
I	Intensity field	–
$I^{'}$	Displaced intensity field	–
$J_i^{Y_\alpha}$	mass flux vector	–
N_{cam}	Background noise	–
R	Universal gas constant	$\mathrm{J} \,/\, \mathrm{K\,mol}$
R_{II}	Correlation function	–
Re	Reynolds number	–
S_{pp}	Number of photons collected per pixel	$\mathrm{No.} \,/\, \mathrm{px}$
T	Temperature	K
T_{ij}	Deformation tensor	$\mathrm{N} \,/\, \mathrm{m}^2$

Lowercase latin letters		**Unit**
c	Speed of light	$\mathrm{m} \,/\, \mathrm{s}$
d_p	Droplet diameter	m
f_c	Resolved frequency	$1 \,/\, \mathrm{s}$

[1] Although not standard, the ° symbol is used synonymously to denote the crank angle degree.

g	Gravitational force	$\mathrm{kg\,m\,/\,s^2}$
h	Enthalpy	J
h	Planck's constant	$\mathrm{J\,s}$
k	Boltzmann-constant	$\mathrm{J\,/\,K}$
k	Turbulent kinetic energy	$\mathrm{m^2\,/\,s^2}$
l	Characteristic length scale	m
p	Pressure	$\mathrm{N\,/\,m^2}$
q_i	Heat flux vector	$\mathrm{W\,/\,m^2}$
s_L	Laminar flame speed	$\mathrm{m\,/\,s}$
s_T	Turbulent flame speed	$\mathrm{m\,/\,s}$
t	Time	s
u_f	Fluid velocity	$\mathrm{m\,/\,s}$
u_i	Velocity	$\mathrm{m\,/\,s}$
u_p	Particle velocity	$\mathrm{m\,/\,s}$
x_i	Position vector	m

Lowercase greek letters **Unit**

δ_{ij}	Kronecker delta	$-$
ϵ	Dissipation rate	$\mathrm{m^2\,/\,s^3}$
η	Efficiency of optical system	$-$
η_K	Kolmogorov length scale	m
κ	Wave number	$\mathrm{1\,/\,cm}$
λ	Air-to-fuel ratio to stoichiometry	$-$
λ	Heat conductivity	$\mathrm{W\,/\,m\,K}$
λ	Wavelength	m
μ	Dynamic viscosity	$\mathrm{Pa\,s}$
ν	Frequency	$\mathrm{1\,/\,s}$
ν	Kinematic viscosity	$\mathrm{m^2\,/\,s}$
ϕ	Equivalence ratio	$-$
ρ	Density	$\mathrm{kg\,/\,m^3}$
ρ_p	Droplet density	$\mathrm{kg\,/\,m^3}$
τ_K	Kolmogorov time scale	s
τ_s	Characteristic time	s
$\vec{\omega}$	Vorticity	$\mathrm{1\,/\,s}$

Abbreviations

ATDC	After top dead center
BBO	Beta barium borate
BDC	Bottom dead center
BMEP	Break mean effective pressure
BTDC	Before top dead center
CA	Crank-angle
CARS	Coherent anti-stokes Raman spectroscopy
CCD	Charge-coupled device
CCV	Cycle-to-cycle variations

CMOS	Complementary metal oxide semiconductor
COV	Coefficient of variation
DISI	Direct-injection spark-ignition
EGR	Exhaust gas recirculation
FMEP	Friction mean effective pressure
FOV	Field of view
HS-IRO	High-speed interrelay optics
IMEP	Indicated mean effective pressure
LDV	Laser Doppler Velocimetry
LIF	Laser-induced fluorescence
MCP	Multi-channel plate
Nd:YAG	Neodymium-doped yttrium aluminum garnet
Nd:YLF	Neodymium-doped yttrium lithium fluoride
Nd:YVO	Neodymium-doped yttrium orthovanadate
PIV	Particle image velocimetry
PLIF	Planar laser-induced fluorescence
SG-DISI	Spray-guided direct-injection spark-ignition
SNR	Signal-to-noise ratio
TDC	Top dead center
UV-PIV	Ultra-violet Particle image velocimetry

1 Introduction

1.1 Optimizing individual mobility in the 21st century

In a technological sense, individual mobility means the feasibility to move around the globe at ones own desire and potential. Commonly, this is done today either by plane, ship, or with an automobile. The main component of latter is a reciprocating internal combustion engine which is used in over 90% of todays cars, trucks, buses, etc. [1]. At the heart of a reciprocating internal combustion engine (in short "engine") is the transformation of chemically bounded energy into mechanical energy. The invention is attributed to Nikolaus Otto from 1876 [2]. This engine used a spark-ignited setup to which Rudolf Diesel in turn would invent his compression-ignition setup in 1892. Both inventions have revolutionized the socio-economic relationships of humans and transformed our local perception of one another to a global form. The access to goods and services from around the globe is readily available. World-wide travel, either mandatory (e.g. work related) or voluntary (e.g. vacation), is possible.

However, this technological breakthrough has also impacted human kind in a negative sense with which future generations are confronted. The reality of increasing global warming as well as the destructive exploitation of fossil fuels are topics of which no individual is deprived of. Here, modern societies have agreed [3] to regulate exhaust gas emissions (e.g. Euro VI) and to further decrease fuel consumption (e.g. using taxes). An alternative to the conventional internal combustion engine fueled with fossil fuels, would either be the electrification of the drivetrain or the use of renewable fuels (commercially known as ’biofuels’). Currently, a sustainable electrical energy conservation within a mass production vehicle measuring up to the range of a conventional gasoline engine is still in the research phase. Common auxiliary units such as a range-extender or hybrid-setups are available, but all require an internal combustion engine as the main drivetrain. Therefore, further development is required.

As mentioned above, an important topic in recent years has been the reduction of exhaust gas emissions, as the anthropogenic impact on the environment increases. With the introduction of the catalytic converter in the mid-1970s, which was introduced to conform to new political regulations, the development to "cleaner" engines is more prominent than ever. The revival of the direct-injection spark-ignition engine (invented in the 1920s) due to advanced injector designs and computer controls has become standard in recent years. Further, combining this with modern turbocharging, and downsizing concepts, new perspectives in regions of robustness, efficiency and power are feasible. Nevertheless, the in-cylinder processes remain complex and to increase the above traits the underlying physical and chemical processes need to be understood. The transient processes of the flow field, the mixing of fuel and air, as well as the combustion process need to be thoroughly investigated. The coupling of each individual process with the others is the main reason for the complexity.

1.2 Current developments within the field of research

This work is based on the research of physical and chemical processes in technical combustion facilities, as occur for example in gas turbines or internal combustion engines. The objective is to understand the underlying mechanisms for future development and optimization. Here, one aspect are experimental studies of the reactive flows in order to determine their characteristics. Common physical / chemical properties investigated are the flow field, the temperature distribution, or concentrations of distinctive species. The experiments are usually performed on atmospheric burners with a generic geometry and readily open access. Additionally, their stability of operation and reproducibility of the underlying physical and chemical interactions provide a basis for model validation in numerical simulations.

With the establishment of the first laser and subsequently detector setups about 50 years ago, the field of laser diagnostics has expanded ever since. The technological innovations since then have increased the readiness to more complex setups and more detailed understanding of basic physical and chemical processes has emerged. In order to characterize the processes within a flame, laser light is employed as a measuring tool. The main advantages are it's non-invasive[1], has a high spatial resolution because of the light coherence, and is available at a high temporal resolution because of ultra-short laser pulse sequences. Latter enables the recording of snap-shots of velocity fields of flow motions, temperature fields, and concentration distributions within the nanosecond to millisecond-range.

The temporal resolution is especially useful when investigating in-cylinder processes of an internal combustion engine. Instead of investigating only single crank angles during one engine stroke, the recording of whole crank angle ranges is beneficial for a more complete analysis. The ability to record the process history of multiple consecutive single cycles offers a more in-depth view into the cause-and-effect chains. The time-scales of flow and combustion characteristics are within the millisecond-range requiring an adequate temporal resolution to obtain reasonable contiguous results. Commonly, the recording frequency of laser diagnostics is < 50 Hz which suffices to record only a few images per cycle (six images at 50 Hz). Using high-speed[2] laser diagnostics enables the recording of the transient physics within the time range of the crank angle rate (at 1000 rpm one crank angle corresponds to a time-range of $166.\bar{6}\,\mu$s).

In order to preserve semi-realistic engine configurations, in-cylinder recordings are only possible with an optical access. Introducing a mechanical measuring sensor would alter the in-cylinder processes (e.g. temperature gradients). All materials with which light is guided either into or out of the engine show great weaknesses at high loads. The physical boundaries are set by the resistance of the materials towards high temperatures and pressures. Therefore, a compromise between realistic engine operation and maximum visibility of the in-cylinder processes is required.

One possibility is the use of endoscopes which are embedded into the cylinder head or liner. Laser light and the resulting signals are guided through them into / out of the combustion chamber. Another possibility is the separation of liner and cylinder head with a glass cylinder. This achieves maximum visibility, albeit also introducing the greatest discrepancy to a realistic engine. The

[1] 'Invasive' techniques indicate a reaction between the measured characteristic and the measurement equipment.

[2] The 'speed' of an excitation / detection system refers to the repetition rate at which it operates. The term high-speed therefore means operating the laser diagnostic components at high repetition rates, i.e. kHz or above.

temperature gradients between steel and glass effect the in-cylinder processes and create a semi-realistic environment. However, the underlying physical / chemical processes are similar and therefore this compromise presents the best trade-off and is used in this thesis.

Common practice in engine experiments combined with laser diagnostics is the isolation of individual physical processes during the engine cycle. This is done to decouple the processes as shown by Sick[3] [4]. Also, different laser wavelengths are employed to record different processes, hence the complexity of recording multiple processes simultaneously increases. In the following, the progress in recording and analyzing the physical / chemical processes during an engine cycle are briefly discussed.

Flow field analysis

The flow motion of the in-cylinder gaseous media (commonly air) influences the mixing behavior of fuel and oxidizer, the combustion process, and the emission of exhaust gases. To improve the efficiency of an engine for example, the effects of it have to be understood. Commonly, it is solely recorded during motored engine operation as no other influences (fuel injection or ignition) are present.

As shown by Rassweiler [5], the first optical recordings to understand the interaction between the flow field and the flame propagation within the cylinder were done in 1938. Since then a number of investigations have been undertaken to visualize and understand the physical fundamentals of the flow field and turbulence within the cylinder confinements. The method of choice is the use of particle image velocimetry (PIV) to gain a planar visualization of the flow motion in a single plane, hence the term "flow field". Albeit only a slice of the flow motion is visualized, the information about velocity direction and magnitude are mandatory quantities for an in-depth understanding.

Starting out in the early 1990's, Reuss [6, 7] investigated the flow field at low repetition rates resolving only one instantaneous velocity field per revolution. Already with only one velocity field per revolution, cyclic variations were noticeable. An improvement towards multiple velocity fields per cycle is presented by Stolz [8] who recorded velocity fields at 200 Hz with a movie camera. In a tedious evaluation process, the recorded images had to be transported from the photographic film with a CCD-camera onto computer hardware and then subsequently processed to obtain the velocity field.

Recording one velocity vector field per revolution of a single engine cycle can indicate the general flow motion but the more interesting part is the history of single flow attributes. Questions as to the formation of single vortices or kinetic energy / turbulence evolution arise. This is facilitated by the development of laser / detector systems with high repetition rates in the range of kHz, hence high-speed imaging. In the last decade, this section of laser diagnostics has presented the ability to record details of physical processes with time scales in the millisecond-range.

In an gasoline engine, Reeves [9] was one of the first to record the flow field at 9 and 13.5 kHz, respectively. The spatial resolution of 256 x 256 px and 128 x 128 px proved to be low, but still adequate to retrieve velocity vectors. In a subsequent publication, Towers [10] used this data to identify the frequency of the recorded eddies of the flow field. With the development of higher powered lasers and faster cameras, the spatial and temporal resolution has further increased. In

[3] In this thesis, only the first author of the publication is referenced, albeit multiple contributors are possible.

2006, cyclic variations were investigated by Jarvis [11] and Justham [12] who recorded the flow field at 10 kHz at an engine speed of 1500 rpm. The before mentioned investigations use laser light of 511 nm and 532 nm (visible range), but at around the same time, a different approach was used by Fajardo [13] who developed a UV-PIV system in which light at 355 nm was used to record the flow field at 16 kHz. This proves to be beneficial when simultaneously recording the combustion phase as the combustion luminosity is eliminated due to the shifted spectral range. An improvement in the size of the field of view was presented by Müller [14] by recording velocity fields with a Nd:YLF laser and a high-speed CMOS camera of a direct-injection, spark-ignition engine with spray-guided injection geometry. The large field of view of 44 x 43 mm recorded at 6 kHz presented single cycle velocity fields of about half the cylinder diameter. At the same repetition rate Fajardo [15] presented flow fields using the UV-PIV method.

These methods were also adapted to diesel engines as presented by Cosadia [16, 17]. Here, high-speed PIV flow fields were recorded inside a diesel engine setup with a Nd:YLF laser system. Particularly interesting is the choice of seeding, as the conventional oil evaporates due to higher in-cylinder temperatures. The analysis focused on cyclic variations of the swirl charge motion.

In addition to simply visualizing the flow field, statistical tools were adapted to characterize the data. These tools were especially used to compare single cycles and identify cycle-to-cycle variations as shown by Grafiteaux [18] and Müller [14]. Here, the kinetic and turbulent kinetic energy of the flow field was used to compare and differentiate single cycles and their respective energy level. This is also used by Ghandi [19], to quantify the turbulent kinetic energy and its evolution throughout single cycles. Another common statistical tool is the proper orthogonal decomposition (POD) shown by Vetèl [20], Druault [21], and Müller [14]. It decomposes the flow field into single energy portions. One main function of it is to filter the flow field as to extract the main flow field information. Further, the quantification of the turbulence properties has been a focus of research as presented by Reuss [22] and Funk [23].

Today, high-speed PIV in a single plane is a standardized setup configuration, although it can only record the in-plane flow velocities. More advanced setups employ multiple planes or stereoscopic recording to retrieve the out-of-plane velocity component. Grant [24] and Hinsch [25] give an overview of three-dimensional velocity recording techniques specializing on PIV. Brücker [26] was one of the first to attempt three-dimensional PIV using a drum scanner to record different planes at high repetition rates of 1 kHz inside a motored engine. In addition, Willert [27] and Prasad [28] presented a practical stereoscopic PIV system which is used predominately in modern setups. It uses the Scheimpflug criterion to minimize the magnification errors. In contrast, a multi-plane approach inside an engine is presented by Kapitza [29] and Guibert [30], although latter at low repetition speeds. Voisine [31] also uses the multi-plane approach to identify the vortex path produced by a tumble charge motion within the whole cylinder. A combination towards dual-plane stereoscopic PIV is shown by Mullin [32]. A further advancement and the leading edge of research is tomographic PIV shown by Elsinga [33] in which a three-dimensional fluid volume and its respective velocity field is obtained (albeit not in an engine). The experimental setup though is much more complex than conventional PIV and the field of view very limited for measurements inside an engine.

The work in this thesis employs a high-speed stereoscopic PIV approach to record consecutive flow fields of single cycles exhibiting all three velocity components in a single plane. With it, the influences of different charge motions as well as different engine speeds are investigated.

Fuel distribution analysis

The flow field recordings describe the flow motion within the cylinder. Coupled with the fuel injection, the distribution of fuel, and thus the mixing process can be investigated. The focus hereby is on identifying fuel accumulations and the local equivalence ratio. This helps to understand the combustion process and the origins of unburned hydrocarbons. Commonly, the method of choice is laser-induced fluorescence (LIF) to record the tracer signals inside the cylinder during motored operation. Other methods like absorption spectroscopy or e.g. Schlieren are also possible, but present the disadvantage of integrating the signal along the line-of-sight. A clear differentiation of single anomalies within the considered volume is therefore not feasible.

A non-fluorescing, substitute fuel (e.g. iso-octane) is doped with fluorescent tracer to record concentration gradients within the field of view. Common tracers are 3-pentanone, biacetyl, or toluene. Almost all tracers are influenced by the intake air, and therefore it is commonly replaced by nitrogen (thus adding to the semi-realistic environment). The reference paper of Schulz and Sick [34] gives an overview of the vast application abilities.

The most interesting region to record the fuel distribution is within the vicinity of the spark plug. Here, the flammability limits of the mixture are important as they determine the stability of the engine operation. As shown by Kuwahara [35] and Frieden [36], the fuel distribution at low repetition rates was recorded for single cycles. However, high-speed imaging is also feasible as presented by Smith [37, 38], but exact quantification of the signal intensities is still problematic as shown by Gordon [39] and Weber [40].

Further investigations were done by Gold [41] who presented a cross section of the in-cylinder air / fuel mixing. Einecke [42] combined the analysis of the fuel concentration and equivalence ratio with the measurement of the temperature. Williams [43, 44] and Stevens [45] investigated the requirements of a multi-component fuel which was more similar to regular fuel for LIF investigations. Quantitative results have been shown at low repetition rates. Measuring the air / fuel ratio in the vicinity of the spark, Grosch [46] developed a spark plug fitted with an endoscope with which near-infrared signals are recorded. In a post-processing application the equivalence ratio within the vicinity of the spark plug can be determined.

The work presented here shows the ability to record fluorescent signals with a standard multi-component reference fuel at high repetition rates without additional tracer. In contrast to the previous mentioned investigations, the focus of this work was on the spatial fuel distribution and additionally, single cycle evolutions of liquid fuel films on top of the piston are analyzed.

Combustion process analysis

The culmination of each engine cycle is the combustion process at the end of the compression stroke. It denotes the conversion of the chemically bounded energy of the air / fuel mixture in a high pressure and temperature environment into mechanical energy. During the combustion, the location and propagation of the flame front (leading edge of the flame) are important characteristics to describe e.g. cycle-to-cycle variations (ccv) or engine parametric influences. The reaction kinetics are e.g. influenced by the before mentioned flow motion or fuel distribution, thus all isolated parts are coupled.

One possibility to characterize the flame inside the cylinder is to record the chemiluminescence generated by the chemically exothermic reaction of the combustion. This has been investigated by e.g. Merola [47], Aleiferis [48], Smith [49], and Fansler [50]. The main drawback is the integration of the signal along the line-of-sight. A clear analysis of single cycle variations (e.g. using the flame propagation speed) is not available. In contrast, using laser-induced fluorescence, the intermediate species in the flame front (OH-radical, NO, etc.) can be electronically excited by absorption. The subsequent spontaneous emission of light can be recorded in a single plane, with minimal superposition of chemiluminescence. Different species of the combustion process were investigated such as NO-radicals by Knapp [51] and OH-radicals by Suntz [52], Arnold [53], and Becker [54].

In recent years, high-speed imaging of OH-radicals has introduced the ability to mark the transient flame front as shown by Kittler [55], Nygren [56], and Hult [57]. The latter two citations presented the flame front inside a combustion engine using multiple dye lasers and retrieving eight consecutive images within one cycle. As presented in this work, the high-speed imaging of OH-radicals has been further developed and applied to image multiple consecutive cycles with a wide range of crank angles (also presented in Müller [58]).

Recording individual processes simultaneously

The isolation of the processes as described above has the benefit of employing an average complexity of the setup (one laser / camera setup only). However, the processes are coupled and the ability to simultaneously record the flow field and the combustion process offers further insight. For instance, the latter is required when calculating the flame propagation speed (recorded with LIF) without the influences of convection (flow field recorded with PIV).

In recent years, this also has been opted for high-speed applications as shown by recordings of e.g. the flow field and the flame front in atmospheric burner setups [59, 60, 61, 62, 63] and in engines [13, 64, 65, 66]. The main reason for this development is the need for high temporally resolved validation data and the readily availability of the diagnostical systems (abundance of laser / camera combinations). This development is certainly the future, albeit the recordings of single processes are worthwhile, as they for now, show a larger field of view (mainly due to limitations in laser power).

1.3 Concept and aim of this work

The focus of this work is on understanding the cause-and-effect chain as well as on investigating the origins of cycle-to-cycle variations of in-cylinder processes within a direct-injection spark-ignition internal combustion engine. According to the respective recording range, the in-cylinder processes were isolated in flow field, spray / flow field interaction, fuel distribution, and flame kernel development measurements. Each recording was analyzed for cyclic variations and influences onto the subsequent in-cylinder process. Especially the ability to record in-cylinder transients throughout multiple consecutive engine cycles with a single crank angle resolution is worth mentioning. The purpose of the recorded data is to assist in future engine developments and provide a validation data for numerical simulations.

This work is structured into five chapters covering basic principles of laser diagnostics and their adaptability to the research of in-cylinder processes. First, this motivational section presents reasons for the necessity to analyze in-cylinder processes of an internal combustion engine and the progress of this work over the last decades. Secondly, a brief overview of internal combustion engines (only main traits concerning this work), the underlying physical relations concerning reactive and non-reactive flows, and the experimental photo physical techniques used in this work are detailed in chapter two.

Chapter three presents the experimental setups. The research engine is discussed in detail, as well as the different laser / camera setups used for the measurements. The post-processing procedures and an error analysis of each setup are also presented.

In chapter four, the results of the before mentioned experiments are shown and discussed. They are arranged according to their individual recording range, which was focused on the in-cylinder processes during the compression stroke. First the flow field, secondly the spray injection (stratified operation), the fuel distribution and finally the combustion processes are investigated. During each measurement campaign, the engine parameters were altered to show crucial differences of the in-cylinder processes. This was particularly beneficial, as with the high temporal resolution, recording the cycle-to-cycle variations of each configuration was readily available. Statistical tools were used to analyze the single cycles and compare them to phase-averaged data.

Summarizing the work, chapter five closes with a discussion of future abilities to further advance the presented results.

2 Theoretical background and measurement methodology

This chapter presents a brief overview of the main traits of internal combustion engines, emphasizing on gasoline engines with direct-injection and spark-ignition. The main focus will be on the in-cylinder processes and possible variations thereof. Further, a concise description of reactive and non-reactive flows within the combustion cylinder will be given. Finally, the theoretical concepts of the techniques used for the measurements shown in chapter four are presented.

2.1 Internal combustion engines

2.1.1 Overview

Numerous classifications for internal combustion engines exist because of their vast operational readiness and the continued research and development for over 125 years. Different designs (reciprocating or rotary), fuels (gasoline, diesel, natural gas, or biofuels), number of strokes (four-stroke or two-stroke), kinds of mixture formation (carburation, port-fuel injection, or direct-injection) or different methods of ignition (activation energy provided externally with e.g. a spark-ignition or internally with a compression ignition) are some of the dominant traits [2]. This illustrates the broad span of developments and specializing on one configuration only provides partial insight, although the physical and chemical principles are similar.

Commonly, the method of ignition is used to part two main development branches, namely into spark-ignition and compression-ignition. The spark-ignition method requires an external energy input to ignite the air / fuel mixture within the combustion chamber (e.g. a spark plug used in modern gasoline engines). The compression-ignition method (e.g. diesel engines) requires a higher compression ratio to realize higher pressure and temperature environments in which the air / fuel mixture auto-ignites. The scope of this overview is on the functioning of a gasoline internal combustion engine, albeit much of the description is also valid for compression ignition engines.

Engine cycle phases

In general, all internal combustion engines convert chemically bounded energy into mechanical energy within the confinements of a cylinder. Focusing on conventional gasoline internal combustion engines with spark-ignition, the basis of this engine is a four-stroke cyclic reciprocating process. The course of events is shown schematically in figure 2.1 including the piston position (top dead center (TDC) means the piston is closest to the cylinder head, and reversed at bottom dead center

(BDC)) as well as the valve positions (open or closed). The first part of a single cycle revolution is called the intake stroke, in which the air / fuel mixture is drawn into the cylinder (when using an external mixture preparation). Subsequently, the compression stroke and the following expansion stroke are the main working phases which cause a reciprocating operation. In the latter phase, the chemically bounded energy is released by combustion, activated by an externally implicated activation energy (ignition). The final part of the four-stroke engine is the exhaust stroke which forces the burned gases out of the cylinder. Following it, the cylinder is filled with fresh oxidizer to restart the process.

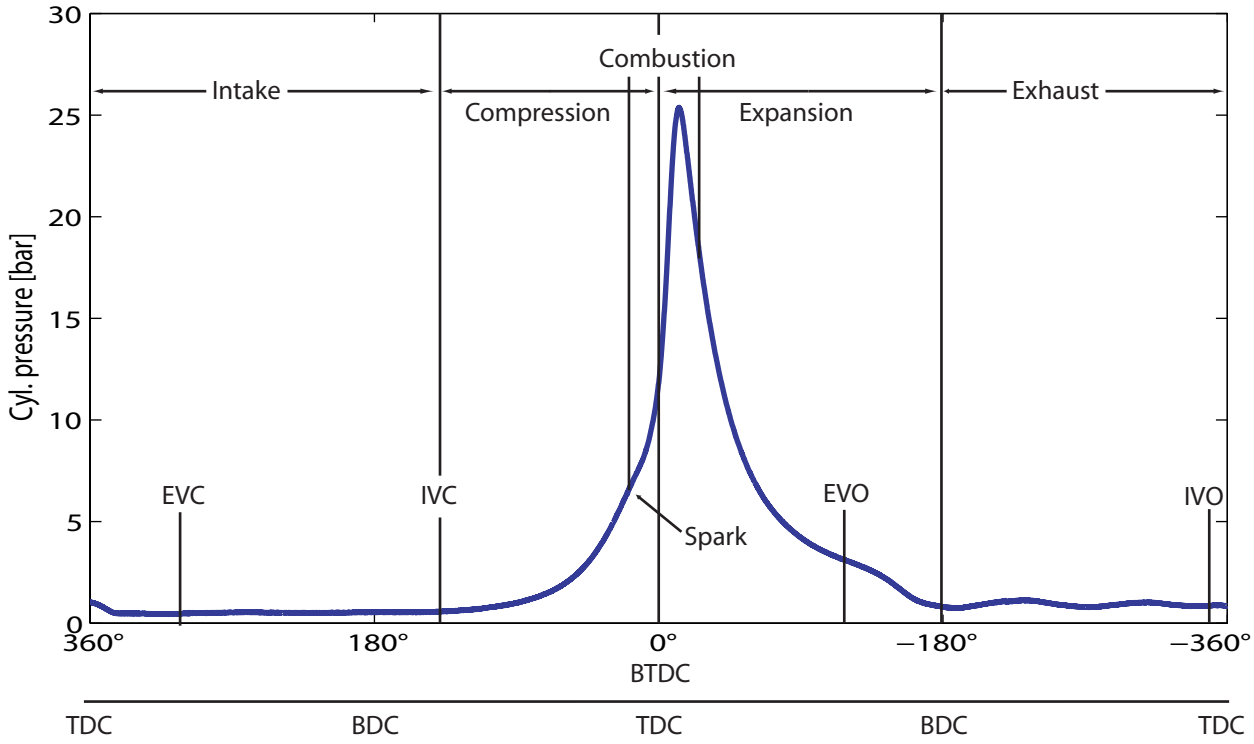

Figure 2.1: Sample pressure curve of the single cylinder engine used in the experiments with the individual strokes [2]. EVC: exhaust valve closing; IVC: inlet valve closing; EVO: exhaust valve opening; IVO: inlet valve opening.

For a sustainable operation of an engine two important features are required, the valves including their phase-locked timing and a moment of inertia for the displacement of the cylinder between exhaust and intake stroke supplied by a flywheel.

Charge motion variations

The fresh air introduced during the intake stroke can be guided to form a predefined flow pattern inside the cylinder. Distinctive flow patterns are also called charge motions. Figure 2.2 shows the common charge motions swirl (left) and tumble (right) and their dominant flow directions. Using e.g. a dual-manifold inlet system, the swirl charge motion is easily developed by closing one of the inlets. The cylindrical flow pattern ideally circles symmetrically with its axis of rotation parallel to the cylinder axis. This conditioning is predominantly used with compression-ignition combustion engines, where the circular drag imposed by the flow field deforms the single jets

produced by the multi-hole injector (conventionally used) and creates a homogeneous distribution of fuel avoiding hot spots. The tumble charge motion in turn is produced e.g. by closing the lower half of the dual-manifold inlet. A cut-off edge produces a non-uniform velocity profile inside the inlet pipes. The velocity distribution at the edge of the intake valves is thus asymmetrical which in consequence forces the production of a tumble charge motion resulting in a large tumbling vortex within the combustion chamber. The axis of the tumble motion is commonly parallel aligned to the crankshaft.

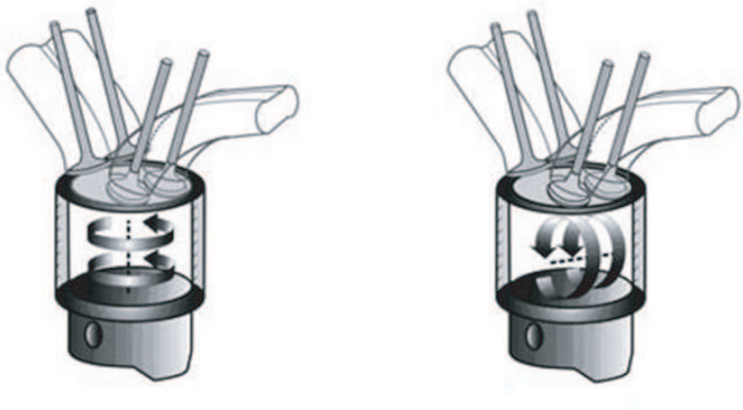

Figure 2.2: Charge motions inside a combustion chamber; swirl charge motion (left), tumble charge motion (right) [67].

Cycle-to-cycle variations (ccv)

During the operation of an internal combustion engine, consecutive cycles are not identical to each other and the variations have been the focus of several studies in which the cause-and-effect chain is the primary object of interest. The cyclic variations are noticeable for instance using the pressure curve shown in figure 2.1 in which each cycle exhibits slightly different gradients. The location of the peak (relatively in time) and center of 50% mass fraction burned of consecutive cycles can also be used to characterize the variations. Their origins is based on multiple characteristics but most prominently on in-cylinder fluctuations of the flow field, the mixture preparation, and flame propagation. The complexity of these processes makes an isolated inspection and characterization necessary, albeit difficult.

The importance of understanding cyclic variations is two-folded. First, the spark timing is determined for the average cycle. Cycles in which the flame propagation is faster or slower than the average speed produce less power and reduce the efficiency. Secondly, cyclic variations limit the engine operation as the fastest burning cycles tend to knock [2]. The slower burning cycles limit the engine operation as they may burn incompletely producing excess amounts of exhaust gas emissions.

2.1.2 IC Engines with direct-injection and spark-ignition

Significant to each internal combustion engine is the formation of the air / fuel mixture. The injection system of gasoline engines has undergone several developments, the most modern and actively used being the direct-injection of fuel into the combustion chamber. The direct-injection system is an advancement to the conventional port-fuel injection and carburetor systems because of its controllability of the mixture preparation while simultaneously increasing the power output. This overview was written combining the literature of Zhao [68], Bauer [69], and Spicher [70].

Technologically, the preparation of the air / fuel mixture can be divided into external and internal preparation. In contrast to the internal direct-injection of fuel into the combustion chamber, the mixture of fuel and air can be prepared within the intake system (externally). Commonly, a carburetor would be used in which the air and fuel flow is combined within the intake manifold. A throttle valve defines the mass flows of air and fuel. During high loads, the throttle valve is open, while during low- and mid-loads pressure losses occur and the overall efficiency of the engine is reduced. To compensate the pressure losses and obtain more controllability of the injected fuel amount, the port-fuel injection system directly injects the fuel into the intake manifold. In contrast to the carburetor, the port-fuel injection dominantly uses an electronically controlled injection system. A low-pressure fuel system is required to inject the discrete amounts of fuel. To ensure a stable mixture within flammability limits, the intake air is heated for example by heat exchange with the exhaust gas (also used with a carburetor). During start-up of the engine the evaporation of fuel is retarded and deposits within the manifold result. Further, the port-fuel injection is of slow response to changing engine loads because of the increased residence time of the fuel inside the manifold inlet. These drawbacks are eliminated with the direct-injection of fuel into the combustion chamber, albeit creating new difficulties detailed in the following.

Direct-injection system

The direct-injection of fuel into the combustion chamber enables a more direct link between the injection and distribution of the fuel within the cylinder. The precise fuel amount, the injection timing as well as the spray dispersion is controllable. The benefits are a reduced fuel consumption, high power output and reduction of exhaust gas emissions (e.g. with multiple injections). Compared to the foregoing techniques, this requires a high-pressure injection system (e.g. 100 - 200 bar), an improved injection nozzle, and a more complex cylinder head geometry.

The direct-injection is able to produce two different injection forms, the homogeneous and stratified injection. At high loads ($\sim$50% of the operational time), the homogeneous injection is required to generate the power output. The fuel is injected early during the intake stroke and ample time between injection and ignition produces a homogeneous mixture of fuel and air (see figure 2.3). At low- to mid-loads however, the injection timing is shifted into the compression stroke and a stratified mixture is produced. Only a small amount of fuel is injected into the decreased cylinder volume. In the vicinity of the spark plug the mixture has to be within the ignitability limits. The fuel is refrained from spreading because of the small amount and the increased gas densities due to pressure increase. Hence, a compact air / fuel mixture is produced. The rest of the cylinder is filled with air making an overall air / fuel equivalence ratio of over 5 feasible.

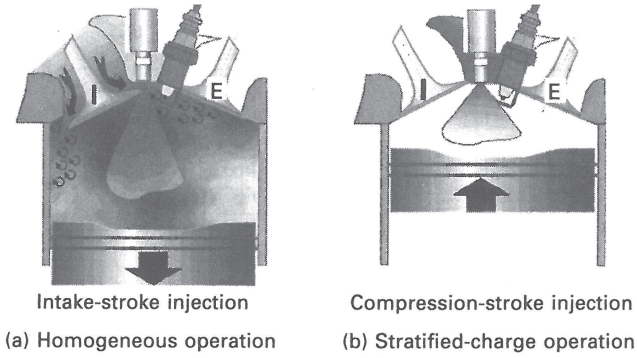

Figure 2.3: Injection modes of a DISI IC Engine [69].

The stratified fuel injection strategies are prone to a strong interaction with the in-cylinder flow field. With respect to the variable position of the fuel injector and the geometric shape of the piston crown, three different combinations of fuel spreading are possible. Figure 2.4 illustrates the different fuel distributions and their trajectory within the cylinder. On the left, the wall-guided method uses the piston crown to direct the fuel towards the spark plug which is positioned centrally in the cylinder head. This method is prone to wall-wetting leading to high concentrations of unburned hydrocarbons since the liquid film on top of the piston crown cannot fully evaporate before ignition. In the middle, the air-guided method is shown which requires a preconditioned in-cylinder air flow to guide the ignitable mixture towards the spark plug. The reproducibility of the flow guidance is not stable and therefore misfires can occur. Both of these methods require defined piston crown geometries. The third alternative on the right is the spray-guided injection which requires a well developed, reproducible spray injection even with changing in-cylinder conditions (pressure / flow field). The ignitability limits of the air / fuel mixture within the vicinity of the spark plug are the main factors constricting a stable operation. Wall-wetting is an unwanted aspect during early injection times within the intake stroke, but is significantly reduced opposed to the other options.

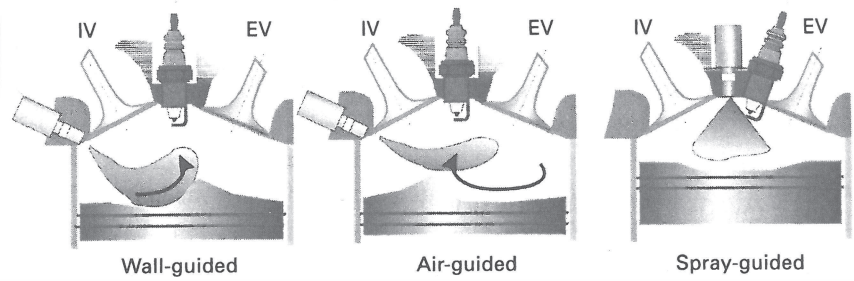

Figure 2.4: Combustion modes with a DISI engine; wall-guided (left), air-guided (middle), spray-guided (right) [68].

Three different injector types are commonly used in direct-injection systems. First, the spray shape of a multi-hole injector can be described as multiple solid-cone spray legs. The number, the orientation of the spray legs as well as the hole diameter are the main traits characterizing the injector. Secondly, the swirl injector produces a solid-cone spray superimposed with a circular motion. Third, the annular orifice produces an annular ring-formed hollow-cone spray shape. The

benefit is the large area covered to optimally distribute the fuel inside the cylinder. Additionally, the annular orifice injector is commonly operated with a piezo-electric stack (opposed to the magnetic needle system) enabling very short injection timings. Example images of the spray shapes are shown in section 4.2

2.1.3 Conventional engine diagnostics

Conventionally, the in-cylinder pressure and outside temperature of an internal combustion engine are measured. The in-cylinder pressure is determined using piezoelectric pressure transducers in which a quartz crystal transforms the pressure (force) into an electric signal. It is referenced to a known pressure. The assumption of homogeneous pressure levels throughout the cylinder is made. To ensure no temperature influences the quartz crystal is heated to a constant level.

An important value, which is calculable with the in-cylinder pressure, is the efficiency of the engine. It is defined by the mean effective pressure and the engine speed. The mean effective pressure is calculated by integrating over the pressure signal of the complete cycle and results in a single value. It is further divisible into break mean effective pressure (BMEP), indicated mean effective pressure (IMEP), and friction mean effective pressure (FMEP) [2]. These values can be calculated during the online operation, ensuring the reproducibility of the engine settings. Additionally, the wall-heat losses which occur due to the heat flux of the liner are calculable with the pressure curve. Common models used include the Woschni [71], Bargende [72], and Hohenberg [73] models. The main aim here is to provide an insight to the in-cylinder heat conversion and produce reliable simulation tools [2].

For more details and further reading about internal combustion engines, the reader is referred to Heywood [2], List [74], and Basshuysen [71].

2.2 Reactive and non-reactive flows

The field of reactive and non-reactive flows is as vast large as the earlier described field of internal combustion engines. Therefore, this sub-chapter focuses on describing the general in-cylinder flow characteristics within the confinements as well as the combustion process. Here, isolating single physical aspects of the in-cylinder processes contributes to a better understanding of their specific characteristics. First, the flow field is briefly discussed as well as the quantitative measures used to describe it. Subsequently, the combustion process is discussed. The following sections were prepared using mainly Spurk [75], Pope [76], Lumley [77], and Warnatz [78].

2.2.1 General characterization

In fluid dynamics the term flow field comprises the motion of a medium (liquid or gaseous) within predefined boundaries. To further characterize it, the Reynolds number Re (equation 2.1) is used to divide the flow regime into laminar and turbulent flows.

$$Re = \frac{\rho\, u^2}{\mu\, {}^{u}/_{l}} = \frac{lu}{\nu}. \tag{2.1}$$

The values u (characteristic velocity of the flow) and l (characteristic length scale) are geometrically influenced, the kinematic viscosity ν is dependent on the medium and temperature which is considered. The physical effects can be described as the ratio between the inertia forces ρu^2 and the viscous forces $\mu u \,/\, l$. It is a ratio between destabilizing (inertia forces) and stabilizing (viscous term) forces of the flow structure.

The Reynolds number itself does not qualify as a differentiation criterion between laminar and turbulent as the flow structures are mainly dependent on the considered geometry (e.g. in basic pipe flows, the flow fields below a Reynolds number of 2000 are considered laminar and above 3000 fully turbulent). Still, the two regions can be separated because of their different momentum transport characteristics. In the lower region (i.e. laminar flows) the momentum transport is dominated by diffusion processes. Above a certain Reynolds number, the chaotic, pseudo-random motions of the flow dominate its progression. Increasing only the flow velocity substantially increases the strain rate and thus perturbations within the flow are the origin of turbulent structures [77]. These structures are dominated by three-dimensional convective momentum transport. The main effect of turbulence in reactive flows used in practical combustion systems is the increased intensity of the miscibility of fuel and oxidizer as well as the wrinkling of the flame structure. These increase the efficiency of the combustion and reduces pollutants.

At a closer look, the transfer of energy in turbulent flows from large scale structures through vortex stretching to viscous dissipation is an important aspect. A common illustration of this process is the energy cascade (figure 2.5) which depicts the turbulent energy spectrum $E(\kappa)$ as a function of the wave number κ [77]. The energy of the large scale structures is transferred onto smaller structures as they subsequently break down due to the increased strain rate. Following the energy cascade, the energy is transferred through an inertial subrange region which is characterized by the scaling factor of $\kappa^{-5/3}$. The dissipation range is dominated by viscous effects in which the kinetic energy of the small scale flow structures is dissipated into thermal energy.

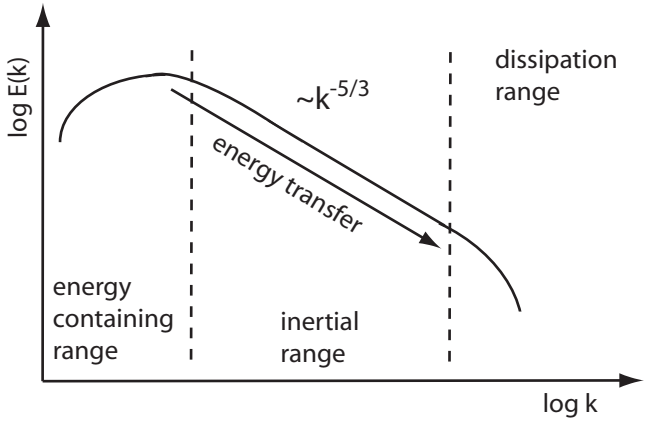

Figure 2.5: Energy cascade.

The time and length scales of the small scale flow structures within the dissipation range of the energy cascade are important. They determine the rate at which the energy supplied by the larger scale motion is dissipated. The production and dissipation rate should be equal within the small scale structures. A common ansatz is to link the dissipation rate ϵ ($\mathrm{m^2\,s^{-3}}$) per unit mass and the kinematic viscosity ν ($\mathrm{m^2\,s^{-1}}$) to form characteristic scales, the Kolmogorov scales. The Kol-

mogorov length scale η_K and the corresponding time scale τ_K are given in equation 2.2:

$$\eta_K = \left(\frac{\nu^3}{\epsilon}\right)^{\frac{1}{4}} \quad \text{and} \quad \tau_K = \left(\frac{\nu}{\epsilon}\right)^{\frac{1}{2}}. \tag{2.2}$$

Conservation laws

Regardless of the degree of turbulence within the flow field, the motion of mass, momentum, and heat are conserved. The first conservation law describes the balancing of mass of an arbitrary control volume within the flow field and is called the "continuity equation". Equation 2.3 presents the differential form of the continuity equation for such a control volume. The temporal change of the density ρ corresponds to the spatial derivative of the mass fluxes (convective transport with the velocity u_i) according to:

$$\frac{\partial \rho}{\partial t} + \frac{\partial \rho u_i}{\partial x_i} = 0. \tag{2.3}$$

This relation holds for both incompressible and compressible flows. Incompressible flows are characterized as a divergence-free fluid-velocity-field due to the relationship of ${}^{\partial \rho}/_{\partial t} = 0$. In this thesis, this assumption is not valid, as the pressure and temperature inside the engine cylinder are constantly changing.

According to Newton's laws of motion, the second conservation law is based on the conservation of momentum within the control volume. It can only be changed by external forces. Equation 2.4 explains the connection between the different forces:

$$\frac{\partial \rho u_i}{\partial t} + \frac{\partial \rho u_i u_j}{\partial x_j} = -\frac{\partial p}{\partial x_i} + \frac{\partial T_{ij}}{\partial x_j} + \rho g_i. \tag{2.4}$$

The local change of momentum ${}^{\partial \rho u_i}/_{\partial t}$ and the convective transport of momentum ${}^{\partial \rho u_i u_j}/_{\partial x_j}$ are equal to the sum of all external forces. These are volumetric forces $-{}^{\partial p}/_{\partial x_i}$ and ρg_i which are due to pressure influences and the gravitational forces, respectively. The second term on the right ${}^{\partial T_{ij}}/_{\partial x_j}$ contains the deformation tensor T_{ij}. Given a Newtonian fluid, it can be expressed by equation 2.5:

$$T_{ij} = \rho\nu \left[\left(\frac{\partial u_j}{\partial x_i} + \frac{\partial u_i}{\partial x_j}\right) - \frac{2}{3}\frac{\partial u_k}{\partial x_k}\delta_{ij}\right]. \tag{2.5}$$

In this relation, the shear stress tensor of the Newtonian fluid is assumed to be linearly dependent on the strain rate tensor. Equations 2.4 and 2.5 form the Navier-Stokes equations.

In practical combustion facilities, the conservation of energy is an important aspect. A common quantity when describing reactive flows is the enthalpy h which is the sum of the internal energy and the displacement energy. As shown in equation 2.6, the change over time and space is equal to viscous heating as well as heat flux over the boundaries of the control volume.

$$\frac{\partial}{\partial t}(\rho h) + \frac{\partial}{\partial x_i}(\rho h u_i) = T_{ij}\frac{\partial u_i}{\partial x_j} + \frac{Dp}{Dt} - \frac{\partial q_i}{\partial x_i}. \tag{2.6}$$

The heat flux vector q_i (equation 2.7) is the sum of heat conduction due to the temperature gradient $^{\partial T}/_{\partial x_i}$ (Fourier's law) and species diffusion $\sum_{\alpha=1}^{N_s} h_\alpha \, J_i^{Y_\alpha}$, when using multiple components. The constant λ is the thermal conductivity. Further, the mass flux vector $J_i^{Y_\alpha}$ relates the mass flux (Fick's law) to the gradient of the species mass fraction including the binary diffusion coefficient D_α.

$$q_i = -\lambda \frac{\partial T}{\partial x_i} + \sum_{\alpha=1}^{N_s} h_\alpha \, J_i^{Y_\alpha} \quad \text{with} \quad J_i^{Y_\alpha} = -\rho \, D_\alpha \frac{\partial Y_\alpha}{\partial x_i}. \tag{2.7}$$

Finally, equation 2.6 neglects the volumetric enthalpy sources (e.g. radiation) which are negligible in this work.

2.2.2 Quantitative description

Kinetic energy

The kinetic energy is a quantitative measure to differentiate between levels of turbulence and the general flow energy. It uses the Reynolds decomposition shown in equation 2.8 to separate the velocity $\bar{u}_i$ from the fluctuation $u_i^{'}$. It can also be used to compare different flow patterns, namely large coherent vortex structures to smaller, more diffusive flow structures. The subscript i denotes the direction of the velocity in Cartesian coordinates.

$$u_i = \overline{u}_i + u_i^{'}. \tag{2.8}$$

The kinetic energy E is defined in equation 2.9 and the turbulent kinetic energy k in equation 2.10 [21].

$$E = \frac{1}{2} \, u_i \, u_i \tag{2.9}$$

$$k = \frac{1}{2} \, \overline{u_i^{'} \, u_i^{'}}. \tag{2.10}$$

In general, the more small scale flow structures the lower the kinetic energy and vice versa. In turn, uniform large scale flow structures present higher kinetic energy levels.

Vortex identification

Defining and identifying vortices is important since they determine the transport processes in a turbulent flow. The vorticity $\vec{\omega}$ is defined as the curl of the velocity field (equation 2.11):

$$\vec{\omega} = \nabla \times \vec{u}. \tag{2.11}$$

The location of the vortex center (e.g. tumble structure) and its path within the cylinder help to analyze cyclic fluctuations. The vortex center can be identified by its maximum of vorticity and

distinctly lower velocities in its center than the rest of the vicinity [18]. Other identification algorithms include the λ_2-method by Jiong [79] or the use of imaginary values as proposed by Adrian [80]. These methods were investigated but the conventional method using the curl of the flow field sufficed the requirements.

2.2.3 Combustion

Reaction kinetics

The internal combustion engine relies on the chemical reaction of fuel and oxidizer to produce thermal energy. A requirement for a successful combustion process is the mixing of oxidizer (i.e. air) and fuel (natural gas, liquid (e.g. oil and derivatives thereof), or solid (e.g. pulverized coal)). The primary fuels of internal combustion engines are gasoline and diesel fuel. Commonly, gasoline requires an external activation energy input (i.e. spark-ignition) whereas diesel fuel is used in auto-ignition engines (also possible with homogeneous-charge compression-ignition engines). When operating an IC engine, the air number λ (in gas turbine environments also known as the equivalence ratio ϕ) is used to classify the air / fuel ratio. It is defined in equation 2.12 with $\left({}^{F}/_{A}\right)_{actual}$ as the actual fuel-to-air ratio and $\left({}^{F}/_{A}\right)_{s}$ as the stoichiometric fuel-to-air ratio depending on the used fuel:

$$\lambda^{-1} = \phi = \frac{\left({}^{F}/_{A}\right)_{actual}}{\left({}^{F}/_{A}\right)_{s}}. \tag{2.12}$$

With λ values above 1, more oxidizer than fuel is present which is called a "lean mixture". Values below 1 present an abundance of fuel, thus making the mixture "rich" and in turn producing e.g. unburned hydrocarbons and other unwanted by-products. A stoichiometric combustion is achieved with an air number / equivalence ratio of 1. Both mass portions of fuel and oxidizer are completely transformed into thermal energy. The fuel-to-air ratio on a molecular level for a stoichiometric combustion process using gasoline is $\sim$14.5 [71]. At high-load operation, the desired equivalence ratio is 1 (perspective of the exhaust gas aftertreatment), but because of inhomogeneities of the fuel distribution, values higher are used which also result in reduced flame propagation speeds.

When operating a gasoline engine, the air / fuel mixture needs to be in its flammability limits within the vicinity of the spark plug when ignited. The energy required for successful ignition can be described using chemical reaction kinetics. In reality, gasoline consists of many different species, but in a first attempt, an elementary reaction model can be used to describe the chemical reaction. Equation 2.13 shows two reactants A and B as well as their reaction products C and D.

$$A + B \leftrightharpoons C + D. \tag{2.13}$$

The bidirectional arrow indicates a forward and backward reaction, but the main interest is the reaction rate and the enabling process. The forward reaction rate is shown in equation 2.14 which is dependent on the concentrations of the reactants A and B (c_A and c_B) as well as a coefficient rate factor k_f.

$$r_f = k_f \, c_A \, c_B. \tag{2.14}$$

The activation process and the subsequent self-perpetuating release of radicals requires an activation energy which can be modeled with the Arrhenius equation presented in equation 2.15. It balances the rate coefficient k_f of the chemical reactions to the temperature T and the activation energy E_a (R is the universal gas constant, A is a pre-exponential factor).

$$k_f = A\,T^n\,e^{-E_a\,/\,RT}. \tag{2.15}$$

In general, the activation energy of a conventional spark plug is between 30 - 150 mJ with a spark time of 0.3 - 1 ms [71]. The coupling of the transient temperature change within the cylinder and the changing ignition timings also influence the required activation energy, thus an ample initial energy release is required for stable operation.

Flame types

The combustion process can either be categorized using the mixture level of both reacting species or the interaction with the surrounding flow. Using the mixture level, three different flame types occur. Non-premixed flames are produced when oxidizer and fuel are mixed within the reaction zone. Premixed flames are produced when a previous molecular mixing before inflammation of oxidizer and fuel occurs, and the partially premixed flame exists as a transitional flame form. If the flow surrounding the flame is used in a categorical sense, both variants of non-premixed and premixed flames can each be sub-divided into laminar and turbulent flames.

The engine operation via port-fuel injection or direct-injection during homogeneous operation mode (at high loads) is primarily characterized by a homogeneous mixture of oxidizer and fuel on a molecular level, and therefore a premixed flame structure is formed. The advantage of premixed combustion is its higher efficiency, the controllability of the exhaust gas compositions, and the retarded formation of soot particles [78]. The disadvantage of a premixed combustion is the availability of large volumes of an ignitable mixture, which can lead to uncontrolled ignition (in engines this is known as "knocking"). A schematic of the premixed flame front is shown on the left side of figure 2.6. The characteristic profiles of the air / fuel mixture, the products, and the intermediate species is presented along the flame trajectory s. The three regions of a premixed flame are the preheating, the reaction, and the oxidation zone. In the first zone, the reactants are preheated by diffusion transport from the adjacent reaction zone. In the second zone, the main reaction forming the products and the transient intermediate species is shown. It is also characterized by the highest temperature gradients. The adjacent oxidation zone is dominated by slow chemical reactions and the peak temperature level. In general, the premixed flame propagates orthogonally to its iso-lines in opposite direction of the flame trajectory s at a characteristic laminar flame speed s_L. The laminar flame propagation speed is dependent of the air / fuel mixture, as well as on the surrounding temperature and pressure environment. It is effected by the surrounding flow motion. Especially if the surrounding flow is turbulent, the laminar flame propagation speed s_L can be used to calculate the turbulent flame propagation speed s_T as shown in equation 2.16.

$$s_T = s_L\,\frac{A_L}{A_T}. \tag{2.16}$$

In a basic perception, the ratio of the laminar flame area A_L to the turbulent flame area A_T denotes the increased flame area due to the wrinkling effects of the turbulent flow [78]. An explanation for

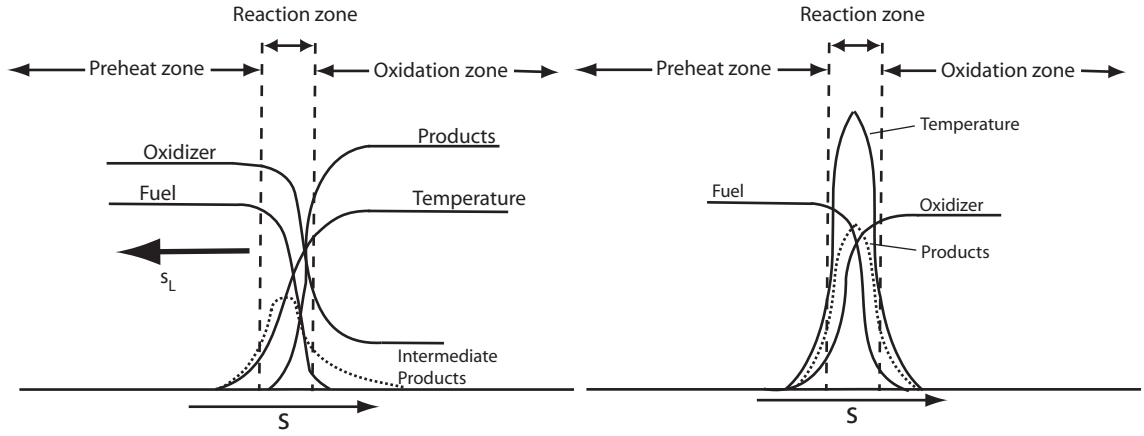

Figure 2.6: Illustration of a premixed flame front (left) at flame coordinate s and a non-premixed flame front (right). Characteristic profiles of different quantities like e.g. fuel and oxidizer concentration and temperature are shown.

a higher flame velocity within turbulent environments is therefore the larger area in which fuel and oxidizer can react. This is a vital correlation because without it higher engine speeds would not be possible. According to Heywood [2], the average laminar flame propagation of a vaporized liquid fuel is $\sim 2\,{}^{m}/_{s}$ (1 bar ambient pressure). Within the cylinder of an IC engine, this speed rises to $\sim 25\,{}^{m}/_{s}$ due to the surrounding turbulent flow. If this did not occur, the combustion process would cease at higher engine speeds because shorter time periods between intake, mixture preparation, combustion, and exhaust stroke are given.

Figure 2.6, right, shows the characteristic profiles of the non-premixed flame. In this case, the flame front is controlled by mixing processes due to diffusion. The fuel and oxidizer are introduced at opposing sides of the flame front where each is initially preheated. The peak temperature occurs within the reaction zone, as do the products. The equivalence ratio along the flame trajectory can have values between ∞ (fuel only) and 0 (oxidizer only). In contrast to a premixed flame, since both fuel and oxidizer are separated before combustion, the combustion systems are more secure towards uncontrollable ignition. In turn, the production of soot particles and unburned hydrocarbons is increased [78].

The distinct non-premixed flame is not formed during normal operation of a gasoline internal combustion engine with direct-injection. This is mainly due to the small time frame between injection and ignition, in which mixing takes place. Still, the partially non-premixed flame is formed during stratified operation, as the cylinder is divided into a part with fuel and a subsection without fuel. Assuming a central position of the injector, the injected fuel spreads inside a cylindrical volume smaller than the whole cylinder. The diffusion and convective transport processes produce a stratified mixture of air and fuel which needs to be within the flammability limits. However, the overall equivalence ratio ϕ of the partially non-premixed combustion can reach levels above the flammability limits and therefore be globally lean.

A side-effect of the late injection are occasional pool fires which occur when large portions of liquid fuel are burned e.g. on the piston crown. These are primarily also partially non-premixed flames.

Further information on combustion can be found in Peters [81] and Warnatz [78].

2.3 Laser-based diagnostics

2.3.1 Overview of methods

Light used as a measurement methodology embodies several advantages such as non-intrusiveness, high spatial resolution, and high time resolution. This introduces new possibilities in resolving physical processes especially in practical flames because of their high-temperature and fast-paced, transient environments. The measurable quantities are e.g. concentrations, number densities, and temperature. The latter being commonly measured with Coherent Anti-Stokes Raman spectroscopy (CARS) or Laser-induced Fluorescence (LIF). With CARS, the temperature dependent Boltzmann distribution of the ground state population and the vibrationally excited state population is used to obtain the temperature of a gaseous media (e.g. in flames). The LIF approach can use the perfect gas law to determine the temperature by dividing the pressure p over the total gas number density N_{gas} multiplied by the Boltzmann-constant k as shown in equation 2.17:

$$T = \frac{p}{N_{gas}\, k}. \tag{2.17}$$

Besides the pressure (pressure transducer is commonly used), the total gas number density can be determined by using the two-line fluorescence method. It measures the Stokes and anti-Stokes direct-line fluorescence of a known seeding supplement (e.g. NO or O_2) within the flame. The known mole fraction infers the total density. The errors which normally affect the measurements (e.g. collisional rates or trapping of photons) conveniently drop out because only the ratio of the two components is taken into account [82].

Another aspect is the measurement of number densities, as indirect methods like Laser Doppler Velocimetry (LDV) or Particle Image Velocimetry (PIV) depend on them. The elastic scattering of particles (Mie-scattering) is used to calculate the velocity within certain boundaries. In this sense, the time resolution[1] of these measurements is of special importance in IC engines. The time scales of single crank angles during the normal operating speed (e.g. at 1000 rpm each crank angle is ideally only $166.\bar{6}\,\mu$s long) is within the millisecond range. Therefore, to record velocities consecutively, the recording repetition rate is required to be of multiple kHz. The methods of LDV and PIV and their respective capability of resolving velocities in space and time is shown in figure 2.7.

The method of LDV / 3C-LDA can only resolve the velocity within one point over time presenting all three velocity components. The main benefit of this technique is the high time resolution based on the Doppler equivalent frequency-shift of the particles passing through the laser fringes. PIV, being a planar velocity measurement technique, can resolve two velocity components u_x and u_y within a single plane at one time instant. In recent years, the advances of higher repetition rates of e.g. all-solid state diode-pumped lasers and CMOS cameras has increased the temporal resolution towards multiple kHz, thus resolving processes within the millisecond scale [55, 83, 14]. Additionally, the use of multiple cameras to obtain the out-of-plane velocity component u_z results in the ability to fully present the desired velocity field in a single plane with PIV (namely three-component, two-dimensional PIV (3C / 2D-PIV) or stereoscopic PIV). To achieve the recording of

[1] The time resolution here means the repetition rate at which the velocity can be measured at a defined spatial point / area of interest.

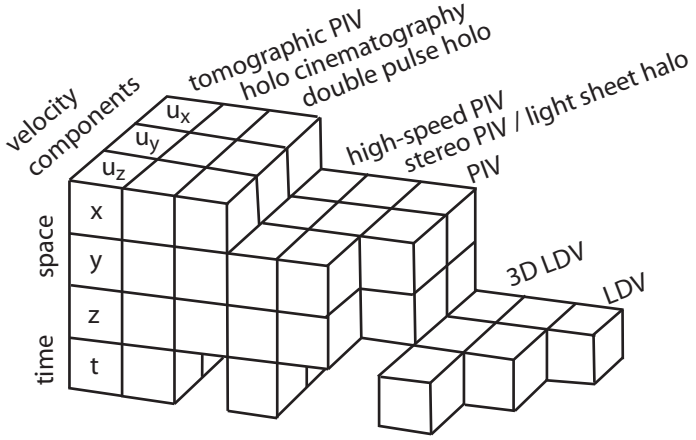

Figure 2.7: Overview of conventional optical velocity measurement techniques and their respective spatial and temporal resolutions [25].

the velocity throughout a complete three-dimensional space, only the use of holo-cinematography or tomographic PIV [33] is available. The experimental complexity although is many magnitudes higher than PIV and, albeit the benefits of the volumetric velocity information are undisputed, considerations towards the time consuming computational evaluation process have to be done.

Finally, the number density (also concentration if signal is quantifiable) of certain species is also useful to determine the local distribution in space and location of e.g. the flame front. Commonly, LIF is used to identify burned and unburned regions of the flame by recording e.g. the OH-radical as an intermediate product of the combustion [82].

2.3.2 Particle Image Velocimetry

The method of particle image velocimetry records the displacement of particles (in this thesis also called "droplets" synonymously) over time within a plane and subsequently calculates discrete velocity vector fields. A setup example of the recording process is shown in figure 2.8. The flow is doped with seeding / tracer particles and their subsequent movement is illuminated by e.g. a laser light sheet. The illuminated particles are recorded onto a screen (preferably a photograph, movie camera, or digital sensor) at least twice within a short time interval to capture their transient displacement. Both recordings are subdivided into areas called "interrogation windows" from which the local displacement vector is calculated with statistical tools (auto- or cross-correlation) assuming a homogeneous movement of the particles within the interrogation window. Dividing the vector components by the separation time between the two recordings gives the velocity of the particle movement and thus the velocity components of the transient flow motion.

Within flow research, PIV is a standard technique and its applicability is greatly diverse. The following overview of the functionality of PIV therefore only considers the relevant parts for the featured experiments and is based on the literature by Raffel [84], Westerweel [85, 86], Keane [87], and Duncan [88].

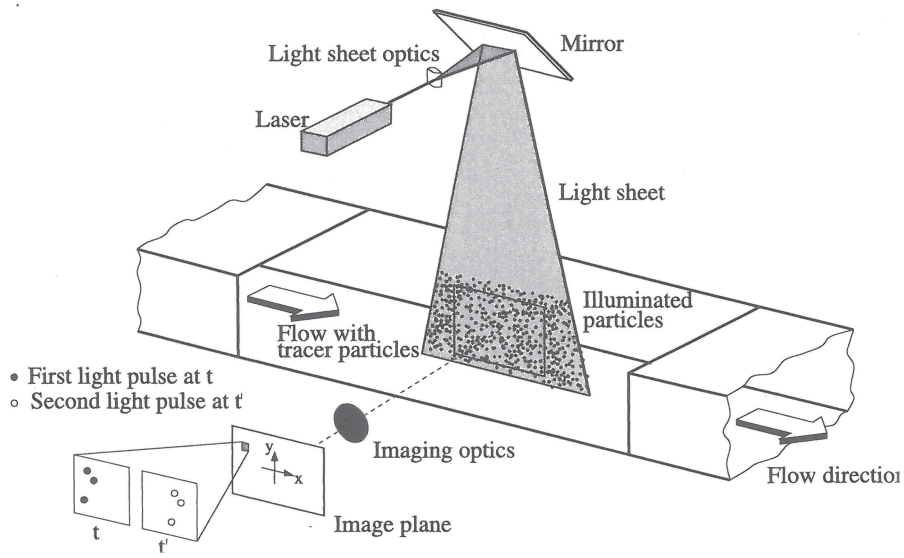

Figure 2.8: Conventional PIV setup [84].

2.3.2.1 Illumination, Imaging, and Vector calculation

As mentioned earlier, a conventional PIV setup is shown in figure 2.8. In the following, the individual parts of the setup like tracer particles, illumination and detection of the scattered light as well as the subsequent calculation of the velocity vectors are discussed.

At first, the flow is doped with particles which comply to minimizing the slip between particle velocity and flow velocity as expressed in equation 2.18:

$$s = \left| \frac{u_f - u_p}{u_f} \right|. \tag{2.18}$$

In turn, there is a conflict between the particle size and its ability for sufficient light scattering (Mie-scattering) because the light scattering intensity is quadratically dependent on the particle diameter. However, the particle velocity usually follows the actual flow field velocity by an exponential law shown in equation 2.19:

$$u_p(t) = u_f \left[1 - \exp\left(-\frac{t}{\tau_s} \right) \right]. \tag{2.19}$$

The characteristic time τ_s is shown in equation 2.20 with the dependent quantities d_p resembling the droplet diameter, ρ_p the density of the droplets, and μ the dynamic viscosity:

$$\tau_s = d_p^2 \frac{\rho_p}{18\,\mu}. \tag{2.20}$$

As described by Böhm [89], the maximum resolvable frequency (inverse of the turbulent time

scale) with tracer particles is described by (with s as the slip velocity):

$$f_c = \frac{\sqrt{2s - s}}{\tau_s \sqrt{(1-s)^2 \left(1 + \frac{\rho_f}{2\,\rho_p}\right)^2 - \left(\frac{3\,\rho_f}{2\,\rho_p}\right)^2}}. \tag{2.21}$$

When using large density ratios e.g. particle seeding and air ($\rho_p \gg \rho_f$), the highest resolvable frequency (equation 2.21) can be reduced to

$$f_c = \frac{0.0227}{\tau_s}. \tag{2.22}$$

The size of the particles is therefore crucial for an adequate following of the flow structures. Additionally, the particles have to be chemically inert and resist high temperatures. Only solid particles (titanium oxide, graphite, boron nitride, etc.) achieve the temperature resistance and are available within flames without evaporating (above 1500 K). Solid particles tend to introduce abrasive forces between mechanically moving parts of the setup (e.g. in an engine between the reciprocating cylinder and liner as well as between the valves and the cylinder head). Liquid tracer particles e.g. silicone oils or hydraulic oils (density between 800 - 900 kg / m^3) solve this problem, but are prone to evaporate above 1000 K. This makes measurements in temperature sensitive environments (e.g. compression stroke of an engine) difficult and reduces the recordable time frame. Still, their self-greasing characteristic and spatially homogeneous distribution are beneficial for in-cylinder measurements. Conventionally, the liquid particles are produced with a Laskin nozzle aerosol generator and their particle diameter is relatively similar to solid particles at $\sim$1 μm. An overview of different particles and their characteristic PIV-usability is shown by Melling [90] and Reeder [91].

The second part of figure 2.8 involves the illumination of the particles. Commonly, a laser light source is used because of the short pulse lengths which enables a freezing of the transient motion. Additionally, the laser light can be formed into a light sheet with conventional optics to produce a distinctive plane in which the movement of the particles is tracked. Further, with the light intensity available, the elastic scattering (Mie-scattering) of the particles can be easily recorded. In recent years, all-solid diode-pumped Nd:YAG lasers are also able to produce repeatable laser pulses at high repetition rates. This way, vector fields separated only by about 100 μs (corresponding to a recording repetition rate of 10 kHz) are recordable and the transient motion of the flow is fully visible. To simplify the recording with a digital camera (due to their quantum efficiency), the Nd:YAG lasers operate often with a wavelength of 532 nm which is the second harmonic of the fundamental 1064 nm wavelength.

In a mechanical sense, the last step of the setup in figure 2.8 is the detection / recording of the particles. The transient particle displacement is commonly recorded with either CCD- or CMOS-sensors (indicated as the "image plane"). Both are digital sensors with which the recording and subsequent calculation of the vector fields on computer hardware is straightforward. Both convert the light transmitted by photons into electrical currents which are presented as the number of counts in each pixel in the raw image. The main differences between CCD- and CMOS-sensors are their spatial and temporal resolution abilities (due to their individual mechanical setup / electrical operation). The CCD has a higher spatial resolution, but is only able to operate at low frequencies (typically between 5 - 30 Hz) due to a single A / D converter. Contrarily, each pixel of a typical CMOS-sensor has its own A / D converter and therefore the readout time is reduced. Imaging

frequencies of multiple kHz are feasible. Because of the reduced available space (due to the A / D converters) and light gathering optics, the fill factor is retarded thus increasing the exposure time (when compared to a CCD-sensor). Still, the availability of the temporal resolution with which previously unknown flow motion is recordable justifies the compromises.

The combination between the illumination (laser light pulse) and detection system (exposure time of frame) at high repetition rates requires an exact timing sequence. Two common approaches record raw images either with a double exposure on one image frame (double exposure / single frame method) or the image is divided into two frames each exposed separately (single exposure / double frame method). The latter is used in this thesis and therefore presented in more detail.

Each frame consists of recorded Mie-scattering produced by the particles. In order for the minimum time separation between both frames (and hence the maximum resolvable velocity), the first light pulse is triggered at the end of the exposure time of the first frame (an example timing diagram is shown in figure 2.9). The light pulse for the second frame is triggered according to the time separation Δt required by the flow speed. This method enables time separations just above the read-out time of the camera (due to timing discrepancies to $\sim 5\,\mu$s).

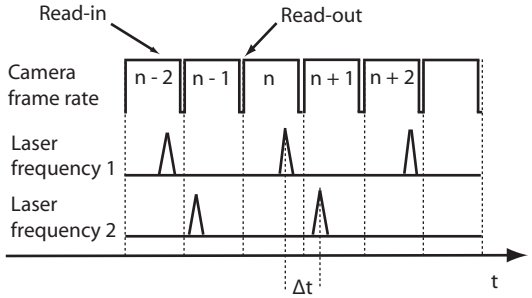

Figure 2.9: Example timing diagram for PIV in double-frame / single-exposure recording mode [84].

The time separation between frames and thus the velocity range of the resulting vector fields is based on the distance of the particle displacement. A typical displacement of $^1/_4$ of the interrogation window size (using e.g. 32 x 32 px) [84] is required for sufficient statistical correlations. The faster the flow field, the shorter the time separation.

The vector calculation is mostly done with automated computer algorithms due to the large amount of recorded data (e.g. a typical CMOS-camera has an onboard memory of 8 GB, equaling to 5400 double-frame images). To increase the performance of the algorithm (minimize number of erroneous vectors), there are different approaches to enhance the quality of the raw image. By subtracting a phase-averaged background image without particles, the background noise of the CMOS-sensor is reduced. Additionally, using a sliding average filter enhances the contrast of single pixels in a predefined neighborhood by subtracting the average within the vicinity of them [92].

The process of the algorithm using images recorded in single exposure / double frame mode is shown in figure 2.10. The cross-correlation method is used to calculate the vectors from the colored interrogation windows with the intensity fields $I(i,j)$ and $I^{'}(i+x,j+y)$ [87].

Each single frame is subdivided into interrogation windows. The intensity fields $I(i,j)$ and $I^{'}(i+x,j+y)$ are transformed into the frequency domain via fast Fourier transformation and the correlation plane $R_{II}(x,y)$ is calculated. Finally, the movement of the particles is expressed

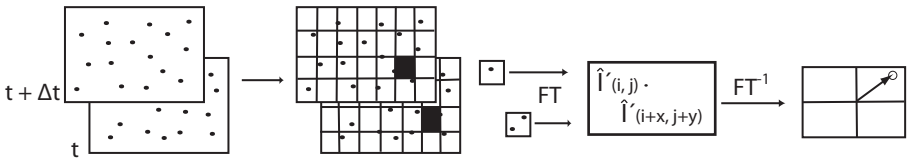

Figure 2.10: Schematic of the vector calculation process using single-exposed / double frame images and a cross-correlation algorithm [92].

by a vector from the center of the interrogation window to the correlation peak in the correlation plane (not shown in figure 2.10).

Looking at the calculation of the correlation plane in more detail, equation 2.23 expresses the cross-correlation of the intensity fields $I(i,j)$ and $I^{'}(i+x,j+y)$.

$$R_{II}(x,y) = \sum_{i=-K}^{K} \sum_{j=-L}^{L} I(i,j)\, I^{'}(i+x,j+y). \tag{2.23}$$

The area of $I(i,j)$ is smaller than $I^{'}(i+x,j+y)$ (e.g. $I^{'}(i+x,j+y)$ is twice the size of $I(i,j)$). By linearly shifting $I(i,j)$ around in $I^{'}(i+x,j+y)$ (without crossing over the edges) the values of the correlation plane (same size as $I(i,j)$) are calculated. The better the intensity fields match, the higher the correlation value. The speed of this calculation can be increased by transforming the intensity fields into the frequency domain and multiplying their complex conjugate indicated by $\hat{I}(i,j)$ and $\hat{I}^{'}(i+x,j+y)$ in figure 2.10. The correlation plane results by transforming the FFT field back into the spatial domain. Finally, a direct estimate of the particle displacement is available by locating the highest correlation peak.

The resulting vector resembles only the average shift of the particles within the interrogation area, as the cross-correlation does not use the actual particle velocity. It is therefore only a first order method and sufficiently small interrogation windows are required to minimize second order effects. Still, in each interrogation window, the number of particles ($\sim$5 - 10 as stated in [84]) has to be sufficient to determine the trajectory and absolute velocity value.

Common techniques to increase the robustness and efficiency (of extracting the velocity information) of the algorithm are window overlapping and multi-pass with decreasing window size. The window overlapping method with a value of e.g. 50% refines the grid produced by the initial interrogation window size and calculates a velocity value between every interrogation window (see Westerweel [85]). The method of multi-pass with decreasing window size uses an initial interrogation window size (e.g. 128 x 128 px) in the first pass and calculates a reference vector. In the next pass, the window size is half of the previous window size (64 x 64 px) and the reference vector is used as a best-choice window shift [92]. This is continued until the final interrogation window size is reached.

In a final step, a post-processing of the vector fields is necessary to reduce spurious vectors. These are vectors which show anomalies in comparison to their adjacent vectors such as differences in magnitude or counter-directed trajectory. These vectors are either excluded from the vector field or altered. The missing vectors can be inserted e.g. with a standard least-squares interpolation scheme using the neighboring vectors.

2.3.2.2 Advancement from 2C- to 3C-PIV

The description of the PIV methodology above is restricted to displaying only the in-plane velocities u_x and u_y of the measuring plane (light sheet). Typically, the flow structures in technical environments are three-dimensional and therefore the necessity to capture the out-of-plane velocity u_z is essential for a more comprehensive understanding.

Multiple experimental setups are possible to retrieve the out-of-plane velocity u_z. The simplest setup would be using a single camera with an arrangement of mirrors, but the error sources are numerous. A different approach is using two cameras arranged opposite each other along the same line of sight to record the flow motion in two offset parallel layers at three time instances and estimating the out-of-plane velocity [84]. The most advanced and widespread method is using two cameras in a stereoscopic configuration (hence stereoscopic PIV), meaning two different viewing angles and reconstructing the out-of-plane velocity from the individual projections. The camera configurations can either be with a lens translation method in which the object plane, lens plane, and image plane are parallel or with an angular lens displacement configuration in which the object, lens, and image plane intersect in a common line adhering to the Scheimpflug criterion [93] shown in figure 2.11. The specialty of the latter setup is the Scheimpflug criterion as this enables a focused view of all the particles within the object plane. The object plane, lens plane, and image plane are collinear. The angular setup was used in the experiments and therefore is explained in more detail.

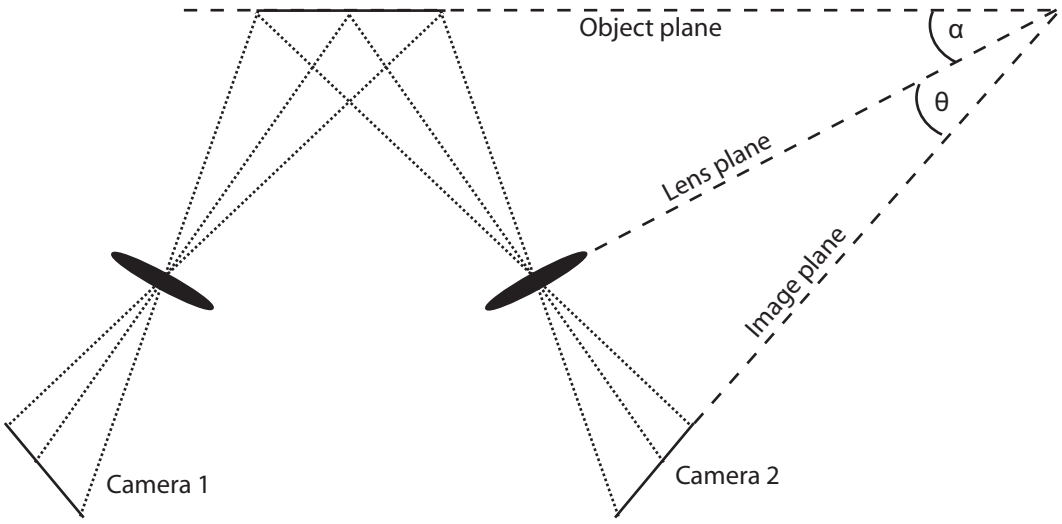

Figure 2.11: Stereoscopic-PIV setup with angular lens displacement and arranged according to the Scheimpflug criterion.

The best imaging of the particles is along the principal axis of the lens which is achieved with the angular setup. Additionally, tilting the back planes according to the Scheimpflug criterion enables the use of small f-numbers required to record the light scattering but which also reduces the depth of field [84]. Fundamentally, the perspective distortion of the setup produces a variable magnification factor over the field of view. The calibration and reconstruction of the two projected, planar displacement fields is therefore essential.

In order to calculate the out-of-plane velocity both images of the cameras have to be matched. Using a dual-plane, three-dimensional target placed coincidentally to the light sheet, the calibration of the images is reduced to matching the embedded marks of the target from each camera

perspective. The detectable marks have to be uniform and a constant displacement is advisable. The number of marks increases the accuracy of the calibration. Additionally, the camera viewing angles have to be calculated for the reconstruction of the three-component velocity vector. With the two-dimensional displacements of the particles on two separate image planes, a relation to the three-dimensional displacements in the object space is possible. The coordinates in the object space are connected to the planar image coordinates by either the pinhole or the polynomial fit model [84]. The polynomial fit model uses a second or third order polynomial to calculate the volume reconstruction. A drawback of this model are the strong distortions near edges. The pinhole model in turn assumes all light from the object plane passes through a single point in space onto the sensor. A non-linear fit is then used to map the object space calibrated feature points to a given functional [84]. With the fitted camera parameters, the local viewing angle for each point on the sensor can be calculated.

The calibration method above assumes the target is placed coincidentally to the laser light sheet. This is not always possible and a slight misalignment can lead to strong perturbations in the velocity components. To correct this, a disparity map is calculated from two simultaneously recorded particle images. The resulting two-dimensional vector field displays the mismatch of the particle coordinates.

The velocities u_x, u_y, and u_z are reconstructed from the two-dimensional velocities calculated for each camera viewing angle and are presented in equations 2.24 - 2.26.

$$u_x = \frac{U_{x2}\ \tan\alpha\ - U_{x1}\ \tan\phi}{\tan\phi - \tan\alpha}. \tag{2.24}$$

$$u_y = \frac{U_{y1} + U_{y2}}{2} + \frac{U_{x1} - U_{x2}}{2}\ \left(\frac{\tan\beta_1 - \tan\beta_2}{\tan\alpha + \tan\phi}\right) = \frac{U_{y1} + U_{y2}}{2}. \tag{2.25}$$

$$u_z = \frac{U_{x1} - U_{x2}}{\tan\alpha + \tan\phi}. \tag{2.26}$$

Equations 2.24 - 2.26 are specifically for the setup shown in figure 2.12. In all equations, the viewing angles of the separate cameras are taken into account and therefore the calibration is of special importance.

A vast amount of literature about stereoscopic PIV setups and their applicability is available. Noteable are e.g. [27, 94, 95, 96, 97, 98, 99, 100, 28, 101, 102, 84]

2.3.2.3 Uncertainties of PIV measurements

PIV measurements are prone to a number of uncertainties due to their complexity and indirect recording of the flow field. First, some of the experimental errors are addressed and subsequently, some errors of the post-processing.

As stated above, the particle characteristics (e.g. size, density, phase of matter) and the seeding technique are very important. They directly influence the quality of the measurements in form of e.g. slip velocity, number density per unit volume, and detectability by the vector calculation algorithm. A homogeneous distribution of the particles throughout the object plane is necessary to reduce the possibility of a systematic bias. Further, the particle size on the image plane needs to

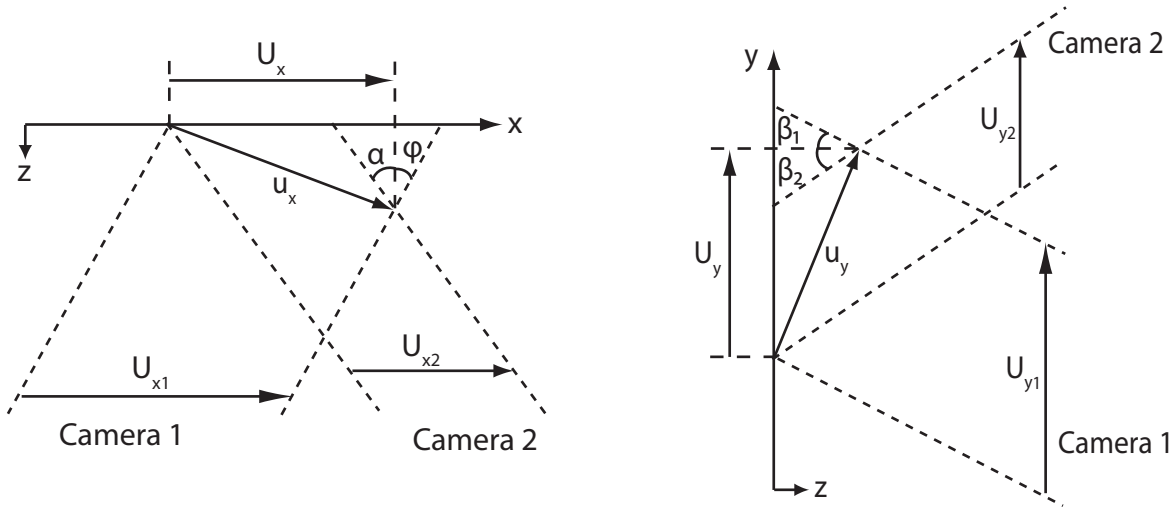

Figure 2.12: Schematic of velocity calculation with a stereoscopic PIV setup. Horizontal camera setup (left) and vertical displaced camera setup (right).

be spread over multiple pixels to reduce the effect of peak locking. An error which also addresses the particle displacement is the time separation between the single exposure / double frames. This correlates with the integral time scale of the flow field. For the algorithm to perform well, a particle displacement of $\sim 1/4$ of the interrogation window size per double frame is a common perception as stated in [84]. Larger and smaller displacements (hence the time separation) can influence the calculation of the correlation plane and produce spurious vectors.

As mentioned earlier, the calibration of the image coordinates (virtual) to the physical coordinates (pixel to meter) is necessary to obtain the best possible flow field data as the viewing angles are directly linked to the velocity components. The displacement (translational / rotational) between the laser light sheet and the target should be minimal and a disparity check can resolve the misalignment.

In this thesis, the PIV measurements were done through a quartz glass cylinder (thickness $\sim$30 mm) which may cause aberrations due to its spherical surface. These result in distortion of the image plane and poor focusing within the boundary layer near the wall. Still, when imaging the flow within the cylinder far from the edges these influences can be corrected and are acceptable [103].

Further error sources such as e.g. background noise, correlation peak detection and general considerations for PIV are presented by [104, 105, 106, 107, 99].

2.3.3 Laser-induced Fluorescence

Laser-induced fluorescence is spontaneous emission from atoms or molecules that have been excited by laser radiation [82]. If an atom or molecule is resonately stimulated by a photon with the energy of $h\,\nu$ through laser light, the atom or molecule absorbs the energy and is lifted to an excited state. The subsequent spontaneous emission of a photon with the discrete energy of $h\,\nu$ is based on the instability of the excited state. The fluorescence signal strength is directly linked to the number density of the excited species in the focal volume. In a practical application like a combustion system, the concentration and temperature are derivable from these recordings and are

useful in characterizing the flame. In such an environment, the technique is especially beneficial because of its non-intrusiveness and high spatial / temporal resolution.

This review is based on the literature of Daily [82], Kohse-Höinghaus [108], and Eckbreth [109] and focuses on the detection of the diatomic OH-radical in flames.

2.3.3.1 Excitation and Detection

The atomic and molecular structure and dynamics of radiative transitions (absorption / emission) is based on the motion of nuclei and electrons described by the Schrödinger wave equation:

$$-\frac{\hbar^2}{2m}\nabla^2\Psi_{(r,t)} + V_{(r,t)}\Psi_{(r,t)} = i\hbar\frac{\partial\Psi_{(r,t)}}{\partial t}. \tag{2.27}$$

The equation consists of the wave function Ψ, Planck's constant h (divided by 2π), the mass of the atom / molecule m, and the potential field $V(r,t)$. In systems which are not time-dependent, equation 2.27 can be reduced to:

$$H\psi = E\psi, \tag{2.28}$$

in which H represents the Hamiltonian operator and E the energy. Equation 2.28 can only be solved by the eigenfunctions of ψ. Thus, only discrete states called "quantum" states are allowed to solve the equation. The quantum states are dependent on the total energy, the total angular momentum of the system, and the angular momentum of each particle allowing only discrete packets of energy to be absorbed.

In a basic perception, the energy of an atom is determined by the electron and its respective behavior within the orbit around the nucleus. The discrete energy levels of the electron can be described by the principal quantum number, the orbital angular momentum quantum number, the magnetic quantum number, and the electronic spin quantum number. Likewise, for diatomic molecules, their energy is determined by three parts: the orbiting and spin of the electrons, and the vibration and rotation of the nuclei with respect to each other [82]. These three parts comprise the total energy E_{sum} of the diatomic molecule as shown in equation 2.29 with E_e as the electronic, E_v the vibrational, and E_r the rotational energy parts.

$$E_{sum} = E_e + E_v + E_r. \tag{2.29}$$

Equation 2.29 can also be expressed graphically, as shown in figure 2.13. It shows a diatomic molecule AB (equilibrium energy state E) as it is electronically excited to the energy state of AB* (energy level E*). The horizontal lines represent the vibrational and rotational energy levels. The difference in energy level of the electronically excited energy states are larger than the vibrational which are also larger than the rotational. The vertical displacement of the corresponding lines indicate these energy differences. The vibrational and rotational energy levels are important as during the residence time in an excited state energy is transfered towards these levels. The resulting spontaneous emission is therefore shifted to lower frequencies, i.e. a red-shift of the fluorescence signal occurs (the excitation wavelength is lower than the detection wavelength). This phenomenon is also known as the Stokes' shift.

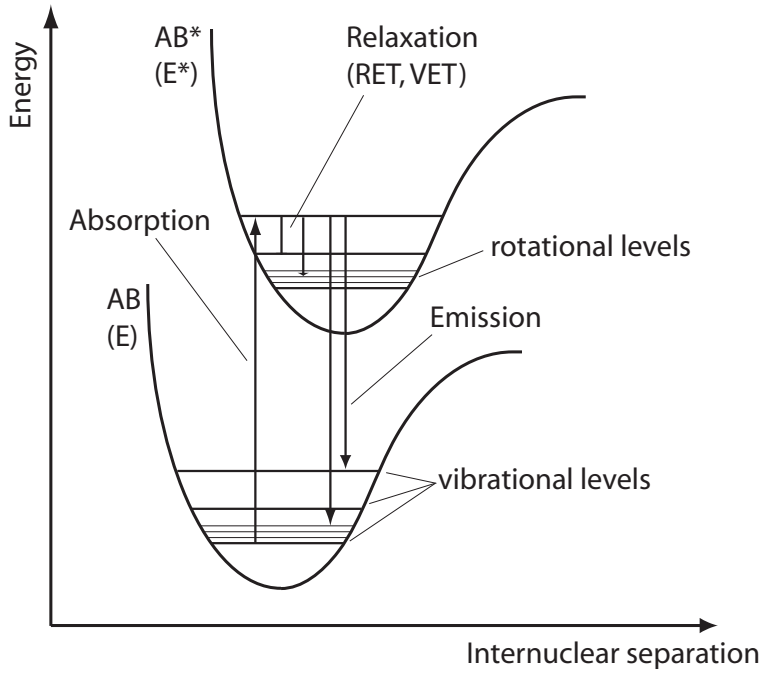

Figure 2.13: Potential energy curves for ground, excited, and pre-dissociative states of a diatomic molecule (known as Morse potential curves)

The excitation of AB is only possible, as explained earlier, if equation 2.30 is balanced with $h\,\nu$ being a discrete energy portion.

$$E^* - E = h\,\nu = h\frac{c}{\lambda}. \tag{2.30}$$

The requirements of the above mentioned equation are not stringently bound to the monochromatic wavelength λ (c being the speed of light). As stated in [110], the broadened spectrum is due to Doppler-broadening as the main reason due to temperature and pressure influences (other sources are negligible in gaseous media).

The detection of the fluorescence signal in a practical environment can be separated in an absorption (number of molecules excited) and a fluorescence quantum yield (ratio between spontaneous emission rate and total rate of relaxation processes) part and is described as

$$I_{LIF} = c\,\underbrace{I_{Laser}\,N(p,T)\,f_{\lambda,J}(T)\,B_{ik}\,\Gamma(p,T)}_{Absorption}\,\underbrace{\frac{A_{ki}}{\sum_j A_{kj} + Q_k(p,T) + P_k}}_{Fluorescence\ quantum\ yield}, \tag{2.31}$$

in which I_{LIF} is the fluorescence signal intensity and c an experimental parameter [111]. The probe volume determines the number density of respective species $N(p,T)$ which are excitable multiplied by the temperature dependent Boltzmann fraction $f_{\lambda,J}(T)$ given the population of the initial level i. B_{ik} is the Einstein coefficient which describes the absorption probability for the transition from i to k (excitation level). Further, the laser intensity I_{Laser} determines the fluorescence intensity as well as the spectral overlap $\Gamma(p,T)$ of the laser profile with the absorption line. The rate of the spontaneous emission is determined by the Einstein A-coefficient (A_{ki}) in relevance to

the sum of the rate of depopulation from the excited state ($\sum_j A_{kj}$), quenching effects ($Q_k(p,T)$), and pre-dissociation (P_k). The latter mentioned quenching and pre-dissociation effects are special cases in which a de-excitation occurs without emission of fluorescence. Quenching can result from e.g. collisions of the excited molecule with other species (oxygen is well known for its quenching effects) [34].

The equation is only valid for weak excitation, in which the fluorescence signal is approximately linear to the laser intensity given the proportional balancing of the ground and excited state of the molecules. If the laser intensity is increased, the signal is saturated and the fluorescence signal is independent of the laser intensity. Other surrounding boundaries like pressure influences, temperature and species compositions as well as the mass of the species also have an effect on the measurement [82].

2.3.3.2 Uncertainties of PLIF measurements

The imaging of concentrations, number density distributions, or temperature profiles with planar laser-induced fluorescence (PLIF) is not without uncertainties. In a stepwise analysis, the error sources at the excitation of the molecule, the collection of the scattered fluorescence, and the subsequent photon to pixel intensity conversion (including intensifier / CMOS-sensor issues) are listed. Only the most severe error sources are addressed when imaging the transient motion of the intermediate OH-radical in flames, as done in this work.

First, the shot-to-shot laser power fluctuation can introduce a systematic linear error to the LIF signal. Therefore, a reference fluorescence signal can be recorded along the laser light path of the measuring plane to calibrate the recorded data. Further, absorption of the signal by other species along the light path to the sensor can be problematic. Other possible interferences along this line include light scattering and interactions with particles.

The collection optics are used to image a portion of the laser light sheet onto the camera sensor. They define the image scale and the amount of light collected. Normally, only a section of the spectral bandwidth is required. The transmission rate of the filters used reduces the LIF signal as will the diameter of the aperture (f-number if focal length is constant). In general, high transmission rates and low f-numbers result in higher LIF signal strengths, hence yield a better signal-to-noise ratio (SNR).

The conversion of photons emitted by fluorescence to actual pixel intensities is usually done with an intensifier coupled to a camera sensor (commonly only used with the gating function and when the fluorescence light is in the spectral range of the ultra-violet segment). The intensifier itself consists of a photocathode surface, a micro channel plate (MCP), and a phosphor screen. First, the photons produce photoelectrons which are then accelerated through the MCP by a voltage between the MCP and photocathode. Through the MCP, the number of photoelectrons is multiplied and these produce a significantly higher number of photons which are detected by the camera sensor. The voltage between the MCP and the photocathode can produce a transient overshoot of photons in the first images. Therefore, several images at the beginning of a recording are biased. Other effects using an intensifier are depletion which is thoroughly examined by Weber [40].

The uncertainties mentioned above are only qualitative as to possible systematic errors and parameters to consider. A more quantitative approach is possible by calculating the signal-to-noise

ratio as described by Clemens [112]. In equation 2.32, the signal ($\eta\, S_{pp}\, G$) and the intrinsic background noise (amplifier noise, digital feedthrough noise, thermal noise, dark-current noise, and quantization noise) N_{cam} are coupled:

$$SNR = \frac{\eta\, S_{pp}\, G}{\sqrt{\eta\, \kappa\, S_{pp}\, G^2 \,+\, N_{cam}^2}}. \tag{2.32}$$

The parameter η relates to the efficiency of the optical system, κ to the noise factor due to the amplification inside the MCP, and G to the gain. The number of photons collected per pixel S_{pp} is dependent of the local laser fluence, Planck's constant h, the laser frequency, the image volume of each pixel, the differential scattering cross section, the number density of the scattering medium, the transmission efficiency, and the solid angle subtended by the lens [112]. If gain G is increased, the shot noise (fluctuations of the number of photoelectrons which are detectable at each pixel) is increased, but also the signal level. An increase in gain is limited to the shot noise limit causing no further increase in SNR. According to Clemens [112], SNR levels of above 20 suffice for quantitative imaging, for qualitative imaging, lower values are also possible.

3 Experimental setups

This section describes the experimental setup of the optically accessible internal combustion engine. Additionally, each laser diagnostical setup is detailed separately and consists of the specific laser diagnostical setup, an assessment of the possible error sources, and the post-processing evaluation. The measurement sections are arranged according to their recording range starting with the intake stroke and ending with the combustion phase (see figure 2.1)

3.1 Optically accessible DISI IC engine

The spray-guided, direct-injection, spark-ignition (SG-DISI) internal combustion engine used in the experiments was a single-cylinder engine with an 82 mm bore and 86 mm stroke. The compression ratio was 9.88 and the displacement 450 cm^3. It was equipped with twin-cam, dual-manifold inlet valves, a pent roof aluminum cylinder head, and a steel liner. In figure 3.1, a schematic of the engine together with an arbitrary imaging setup is shown. A placeholder for different injectors was oriented centrally within the cylinder head. The spark plug was mounted at an angle of $\sim 30^\circ$ relative to the injector between the outlet valves (not shown in figure 3.1). The optical accessibility was achieved by mounting a 30 mm high quartz glass ring between the cylinder head and the liner. The liner was vertically movable on a linear translation shaft. This allowed quick access to the quartz glass for cleaning purposes. The glass ring itself was equipped with pent roof windows. A glass disc inserted into the flat piston crown allowed optical access through the elongated bowditch piston. The cylinder head and liner were preheated to 60° C mimicking steady-state engine conditions (more typical in series engines is 80 - 100°C).

Different in-cylinder flow patterns were achieved by guiding the intake flow $\sim$0.2 m before the intake valves. Here, different circular steel plates were able to deform the flow. A tumble flow pattern (see figure 2.2, right) was created by blocking the lower half of the manifold inlet. Since the cylinder head was equipped with overhead valves, the axis of the tumble charge motion was aligned theoretically parallel to the crankshaft orientation. Closing one of the dual-manifolds produced a swirl flow motion (see figure 2.2, left) within the cylinder. The swirl motion was directed perpendicularly to the crankshaft, rotating around the cylinder axis. To create the neutral flow motion no plates were inserted into the manifold, thus the intake flow was guided unhindered into the cylinder.

The setup shown in figure 3.1 is referred to as the 'tumble plane configuration' as the camera viewing angle is parallel to the large scale tumble motion caused by the dual-manifold inlet (camera viewing axis is also aligned parallel to the crankshaft direction). The belt transmission to the overhead camshafts is behind the cylinder so that a maximum visible angle into the combustion chamber is possible. Camera and laser can be switched to form the so-called 'swirl plane configu-

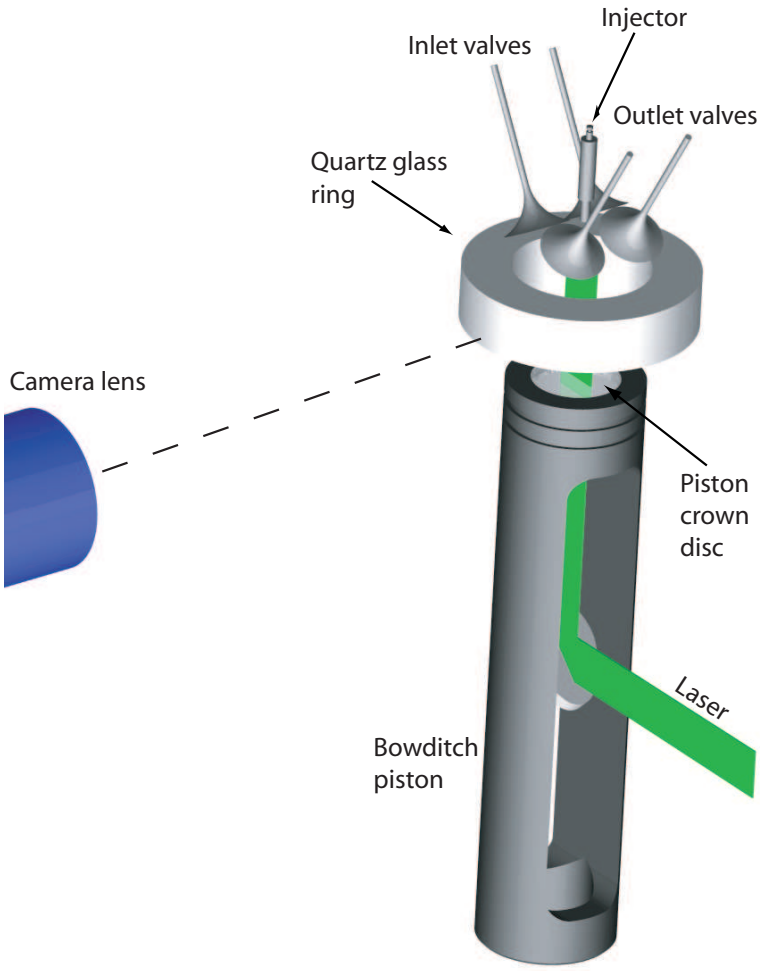

Figure 3.1: Engine schematic without liner and cylinder head. An example camera setup is shown with a tumble plane view (camera sensor parallel to tumble vortex axis). Cylinder position is at mid-stroke.

ration'. The axis of the large scale flow field produced by a swirl charge motion would then be in the line of sight of the camera's viewing axis.

All other standardized state of the art measuring facilities (engine speed, pressure, temperature, etc.) required to operate the research engine where also installed. In particular, pressure sensoring of the in-cylinder, the manifold inlet, and outlet was available separately. Temperature sensors monitoring the inlet, the cylinder temperatures as well as the outlet were also used.

3.2 Error sources during engine operation

In general, a categorization into three classes is proposed (increasing in influence) which point out error sources and considerations influencing the stability and reproducibility of the operating / measurement conditions. Each class can occur either during a single recording (i.e. the recording of multiple cycles at one parameter variation) or throughout a complete measurement setup

(i.e. the setup imposes the error source, hence it is a systematical error). Where the influence of the error source is not quantifiable, its impact is estimated. The classes comprehend:

1. **Class 0 error sources:** These errors / considerations are mostly systematic and during normal engine operation do not influence the measurement in any severity.
2. **Class 1 error sources:** Multiple engine cycles will be affected by these errors as they occur e.g. non-linear. These errors are time dependent as well as thermo-dynamically influenced. The pressure and temperature conditions within the cylinder for example are the main sources.
3. **Class 2 error sources:** This error class describes strong influences on the quality of the measurements. Most likely, the recordings have to be repeated or, if the error is not remediable, a different technological approach has to be realized.

The interplay between the laser diagnostical setups and the engine are versatile. Hence, to pinpoint different error sources the mechanical and optical components / setups are isolated. The following list gives an overview of the complexity and the sensitivity of the main error sources which have to be considered during engine operation, but makes no claim to be complete.

Class 0 error sources

- **Vibrations:** The vibrations of the engine should be well below or above the recording frequency for a negligible influence. Secondly, the broadband mirror inside the bowditch piston has to be isolated from the cylinder vibrations in order to record reproducible datasets. Further, the complete laser system as well as the detection system have to be isolated from the vibrations of the engine. For example, at 1000 rpm the first order oscillation frequency of the engine is $\sim$16 Hz. The high-speed laser diagnostics used in this thesis operated at 6 kHz, therefore the influence is negligible.
- **Engine speed:** The real engine speed is within 0.5% of the nominal engine speed. Small perturbations are due to the dynamics inside the cylinder e.g. cyclic variations.
- **Event timing:** The timing of valves opening and closing, as well as injection and ignition has to be phase locked over multiple cycles to produce datasets which can be used for statistical analysis. The crank angle shaft timing unit resolves up to 0.1° CA which delivers a maximum time shift depending on the engine speed (e.g. $16.\bar{6}\,\mu$s at 1000 rpm).
- **Temperature:** The temperature of the cylinder head and liner have to be stable throughout the recordings (to ensure reproducibility). The temperature gradient because of the quartz glass liner between cylinder head was not addressed. Measurements comparing the engine to a thermodynamic engine are detailed by Gleissner [67]. The error source is only mentioned for logical reasons, but is not within the scope of this work.

Class 1 error sources

- **Injection pressure:** The injection pressure has to be constant throughout the recordings. A static pressure chamber which provides a constant pressure is preferred. A reciprocating pump may introduce pressure fluctuations ($\pm\,5\%$).

- **Intake system:** The temperature and the mass flow of the intake air have to be carefully monitored. A temperature decline in the intake manifold appears e.g. during port-fuel injection because of the evaporation enthalpy. Further, the mass flow of the intake system is influenced when introducing seeding (e.g. during the PIV measurements). The quantities of seeding have a non-linear effect on the recordings because of their characteristic settling time.
- **Synchronization:** During the compression stroke, the recording frequency and the piston frequency are not phase locked. The piston velocity is retarded during the upward movement due to the increased pressure force. Hence, the piston movement is non-linear and a specific crank angle timing is difficult. The misalignment of fixed frequency and crank angle increase can be up to 15 μs throughout the compression stroke. This is within the time range of 0.1° CA at 1000 rpm and thus negligible.
- **Residual gas composition:** The opening and closing of the valves overlap during the engine cycle (see figure 2.1) and thus, a complete discharge of the exhaust gas emissions is not given. During motored operation, this effect is negligible. The effect is prominent during skip fired mode (one fired cycle, then multiple motored cycles) because the residual gas composition affects the subsequent cycle. The amount / composition of the residual gas can be measured with e.g. Raman spectroscopy, but is not within the scope of this work.

Class 2 error sources

- **Recording time:** Long run time measurements of the in-cylinder processes are limited due to the quartz glass ring. The seals between it and the cylinder head and liner tend to overheat and become porous. Hence, the compression of the in-cylinder volume is not possible anymore. Temperatures above 650 K are alarming.
- **Manifold inlet pressure:** The manifold inlet pressure (directly linked to the inlet mass flow) of the intake system strongly influences the in-cylinder processes. When comparing engine cycles with different settings (e.g. different charge motion), the in-cylinder pressure needs to be maintained as it effects the reproducibility (e.g. of the flow field). Deviations of a few millibar (within the accuracy of the measuring equipment) are acceptable.

3.3 Flow field measurements

The measurements of the in-cylinder transient flow field, spray development, and fuel distribution were all recorded with the camera / laser setup in the tumble plane configuration (see figure 3.1). The tumble plane was chosen because of its symmetrical orientation within the cylinder and because the tumble flow motion exhibits the most influential structures and effects during the combustion phase [67]. The main parameters of each recording setup are listed in table 3.1.

3.3.1 Experimental setup and data processing

The main engine setup is described in section 3.1. The three velocity components of the flow field were recorded with a stereoscopic PIV setup.

Table 3.1: Overview of the main parameters for the experiments of the flow field (3C-PIV), spray / flow field interaction (Spray), and fuel distribution (Fuel) measurements. Engine times are measured in ° CA and are relative to the top dead center of the compression stroke.

	Setting / Value		
	3C-PIV	Spray	Fuel
Engine			
Engine speed [rpm]	1000, 1500, 2000	1000, 1500, 2000	1000
Compression ratio	9.88		
Charge motion	tumble, swirl, neutral	tumble, swirl, neutral	swirl, neutral
Fuel/air ratio [-]	-	-	0.75 - 1.25
Rail pressure [MPa]	-	5, 10, 15	10
Manifold inlet pressure [mbar]	950, 1500	960	600
Injection duration [μs]	-	750	λ dependent
End of Injection [°]	-	50	300
Fuel	CEC RF-85 A 01		
Injector	multi-hole	multi-hole, swirl, annular orifice	multi-hole, annular orifice
Manifold inlet temperature [°C]	23	23	55
Camera			
Camera / Intensifier	Photron SA 1		Photron SA 1 with HS-IRO
Imaging plane	tumble		
Camera Start [° BTDC]	180	90	50
Camera End [° BTDC]	60	45	10
Temporal resolution []	one image per crank angle at 1000 rpm		
Spatial resolution [mm / px]	0.067	0.0625	0.067
Gate / Gain [ns / %]	-	-	3500 / 50
Field of view [mm^2]	25x40	43x44	43x44
Repetition rate [kHz]	12 - double frame mode		6
Delta t [μs]	7 - 40	-	-
Record cycles	100	100 - 200	100
Laser			
Repetition rate [kHz]	6		
Energy [mJ]	2.3	0.7	0.5
Wavelength [nm]	532	532	266
Light sheet dimensions [mm]	35 x 40 x 1	45 x 45 x 1	45 x 45 x 1

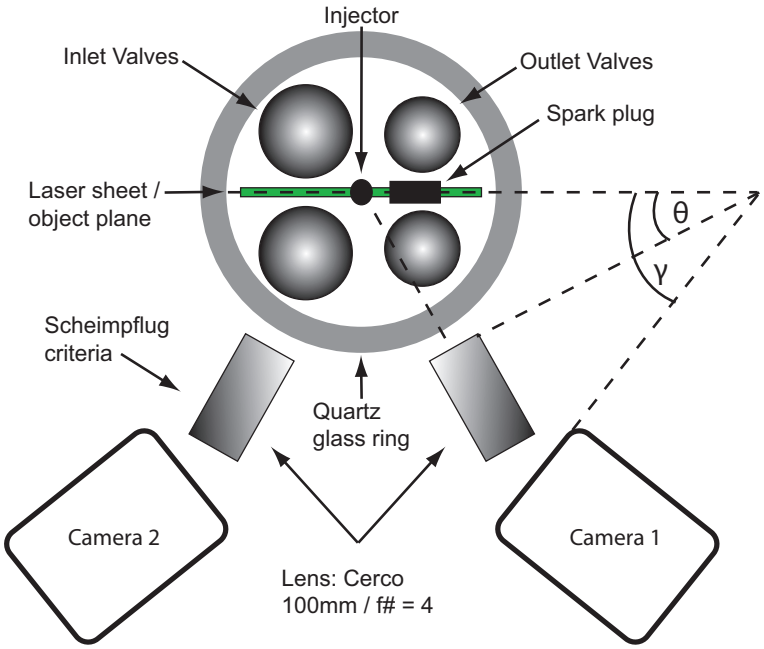

Figure 3.2: Schematic of the experimental stereo-PIV setup.

The recordings were taken at 6 kHz which resolves one crank angle per image at 1000 rpm (cameras operated in double-frame mode synchronized to the double-pulses emitted by the laser cavities). A frequency-doubled dual-cavity Nd:YAG diode-pumped slab laser (Edgewave IS6II-DE) was operated at 532 nm with a pulse energy of 2.3 mJ / pulse. Depending on the velocity of the flow field, the pulse-to-pulse time separation was between 10 and 40 μs. The light sheet was formed with a single -37.5 mm lens (cylindrical) and positioned centrally inside the cylinder (see figure 3.2). The dimensions of the light sheet were 35 x 40 x 1 mm^3 resulting in a reasonable compromise between in-depth spatial resolution and out-of-plane losses.

The seeding material, hydraulic oil (Liquimoly), was injected into the intake system $\sim$0.6 m upstream of the inlet valves resulting in a homogeneous distribution within the nitrogen inflow. The average diameter of the aerosol droplets was 1 μm. They were produced using a commercial droplet generator (Palas AGF 10D-S, see [67]) equipped with Laskin nozzles. During the recordings (compression stroke only) the droplets evaporated beyond 60° BTDC limiting the recording range to 180 - 60° BTDC. During each recording, the droplet deposits on the quartz glass ring did not degrade the imaging quality. However, following each recording, the quartz glass cylinder was cleaned to ensure reproducible conditions.

The Mie-scattered light was recorded with two CMOS cameras (Photron SA1) in the Scheimpflug arrangement shown in figure 3.2. The angles θ (between object plane and lens plane) and ϕ (between object plane and imaging plane) were $\sim$30°. The linear translation shaft hindered larger angles. Both cameras were identically equipped with 100 mm lenses (Cerco) and used a focal aperture of 4. During each recording all light except for the laser was turned off, hence no filters were applied to the lenses. The cameras were operated at 6 kHz in double frame mode. Each frame had an array size of 688 x 704 px with a pixel resolution of 0.067 px / mm. The field of view was limited due to the curved optical access and reflections caused by the spark plug to 20 x 40 mm^2 (see figure 3.3). The on-board memory of the cameras limited the recordings to 50 consecutive

cycles.

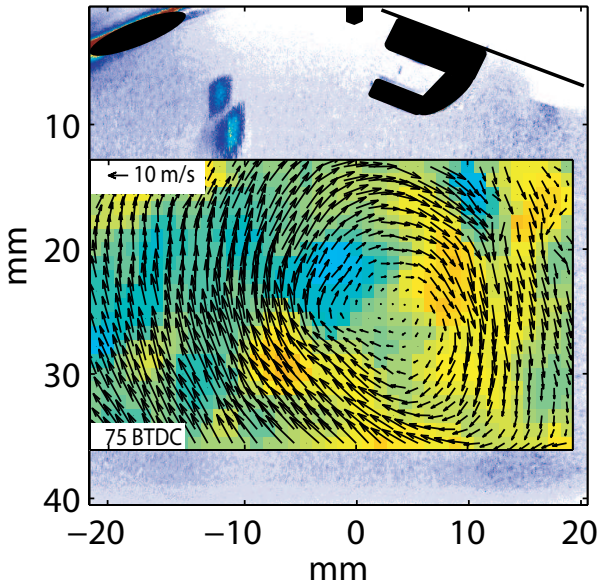

Figure 3.3: Field of view of in-cylinder flow field. The vector field is superpositioned onto a raw image indicating the component positions of the spark plug, injector, and inlet valve (from right to left).

Calibration

The apparent coordinates of the droplets recorded on the imaging plane are corrected to physical space coordinates using a three-dimensional, dual-plane calibration target (LaVision, target type 10). Because of the limited vertical displacement of the liner (translational shaft setup), the target could only be recorded in the required position without the quartz glass ring. The markers of the calibration target are used to dewarp the recordings because of the distortion caused by the different viewing angles and the quartz glass ring. Further, the viewing angles are obtained with a pinhole model in order to calculate the velocity vectors.

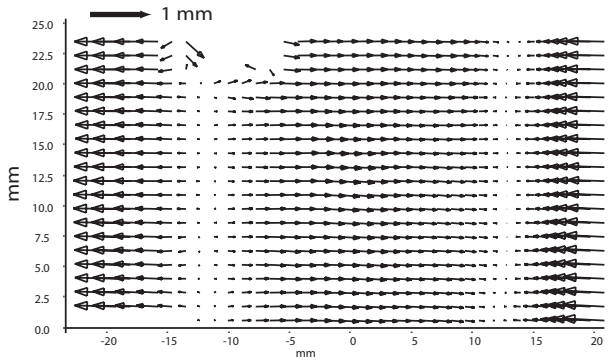

Figure 3.4: Disparity map after applying the self-calibration algorithm.

To reduce the mismatch of the recordings, a self-calibration algorithm with a pinhole model proposed by Wieneke [101] was used. It refines the camera parameters (i.e. viewing angles) by evalu-

ating the particle offset between simultaneously recorded PIV raw images, although limited to the first order coefficient. This results in a remaining mismatch of ∼5 px as shown in figure 3.4 by the disparity map which adheres to a maximum systematic error of 15% spatial offset. This error is acceptable, as the length scales of the recorded flows are larger than the interrogation volumes [10], albeit being more qualitative than quantitative.

To visualize this systematic offset, the phase-averaged velocity vector field at 160° BTDC (swirl charge motion, engine speed of 1000 rpm) was calculated with and without self-calibration. The difference between both velocity vector maps is shown in figure 3.5.

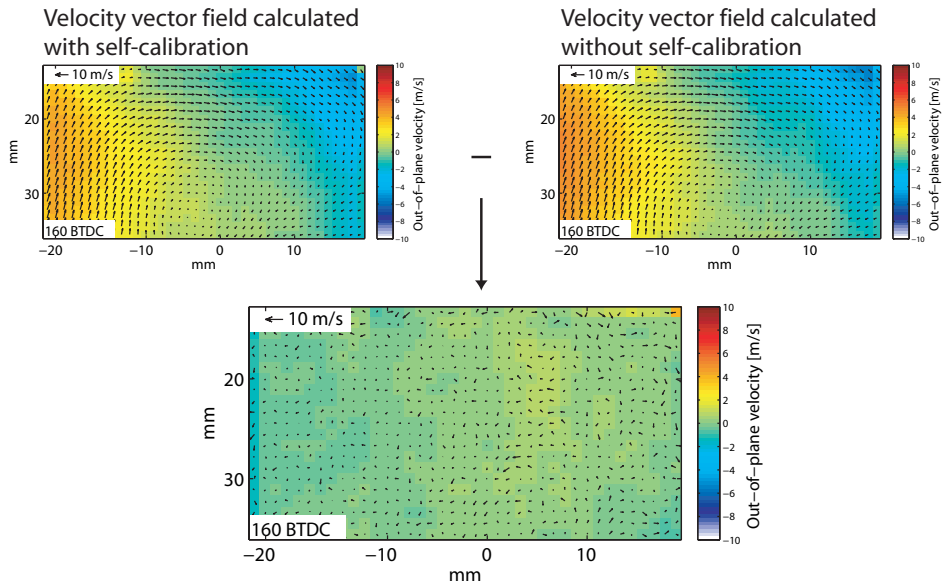

Figure 3.5: Comparison of an arbitrary phase-averaged velocity vector field with and without use of the self-calibration algorithm.

No pattern is visible and the out-of-plane velocity component is near zero (mean value of u_z in this example is ∼-0.16 $^m/_s$, 1-σ standard deviation is ∼0.44 $^m/_s$). In addition, the velocity distribution of each individual component at 160° BTDC with a tumble (left) and swirl (right) charge motion is presented in figure 3.6.

The in-plane velocities of the tumble charge motion show only little discrepancies. However, the out-of-plane component u_z shows a shift with the self-calibration to positive values. In comparison, the swirl charge motion shows a wider distribution of u_z (as expected) and also a shift to positive values. A systematic offset of the in-plane velocities is also visible. Notice the conclusions are only valid for the specific field of view.

Data processing

First, a small sliding average (5 px) was used to reduce the background noise of the images. Subsequently, the double-frame images of the instantaneous flow field recordings were evaluated using a commercially available cross-correlation PIV algorithm (Davis 7.2, LaVision). A decreasing multi-pass method with interrogation windows from 128 x 128 px with 50% overlap to 32 x 32 px

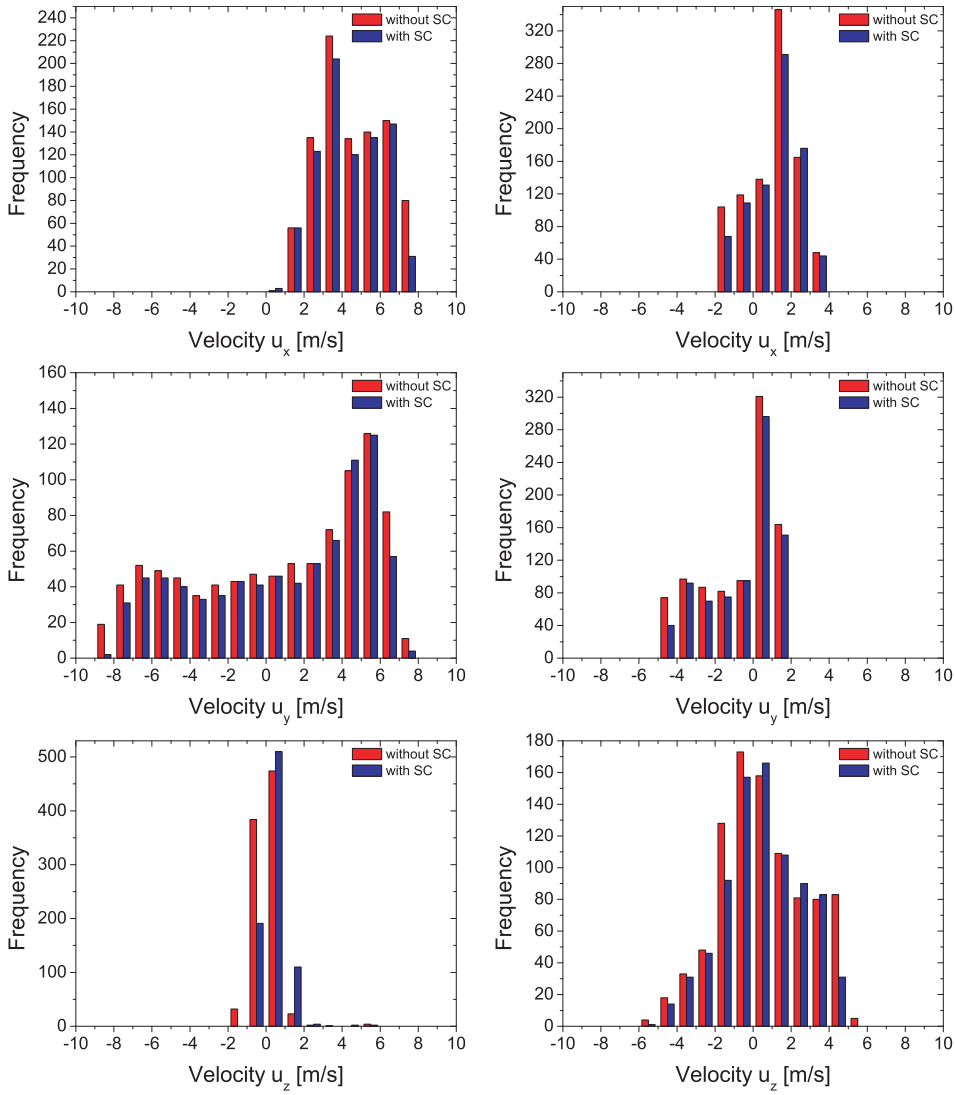

Figure 3.6: Distribution of individual velocity components u_x, u_y, u_z. Left: phase-averaged velocity field at 160° BTDC with tumble charge motion; right: phase-averaged velocity field at 160° BTDC with swirl charge motion. SC: self-calibration.

with 50% overlap (done twice) was used to generate the velocity vectors with a physical resolution of 2 x 2 mm and a vector spacing of 1 x 1 mm. The peak noise ratio Q (see Raffel [84]) was set to 1.8 to discard lower correlation values. Finally, a 3 x 3 median filter was applied to remove spurious vectors. The number of vectors was sufficient for all post-processing procedures with a maximum of ∼15% missing vectors at 60° BTDC.

3.3.2 Error sources of flow field measurements

Class 0 error sources

- **Laser:** The laser profile and energy have to be stable for each cavity throughout the recordings. Linear shot-to-shot effects would produce unequal Mie-scattering intensities of the

droplets and increase the number of spurious vectors.

- **Quartz glass cylinder:** The imaging of the droplets through a quartz glass cylinder with a thickness of $\sim$25 mm results in possible aberrations. As investigated by Reuss [103], aberrations do not affect the imaging plane when only a partial field of view of the cylinder is recorded. Contrarily, when imaging the whole cylinder, the optical effects at the edges increase and further consideration of error sources (e.g. distortion) is necessary.

Class 1 error sources

- **Pulse-to-pulse time separation:** The pulse-to-pulse time separation is set to resolve the velocities within a flow field in respect to their particle displacement. The compression stroke features large velocity gradients, thus a compromise is made using a constant time separation value (Δt). A trade-off between high velocities early in the compression stroke (requiring small time separations) and low velocities during the mid-section of the compression stroke (requiring long time separations) is required. In order to resolve the velocities within the compression stroke correctly, a varying time separation scheme has to be applied. This was not done because the error obtained during the compression stroke is assumed to be acceptable.
- **Calibration:** The CMOS cameras record the droplet displacement onto the image plane which has to be transformed into physical space coordinates. Further, the viewing angle of the cameras is important to calculate the out-of-plane velocity component. This is done with a calibration target (usually a dual-plane three-dimensional target). The alignment of the calibration target coincidentally with the laser light sheet is prone to errors. Therefore, using a self-calibration algorithm results in a disparity map which is required to ensure reasonable results.
- **Temporal mismatch:** Different time references are used during the engine operation. All engine units are timed to the crank angle pick-up sensor also called the engine timing unit. The laser diagnostical system is set to a constant frequency and triggered through the engine timing unit. Both time signals are independent of each other. Upon start trigger (issued by the engine timing unit), the camera will use the next available read-in sequence to start the recording. Ultimately, if the start trigger occurs at the beginning of a read-in sequence the offset between the actual recorded image and the crank angle will be a maximum of 1° CA (engine speed is 1000 rpm and camera speed is 12 kHz in double frame mode). At higher engine speeds the mismatch is increased, given a constant recording rate. This temporal mismatch is called a jitter which can occur during every recording of each cycle when high-speed measurements are recorded. Figure 3.7 shows a schematic time scale of the possible jitter combinations.

Class 2 error sources

- **Droplet distribution:** As mentioned in chapter 2.3.2, the algorithm performs stable with a droplet displacement of $\sim 1/4$ of the interrogation window size (in coherence to the time separation value Δt) between two raw images. The seeding introduced at the inlet manifold should allow for a homogeneous distribution with the corresponding droplet displacement.

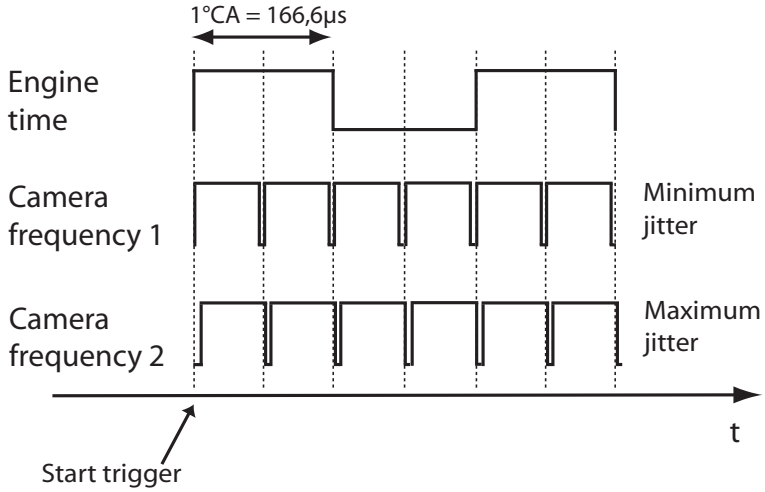

Figure 3.7: Time scales of the engine, the camera and the possible jitter combinations.

Too little seeding or accumulations within the cylinder produce deposits on the quartz glass ring, thus resulting in insufficient vector fields or too few vectors for a reliable statistical analysis.

- **Droplet deposits:** The droplet deposits on the quartz glass ring limit the number of consecutive cycles recordable. The engine in this thesis allowed ∼50 cycles to be recorded before exhibiting gradual contamination, while further cycles showed large quantities of seeding material on the quartz glass ring. To reduce this error source and ensure reproducible cycles, the quartz glass ring was cleaned before every recording.

3.3.3 Post-processing procedure

The flow field of each engine configuration (e.g. engine speed, charge motion, etc.) was recorded in three independent datasets containing 50 consecutive cycles spanning from 180 - 60° CA. The statistical analysis was based on 100 cycles taken from the recorded datasets (equally distributed ∼33 cycles from each dataset).

Quantitative analysis: Kinetic energy

The instantaneous flow fields recorded at different in-cylinder conditions were compared by calculating the spatially-averaged kinetic energies and turbulent kinetic energies. The kinetic energies were calculated using:

$$E = \sum_{i=1}^{n_x} \sum_{j=1}^{n_y} \frac{1}{2} \frac{u^2_{x\,(x_i,y_j)} + u^2_{y\,(x_i,y_j)} + u^2_{z\,(x_i,y_j)}}{n_x \cdot n_y}, \tag{3.1}$$

with u_x, u_y, and u_z as the velocities (u_x and u_y as in-plane velocities and u_z as the out-of-plane velocity). The number of vectors is calculated by n_x and n_y [21].

Accordingly, the phase-averaged velocity field $\overline{u_i}$ was calculated for each individual crank angle. Using the Reynolds-decomposition $u_i^{'} = u_i - \overline{u_i}$, the fluctuations $u_i^{'}$ of the velocity fields are determined. They are used in equation 3.2 to calculate the spatially-averaged turbulent kinetic energy:

$$k = \sum_{i=1}^{n_x} \sum_{j=1}^{n_y} \frac{1}{2} \frac{u'^2_{x(x_i,y_j)} + u'^2_{y(x_i,y_j)} + u'^2_{z(x_i,y_j)}}{n_x \cdot n_y}. \tag{3.2}$$

To test the significance of the stereoscopic PIV data, it was compared to conventionally recorded two-component PIV with the assumption of isotropy. Here, the out-of-plane velocity u_z was calculated by linear superposition of the in-plane velocities according to:

$$u_z = \frac{1}{2}u_x + \frac{1}{2}u_y. \tag{3.3}$$

The fluctuating velocities were calculated accordingly.

Quantitative analysis: Vortex tracking

The large scale flow structures produced with e.g. a tumble charge motion exhibit an identifiable vortex core. Its location and movement within the field of view is used to characterize each single cycle as the fluctuating coordinates indicate cyclic variations. The vorticity (equation 2.11) of the velocity fields (only in-plane velocities) was calculated using a least-squares approach. Non-existent values were interpolated using the surrounding values to obtain a consistent vector field. The maximum vorticity was located adhering to the requirements that the velocities within the vicinity exhibit larger values than the velocity at the peak vorticity.

3.4 Spray / flow field interaction measurements

The main focus of the spray / flow field measurements was the analysis of the interaction between the stratified fuel injection with the flow field. A detailed investigation of the flow field and its impact upon subsequent spray dynamics prior to combustion was conducted. To characterize the influences of both, the temporally resolved velocity measurements were recorded $\sim$35° CA before the start of injection. This way the transient flow field dynamics and their respective cyclic variations were recorded for each single cycle. Subsequent spray injections were recorded and thus a thorough view of the interaction process between flow field and spray was possible.

3.4.1 Experimental setup

The engine setup is described in section 3.1 with the following modifications. The spark plug was removed for the present study to enable reproducible flow fields. The engine was motored with

nitrogen as the intake medium. A reference fuel with a low percentage of aromatics similar to regular gasoline was used to simulate the physical properties (i.e. viscosity, enthalpy of vaporization, etc.).

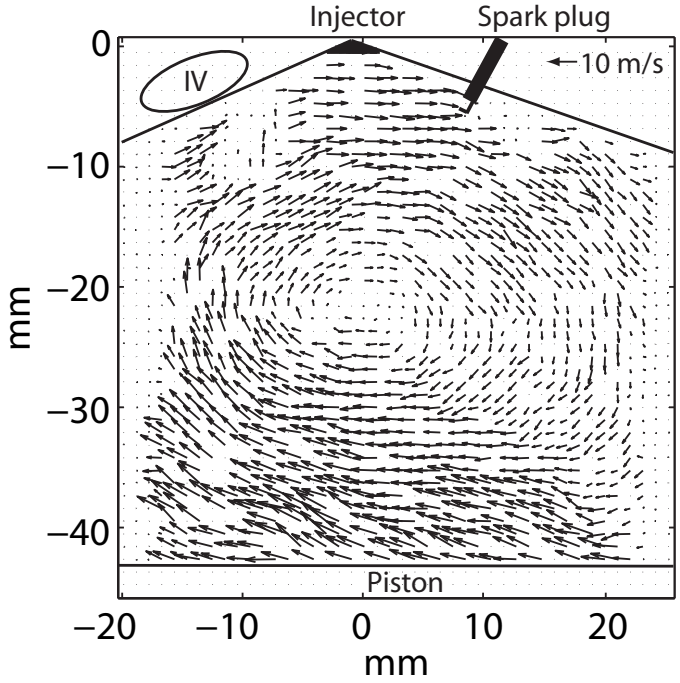

Figure 3.8: Field of view of in-cylinder flow field / spray injection; IV: inlet valve; Spark plug depicted only for orientation.

The instantaneous flow field was recorded using two-component PIV. A frequency-doubled, dual-cavity Nd:YVO_4 slab laser (Edgewave IS4-DE) was operated at 532 nm with a pulse energy of 0.7 mJ / pulse. The repetition rate was set to 6 kHz with a pulse-to-pulse separation of 10 - 40 μs depending on engine speed and the investigated charge motion. The laser beam was formed into a light sheet with three lenses (-20, 300, and 500 mm, all cylindrical) and then guided through the piston window intersecting the cylinder (see figure 3.1). The light sheet was $\sim$44 mm wide and $\sim$1 mm thick. Mie-scattering of seeded oil droplets was recorded perpendicularly through the quartz glass ring using a single CMOS camera (Photron SA1). The pixel-resolution of all recorded images was 62.5 μm and the field of view spanned 688 x 704 px, resulting in a field of view of 43 x 44 mm^2. An example flow field including the positions of the engine components is shown in figure 3.8.

The aerosol was produced with an air pressurized generator (Palas AGF 10D-S) using hydraulic oil (Liquimoly) as seed. The size of the droplets was $\sim$1 μm to ensure low particle response times. Droplets were seeded into the manifold inlet $\sim$0.6 m upstream of the inlet valves. This guaranteed a homogeneous droplet distribution within the cylinder.

The recordings were taken within the compression stroke prior to and during injection. The spray injection was recorded for $\sim$5° CA, while the flow field was recorded for $\sim$35° CA prior to injection. Since the recordings were done within the same cycle, flow field and its impact on the spray development are directly linked to each other. To achieve good statistics each dataset per engine speed included $\sim$100 - 200 cycles (engine speed dependent).

Synchronization of the camera and the laser with the engine speed was done with an analog / digital converter (LaVision). The increment signals for each crank angle and the main engine cycle trigger were used to fire the laser and record the images without occurrence of jitter. The engine speed was nominally stable with only minor cyclic variations. This is normally within 1% of the engine speed but running a camera / laser system with a fixed frequency bares indifferences to the synchronization. The periodic read-out / read-in sequences of the camera are interrupted by a random reset signal which also triggers the laser. Thus, a direct synchronization with the transient start trigger was possible.

Data processing

The evaluation of the PIV data was based on a PIV-algorithm presented by Böhm [62]. Using decreasing multi-pass iterations, the PIV images were cross-correlated with window shifting and a final grid consisting of 16 x 16 px. No overlap was used and the final resolution of each interrogation window was 1 x 1 mm. The number of valid vectors depends greatly on the gas densities and the operational conditions within the cylinder. The quality of the vector fields was very good at early stages of the compression stroke. Spurious vectors appeared predominantly at the edges (piston crown, inlet and outlet valves) caused by reflections. A rapid decline in signal quality was visible near top-dead-center (TDC). Here, high temperatures caused the seeding oil to evaporate. Another influence on the decline was accumulated deposits of injected fuel on the quartz glass ring. A trade-off between the number of recorded cycles and signal quality was made to ensure valid flow fields throughout each recording. To accurately filter the vector fields, a set of filters based on the signal-to-noise ratio, the correlation peak height as well as a comparison with the local neighboring vectors removing inconsistent vectors was used. Spray injection was recorded using Mie-scattering of the liquid fuel.

3.4.2 Error sources of spray / flow field measurements

Most of the error sources and considerations for the flow field recordings are the same as for the three-component measurements mentioned in section 3.3.2. Therefore, only the spray specific error sources are listed.

Class 1 error sources

- **Injector:** To be able to compare different spray shapes, the orientation of the injection nozzle requires special attention, as well as the injection pressure and injection timing (synchronization of start of recording and start of injection).
- **PIV evaluation**: No distortion correction of the raw images was done because the aberrations in two-dimensional recordings (straight alignment of object plane / image plane) were assumed negligible. Further, the PIV algorithm used to obtain the in-plane velocity components is based on MATPIV [113]. It is detailed by Böhm [89]. Some short-comings compared to the algorithm presented in the section of the flow field recordings are e.g. no pre-processing, and no interrogation window deformation.

Class 2 error sources

- **Pixel saturation:** The CMOS camera used in the experiments showed an over-saturation of the pixels during fuel injection. During it vertical segments of the CMOS sensor are not sensitive to the different signal levels (spray / Mie-scattering of droplets). Portions of the camera sensor beneath the spray are not able to record Mie-scattering, thus no velocity field is displayed. Outside of the spray, the normal sensitivity of the sensor is readily available.

3.4.3 Post-processing procedure

To characterize the spray, the evaluation was based on the penetration depth and the spatial drift of the spray towards the right side of the injector axis. This asymmetry was not a feature of the injector but was caused by directed in-cylinder flows such as an induced tumble charge motion. The drift of the spray, D, was defined as the ratio of the area left A_l of the injector center line (vertical line in figure 3.9) relative to the complete area $A_l + A_r$ of the spray as shown in equation 3.4:

$$D = \left(0.5 - \frac{A_l}{A_l + A_r}\right) \cdot 100. \tag{3.4}$$

Negative values of D present an asymmetrical movement of the spray to the left and positive values vice versa.

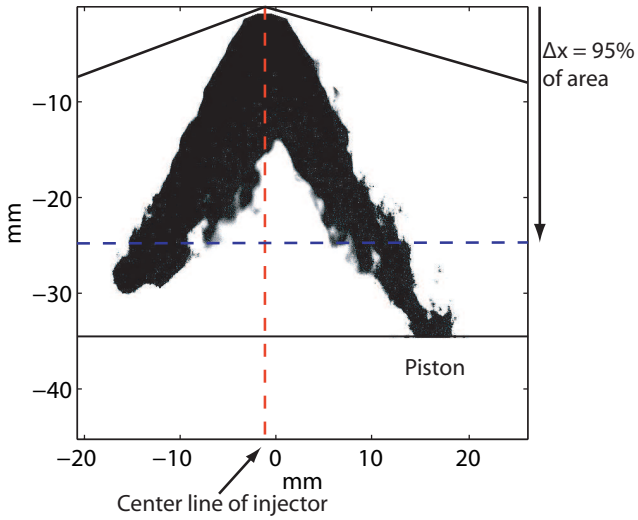

Figure 3.9: Field of view of in-cylinder flow field; IV: inlet valve

The spray penetration depth was defined to be the vertical displacement of the spray until 95% of the spray area was reached. By this definition the spreading of the fuel is evaluated rather than the spray tip with the farthest penetration that carries only minor fractions of the injected fuel [114]. This way, elongated strains of different spray shapes were excluded for better comparisons.

3.5 Fuel distribution measurements

The analysis of the fuel distribution inside the cylinder is especially important to localize accumulations of fuel (rich pockets) and characterize the homogeneity of the fuel distribution inside the cylinder when fuel is injected directly. It was measured with laser-induced fluorescence by excitation of tracer molecules within the reference fuel. The composition of the reference fuel CEC RF 08-A-85 included the tracer molecules (factory composition), hence no tracer components were additionally added. Although not certified, the effect of the assumed tracer is similar to toluene as strong oxygen-quenching is noticeable.

3.5.1 Experimental setup

The main engine setup is described in section 3.1. Additionally, the inlet manifold was preheated to 55° C to ensure almost homogeneous mixing while using the port fuel injection setup. Besides the oxygen sensor (Bosch LS7151) used within the exhaust gas system to determine the equivalence ratio, a special spark plug (LaVision) was used redundantly by measuring the absorption of hydrocarbons [46]. Within the combustion chamber the spark plug was arranged to have the lateral electrode parallel to the laser sheet (see figure 3.10). The laser sheet bisected the spark plug center, thus shadowing the fluorescence signals behind the electrodes. All recordings were taken within a nitrogen atmosphere to avoid quenching of the fluorescing fuel by oxygen. To ensure specified engine conditions (especially a stable preheating of the inlet manifold) the engine was motored a minimum of ∼10 minutes before recordings were taken. Furthermore, after each recording, all glass components were cleaned to secure reproducible conditions.

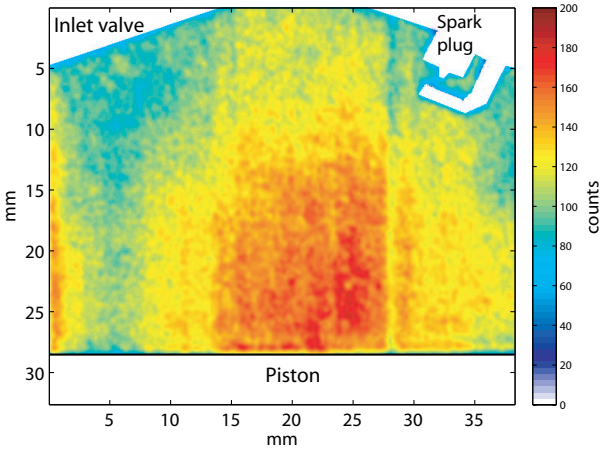

Figure 3.10: Example raw image of the LIF signal with the port-fuel injection system. Engine parameters: 1000 rpm, neutral charge motion, injection timing 360° BTDC, global equivalence ratio = 1 (stoichiometric).

An all-solid state diode pumped Nd:YAG slab-laser (Edgewave IS8II-DE) was operated at 6 kHz with an average laser energy of 8 mJ / pulse. The laser was equipped with an externally attached BBO crystal to double the fundamental wavelength of 532 nm into 266 nm resulting in ∼0.5 mJ / pulse [39]. The laser energy was recorded simultaneously with a high-speed energy meter

(LaVision) and a redundant photodiode (Thorlabs). The light sheet width of 35 mm with a thickness of 0.5 mm was guided with a 45° mirror into the combustion chamber. A high-speed CMOS camera (Photron SA1) equipped with a dual-stage intensifier (LaVision) was used to record the fluorescence signals. The settings of the intensifier were 50% gain (quantum efficiency of the intensifier at 266 nm was ∼10%) and a gate of 3500 ns. To reduce the influence of reflections a UV-enhanced lens (Bernhard Halle Nachfl. GmbH, f/# = 2, f = 100 mm) was used to collect the photon signal. A razoredge filter (> 267 nm, Semroc) and an ultraviolet transmitting filter (Schott UG11, 12 mm) suppressed the excitation wavelength efficiently. In figure 3.10, an example raw image is shown which also presents the recorded FOV.

Data processing

Image processing was necessary to reduce noise and enhance signal quality. The background noise of the raw images was reduced by subtracting averaged background images without fluorescence signal. The averaged background images (images from 100 cycles) were recorded at the same crank angle with the same procedure as the measurements with fluorescence signals, thus the spatio-temporal domain is the same (no phase shift). In order to suppress the influence of a transient overshoot of the intensifier at the beginning of each recording, the first 2000 images were not used in the analysis [40]. To correct for laser energy fluctuations, the signal intensity of each pixel of each image was corrected by a reference to laser pulse energy ratio. A Gaussian average filter (5 px) was used to smooth the pixel intensities.

3.5.2 Error sources of air / fuel distribution measurements

Class 0 error sources

- **Injection pressure:** During the measurements, the injection pressure was stabilized using a constant pressure chamber. Small perturbations within the nitrogen feed system are balanced by the large surface ratio between the outlet nozzle of the nitrogen feed and chamber diameter.
- **Laser beam profile:** The influence of the laser beam profile is negligible since only relative data was used. The characteristical profile is thereby compensated. No stability problems of the profile occured during the measurements.

Class 1 error sources

- **Intensifier:** The intensifier coupled to the camera presents overshot effects which result in overestimation of fluorescence intensities during early periods of each single recording [40]. A systematic error would result when using the complete recording. To reduce this influence, the first 2000 images were not used in the analysis.
- **Tracer distribution:** A homogeneous distribution of the tracer within the fuel is necessary to achieve realistic recordings. The density of the tracer needs to be relatively close to the density of the used fuel. This is only mentioned for completeness when adding an additional tracer component which is not part of the original fuel composition.

- **Absorption:** A zero order calibration scheme was applied to obtain qualitative data of the spatial mixture composition. However, a systematic offset during stratified operation is possible as absorption effects occur in vertical direction (inhomogeneous fuel distribution, see figure 3.11).

Class 2 error sources

- **Fuel deposits:** The deposits of fuel onto the quartz glass cylinder required it to be cleaned before each recording to ensure reproducibility. Further, different charge motions presented higher contamination rates (e.g. tumble charge motion). These recordings were not used in a statistical analysis, but rather recorded for qualitative reasons.
- **Pressure / temperature:** As stated by Schulz [34], the intensity of the fluorescence signal of toluene is strongly pressure and temperature dependent (see equation 2.31). Especially the fluorescence quantum yield, mainly influenced by the quenching (reduced to a minimum because of the nitrogen atmosphere) and pre-dissociation processes, employs constraints to the evaluation of the recordings. However, as only relative signal intensities are used for the calculation of the equivalence ratio, the influences are systematic. Further, the investigation of the fuel deposits on top of the piston crown and the fuel distribution within the cylinder are also prone to systematic errors, albeit relatively. A reference quantification of the errors was not possible.

3.5.3 Post-processing procedure

In general, the application of tracer PLIF is a common technique in laser diagnostics to measure local equivalence ratios and / or temperatures [115, 34, 116]. Calibrating the equivalence ratio, the signal intensity within known fuel distributions (e.g. homogeneous equivalence distribution provided by a port fuel injection system) is used as a reference (I_{ref}). Recordings with unknown fuel distributions (I_{inst}) within the combustion chamber (e.g. with a direct-injection system) can then be referenced and the equivalence ratio ϕ determined. Equation 3.5 is only valid if in-cylinder pressure and temperature conditions are identical during both engine runs (calibration of I_{ref} and actual measurements I_{inst}):

$$\phi \propto \frac{I_{inst}}{I_{ref}}. \tag{3.5}$$

Figure 3.10 presents a typical raw image of the PLIF signals with port fuel injection. Fluorescence signals decrease along the laser light path because of absorption effects. Figure 3.11 (left) shows an average image over 50 cycles of the PLIF signals with identical engine parameters as in figure 3.10. Assuming perfectly homogeneous conditions, the average fluorescence signals are used as the calibration matrix for the recorded crank angle. In contrast, figure 3.11 (right) shows a raw image of PLIF signals with direct-injection. Large scale heterogeneous structures are visible as fluorescence signals indicate different absorption intensities along the laser light path. Strong fluorescence signals are visible on the piston surface (left) indicating wall wetting.

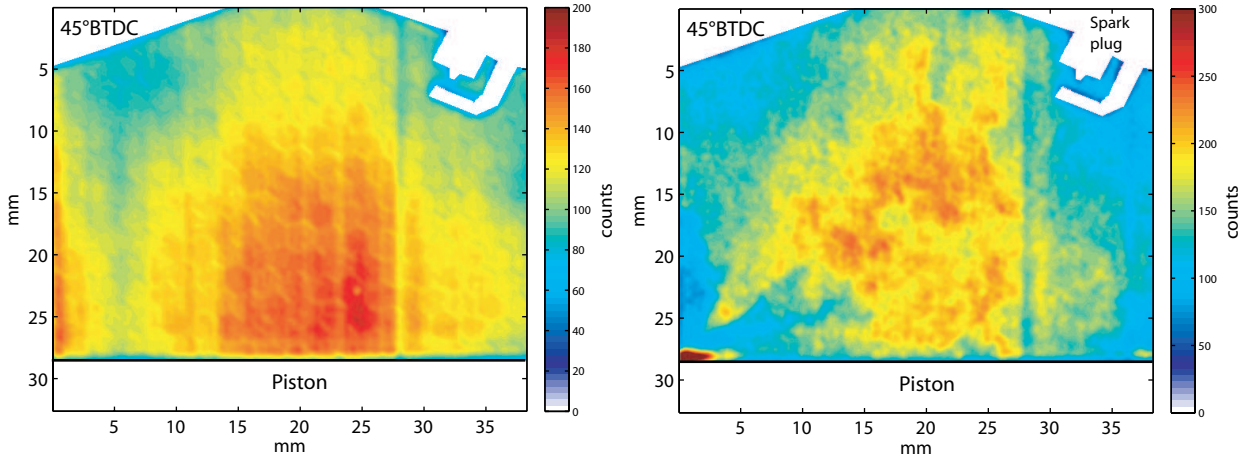

Figure 3.11: Left: Average intensity map of the field of view with port fuel injection. Right: Example raw image of the field of view with direct-injection. Engine parameters: 1000 rpm, neutral charge motion, injection timing 300° BTDC, global equivalence ratio = 1 (stoichiometric).

To attribute fluorescence signals of the instantaneous fuel distribution to a determined equivalence ratio a calibration procedure was developed. First, the engine was operated with a port fuel injection system. The fuel was injected ∼0.6 m upstream of the inlet valves. The temperature within the manifold inlet pipe was conditioned to 55° C (during the injection, a temperature drop of ∼5° C was measured because of the evaporation enthalpy). This procedure ensured a homogeneous and known equivalence ratio within the combustion chamber. For a fixed equivalence ratio, the PLIF signals were recorded for two independent engine runs. In a first run, the engine was operated with air and fired. The equivalence ratio was determined with a conventional oxygen sensor placed ∼0.15 m behind the exhaust valves. In a second run, for otherwise identical conditions, the air was replaced by pure nitrogen and PLIF signals were recorded. Combining both recordings, a spatio-temporal calibration matrix of PLIF-signals assigning each pixel / intensity combination a certain equivalence ratio was obtained.

The fuel distribution with the direct-injection system was characterized by using the recorded calibration matrix. First, the engine was operated in firing mode to retrieve the amount of fuel needed to achieve certain global equivalence ratios (also measured with the oxygen sensor). Secondly, for otherwise identical conditions, the engine was motored and PLIF signals were recorded within a pure nitrogen atmosphere. For comparability, during the operation with direct-injection the manifold inlet temperature was reduced to 50° C alluding to the evaporation enthalpy while operating with the port fuel injection system. While the engine was operated in firing mode, both injection systems were set to operate with an indicated mean effective pressure of ∼3 bar and a corresponding coefficient of variation of 2%.

3.6 Flame kernel development

The transient flame kernel development was recorded using laser-induced fluorescence by excitation of OH-radicals. It was used to localize the flame front within the cylinder during combustion

Table 3.2: Parameter configuration of the engine operating point. Engine times are measured in ° CA and are relative to the top dead center of the compression phase.

Parameter	Setting / Value
Engine speed [rpm]	1000, 1500, 2000
Compression ratio	8.24
Charge motion	tumble, swirl, neutral
Fuel/air ratio [-]	0.75 - 1.25
Rail pressure [MPa]	10
Manifold inlet pressure [mbar]	300 - 1500
Skip fire ratio	1:3

and identify cyclic variations as well as the influence of exhaust gas recirculation onto the flame front.

3.6.1 Experimental setup

Temporally resolved OH-PLIF was observed through the piston window using a 45° mirror located within the extended piston as shown in figure 3.12. The engine is similar to the engine described in section 3.1 and only the most important operating parameters for the present study are listed in table 3.2. A standard outward opening annular orifice injector with a piezoelectric actuator was applied. The fuel used was similar to standard gasoline (Ökokraft4T, Haltermann Hamburg), but with only a low percentage of aromatics. This was necessary to avoid superposition from LIF signals of other species.

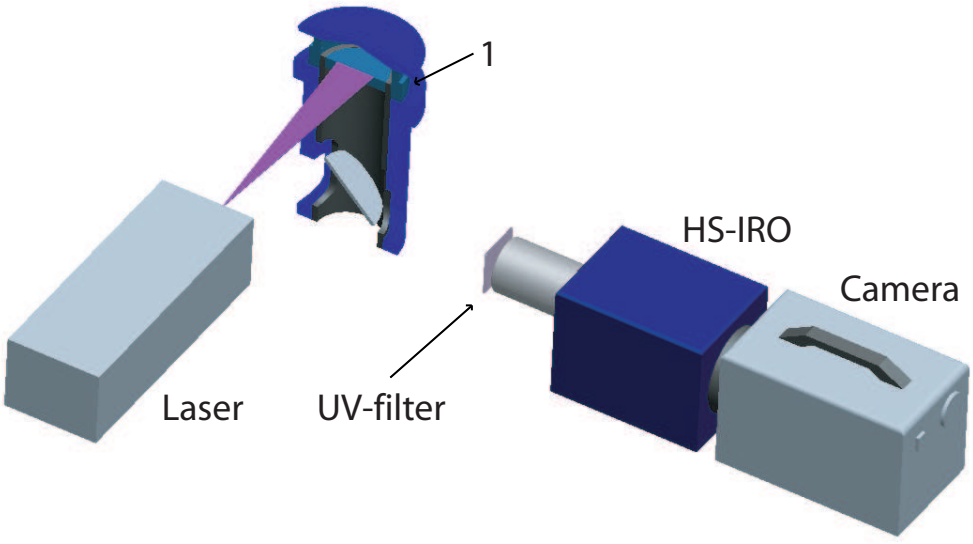

Figure 3.12: Schematic of the engine / camera / laser arrangement in the swirl plane configuration; 1: quartz glass ring.

Because of high temperatures during the fired mode, the engine was skip fired with a ratio of 1:3 (one cycle fired, three cycles motored). Furthermore, the charge time of the spark plug was

adjusted to ∼1.5 ms. This was done to protect the intensifier from over-saturation effects by the light intensity of the spark. However, the second reason was to reduce the time between ignition of the air / fuel mixture and start of recording of the flame front to be able to capture the early flame propagation. Amplifying the ignition spark would have caused irreversible damage to the intensifier. In early tests, the ignition of the engine was thoroughly inspected for such a short spark duration. In a parametric study synthetic external exhaust gas recirculation (EGR) rates were varied from 0 to 20%. The composition of exhaust gases was mimicked by N_2 and CO_2 in a mixing ratio of 9:1.

OH radicals were excited at the $Q_1(6)$ line within the $A^2\Sigma^+ \leftarrow X^2\Pi(1-0)$ band using a frequency doubled dye laser (Sirah Allegro). The dye laser was pumped by a frequency doubled Nd:YAG laser at 532 nm (EdgeWave). The pump laser was operated at a repetition rate of 6 kHz. Average pump pulse energies and pulse lengths were 5.3 mJ / pulse and ∼10 ns, respectively. To lower the peak intensities at the dye laser optics, the beam of the pump laser was expanded by a telescope with an expansion factor of 1.4. Resonator and amplifier of the dye laser were operated with Rhodamine 6G dissolved in ethanol. Dye laser radiation at 566 nm was frequency doubled using a BBO crystal. First and second harmonics were separated by four Pellin-Broca prisms. At 283 nm average pulse energies of up to 360 μJ / pulse were achieved at a repetition rate of 6 kHz (2.15 W quasi-cw).

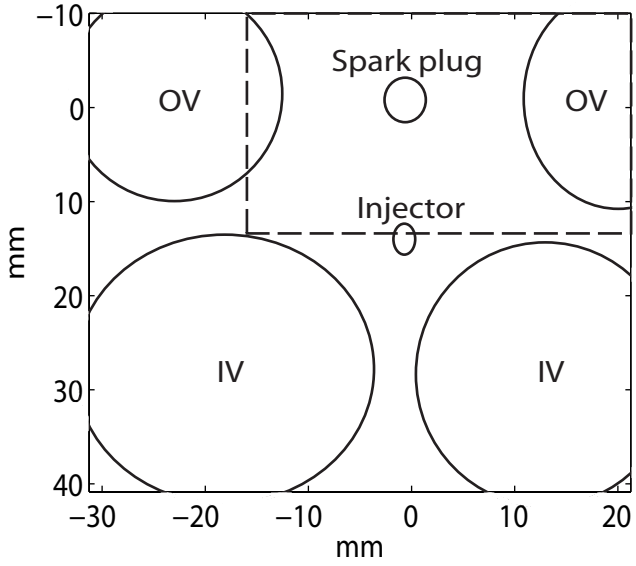

Figure 3.13: Field of view within the cylinder. Intake valves (IV) are in the lower part and exhaust gas valves (OV) at the upper. The injector is mounted centrally and the spark plug is located between the exhaust valves. The dashed rectangle shows the enlarged portion seen in figures 4.43 - 4.44.

A laser light sheet was formed using a combination of three lenses (f_1 = 1000 mm cylindrical; f_2 = 208 mm spherical, f_3 = 250 mm spherical). The light sheet entered the cylinder through a quartz glass ring and was aligned horizontally just above the top dead center (TDC) position of the piston (see figure 3.12 and x-direction in figure 3.14). At the measuring plane, the light sheet was 54 mm wide and approximately 200 μm thick. Due to reflective losses at the lenses and the quartz glass ring pulse energies decreased to 290 μJ / pulse inside the cylinder. Vertical and horizontal

alignment of the laser profile were checked regularly between single engine recordings. Fluorescence around 308 nm was collected using a UV lens (Bernhard Halle Nachfl. GmbH, f = 100 mm, f/# = 2). A band pass filter with 80% transmission at 308 nm (mso Jena) was used to reduce spuriously scattered light and flame luminosity. PLIF signals were recorded by a lens-coupled dual-stage intensified CMOS camera (Photron SA1). The intensifier consisted of a multi-channel plate followed by a booster (LaVision HS-IRO). It was operated at 65% gain and a gate width of 100 ns. At 6 kHz, 992 x 1024 px of the CMOS chip were active resulting in a field of view of 53 x 54 mm (see figure 3.13). The dashed rectangle presents the investigated area used for the statistical analysis in section 4.4. Emphasizing signal yield, figure 3.14 presents a raw image selected randomly from a sequence consisting of thousands of frames.

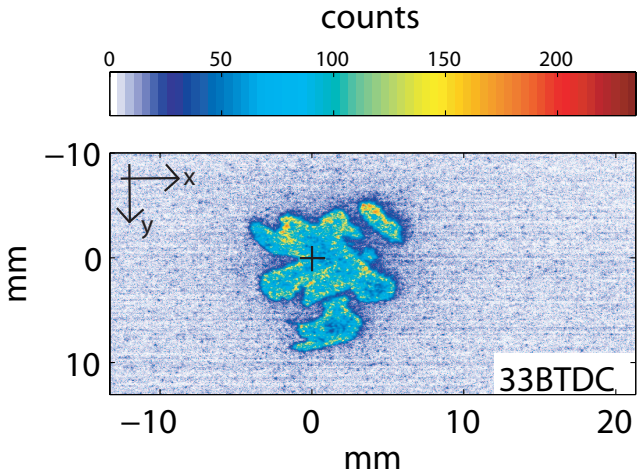

Figure 3.14: Example enlarged raw image with the cross marking the position of the spark plug (dashed rectangle of figure 3.13). Colors represent intensities, but are only qualitative.

The camera's on-board memory was limited to 8 GB resulting in 5400 images per sequence. Due to this storage capacity during a single engine run lasting approximately 21 s 180 sequential cycles were recorded enabling statistical analysis. Camera and intensifier were synchronized with the engine timing via the engine timing unit.

Data processing

A data processing procedure was applied to the raw images (figure 3.15, a) to extract the local flame front. In a first step a cuvette set atop the piston was used to examine and correct the laser profile [67]. Secondly, an averaged background image was subtracted. Further denoising was done with a median filter (figure 3.15, b). In a final step, to clearly differentiate between burned and unburned regions each image was evaluated with a histogram of the pixel intensities to deduce an adaptive threshold, which was set as the minimum between the bimodal distribution (process shown in figure 3.16). The binarized images were then used for all further analyses (figure 3.15, c).

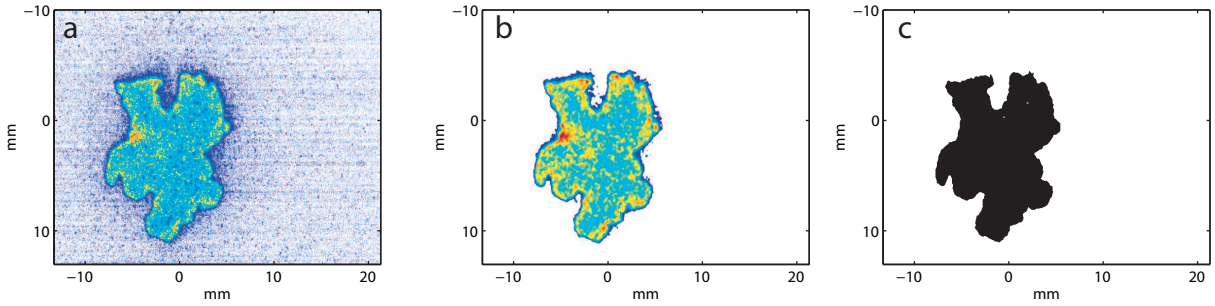

Figure 3.15: Post-processing of OH-Plif data. a) raw image; b) background subtraction and median filter; c) adaptive threshold and binarization.

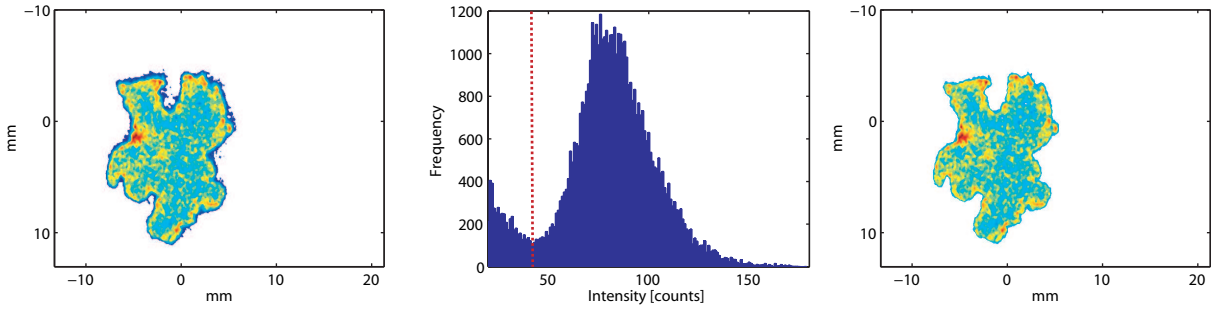

Figure 3.16: Example of adaptive threshold. Left: Fluorescence signal with background subtraction and median filter. Middle: Histogram of intensities with bin size according to the maximum signal intensity with an increment of 1. Right: filtered image.

3.6.2 Error sources of OH-PLIF measurements

Class 0 error sources

- **Injection pressure:** The injection pressure was generated using a reciprocating piston pump. Below a reference pressure, the piston would reinduce the set pressure. Single injections occur below the reference pressure (deviation of $\sim$10 bar at 200 bar). The effects are referred to as marginal since only homogeneous injection timings are taken into account and thus residence times are long enough.

Class 1 error sources

- **Light sheet:** The positioning of the laser light sheet was susceptible to minor perturbations as the laser system was installed spatially separate and not in the vicinity of the engine (distance $\geq$ 5 m). Conventionally, the laser path between laser and measurement plane is ideally small as further distance increases divergence and energy losses. The systematic error is negligible, since the error source is only relative.
- **Laser energy:** The energy fluctuation of the dye-laser is directly linked to the photon emission intensities recorded. A sufficient SNR is required for automatic processing of the images.

- **Synchronization:** As seen with the timing sensitivity during the flow field measurements, the synchronization of the image recording and the corresponding pressure curves needs to be addressed. Only qualitative statements are obtainable as the certainty of the crank angle attribution is only within 0.5° CA.
- **Exhaust gas composition:** During the recordings with predefined synthetic exhaust gas, the composition of the mixture components is not realistic. Especially the water components of the exhaust gas were not addressed. Residual gas quantities within the cylinder from previous fired / skipped cycles are also not taken into account, resulting in a systematic offset.
- **Engine run time:** In order to record multiple consecutive engine cycles at a stable operation the engine was fired for at least 30 s non-stop. In effect, the temperature increase causes the seals between the quartz glass ring and the cylinder head to break and would damage the engine. To prevent this, the engine was run in skip fire mode during which only single cycles are fired and multiple cycles are motored. In turn, this results in a temperature gradient between the cylinder head and the quartz glass components. Further, it only approximates the realistic temperature gradients within a production engine. It also effects the residual gas composition as the gas composition when fired continuously is different. These effects were not taken into account.

Class 2 error sources

- **Spark plug charge:** In order to protect the multi-channel plate detector from accidental damage due to the light emission of the spark, the discharge time of the spark plug was reduced to a minimum. This effects the reproducibility of the ignition of the surrounding air / fuel mixture. A secure number of empirical tests were done, although an element of risk of a misfire (which would easily be ignited with a conventional amount of charge energy) remains.

4 Results and discussion

This chapter presents the results and discussion of the different experiments. The in-cylinder processes are isolated into flow field, spray / flow field interaction, fuel distribution, and flame kernel development sections. They are arranged according to their individual recording range, which also adheres to the consecutive engine stroke phases shown in figure 2.1.

First, the in-cylinder flow field is analyzed. It is the basis of the subsequent fuel distribution and combustion processes. Flow field images combined with statistical tools to investigate cycle-to-cycle variations (ccv) are presented. Influences of parametric variations of the in-cylinder flow motion (different charge motions, engine speed, etc.) are also detailed. Additionally, the measurement technique itself is analyzed in form of consistency and different calibration aspects.

The second section addresses the interaction of the flow field and the stratified spray injection (during the compression stroke). Focusing on the spray dynamics, statistical tools such as the penetration depth, spray drift, and kinetic energy are used for analysis of individual cycles. The influence of different charge motions, engine speeds, injector types (spray shapes), and injection pressures are investigated.

To analyze the fuel distribution within the cylinder, the third section presents laser induced fluorescence data. A calibrating method was adopted to determine the equivalence ratio when using the direct-injection system of the engine. Strong spatio-temporal in-cylinder variations are shown indicating a heterogeneous fuel distribution. Also, different engine configurations and their influences on wall-wetting are shown.

The last section presents the flame front propagation during combustion. It is the culmination of the before mentioned isolated processes. Data with different levels of exhaust gas recirculation (EGR) are presented. A comparison between laser diagnostical data and conventional pressure measurements is shown.

4.1 Flow field measurements

Overview

The in-cylinder flow field is an important cornerstone to the combustion process as it influences the fuel distribution and subsequent flame front propagation. Its highly transient nature and cycle-to-cycle variations (ccv) require a single cycle analysis. Phase-averaged flow fields recorded with conventional PIV at low speeds (below 50 Hz) are suitable to determine cyclic fluctuations of single cycles at one distinct crank angle, albeit without the desirable information about the flow field before and after the recording. Further, conventional PIV is only able to measure two velocity components u_x and u_y in a plane, thus neglecting the influence of the out-of-plane velocity u_z.

The presented stereoscopic PIV approach is able to determine all three velocity components in a plane at 6 kHz throughout the compression stroke from 180° - 60° BTDC. This enables a temporal resolution of one image per crank angle at 1000 rpm. The motored engine was operated with nitrogen (to avoid ignitable mixtures) without fuel injection nor ignition. Details of the engine setup and the characteristic parameter variations are addressed in section 3.3 and in the following subsections.

4.1.1 Validation of data

The presented data is validated by comparison with previous two-dimensional recordings performed by Müller [14] in 2008. In figure 4.1, the spatially-averaged, phase-averaged kinetic (left) and turbulent kinetic energy (right) calculated using equations 3.1 and 3.2 are shown.

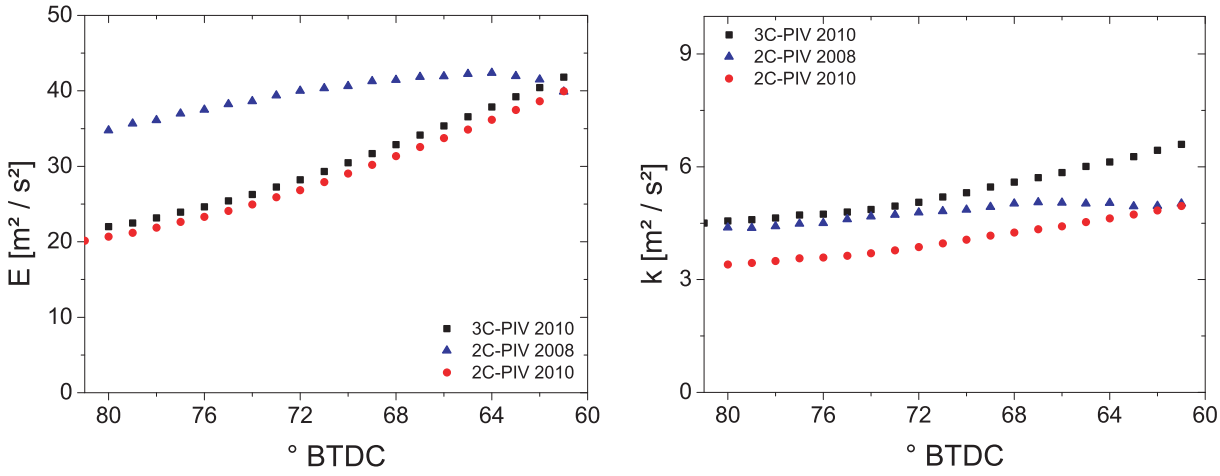

Figure 4.1: Comparison of spatially-averaged, phase-averaged kinetic (left) and turbulent kinetic energy (right). Engine parameters: 1000 rpm, tumble charge motion.

The comparison of both recordings is justified, since both cylinder head geometries, bore diameter and stroke length were equal as well as the engine speed, charge motion, intake pressure, etc. The tumble charge motion was chosen because of the dominant in-plane velocities and little out-of-plane motion (see section 4.1.2).

Further, Mie-scattering at the same symmetry plane inside the engine was recorded at the same repetition rate of 6 kHz. However, the compression ratio was 9.6 in 2008, while the presented recordings were taken with a compression ratio of 9.88 (cylinder pitch was modified). The recording range differed and only a 20° CA overlap between 80° - 60° BTDC is available.

The kinetic energy distribution between both recordings do not match. However, the magnitude of the kinetic energy is defined by the quadratic multiplication of the velocities. Therefore, the difference of $\sim 15\,{}^{m^2}/_{s^2}$ is only an increase of $\sim 2.7\,{}^{m}/_{s}$ to the average velocity. This inaccuracy can be attributed to the different compression ratio and calibration method. Further, two different evaluation algorithms (Davis 7.2 and MATPIV (for validation of code see [89])) were used, also adding to the discrepancies. In comparison, the fluctuations of the velocity field shown by the level of turbulent kinetic energy match in good agreement.

Confirmation of three-dimensionality of the flow motion

The flow motion inside the cylinder is three-dimensional, but only velocity vector fields in a distinctive plane are recorded. Therefore, before detailing individual flow motion characteristics, a confirmation of the three-dimensionality is shown by solving the conservation of mass equation (see equation 2.3).

The required density ρ is spatially uniform and independent of the convective transport. Therefore, it can be separated from ${}^{\partial \rho u_i}/_{\partial x_i}$. Mass loss because of blow-by is neglected. The time-dependence of ρ is further described by:

$$\frac{1}{\rho}\frac{\partial \rho}{\partial t} = \frac{1}{\Delta t}\frac{\rho_t - \rho_{t-1}}{\rho_t} = \frac{1}{\Delta t}\frac{\frac{p_t}{R_s\,T_t} - \frac{p_{t-1}}{R_s\,T_{t-1}}}{\frac{p_t}{R_s\,T_t}}. \tag{4.1}$$

Using the ideal gas law, the density ρ can be described by the intake temperature T and the in-cylinder pressure p. The subscript t denotes the time step, concurrent to the crank angle. R_s is the specific gas constant of air. The data points of the pressure signal were interpolated with a two-term exponential fit. The temperature T_t was estimated with a polytropic process ($\kappa = 1.4$ for nitrogen):

$$T_t = T_0 \left(\frac{p_t}{p_0}\right)^{\frac{\kappa-1}{\kappa}} \tag{4.2}$$

In figure 4.2 the strain rates ${}^{\partial u_x}/_{\partial x}$, ${}^{\partial u_y}/_{\partial y}$, ${}^{\partial u_z}/_{\partial z}$, as well as the density is plotted, according to the recorded flow fields with a tumble (left) and swirl charge motion (right). The error bars denote the cycle-to-cycle variations, rather than the measurement errors.

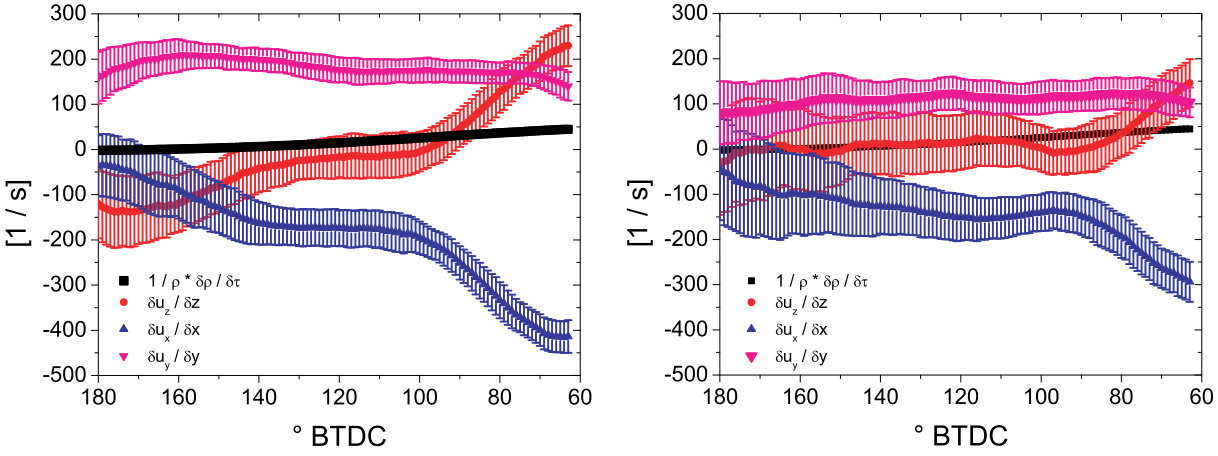

Figure 4.2: Normal strain rates of the phase-averaged velocity vectors fields at 1000 rpm. The error bars display the 1-σ deviation of all recorded cycles. Left: tumble charge motion; right: swirl charge motion.

Although 3C-PIV is recorded, only the in-plane velocities u_x and u_y are evaluable, since the derivative in z-direction is not available, thus the strain rate ${}^{\partial u_z}/_{\partial z}$ was calculated using equation 2.3. The instantaneous flow fields of the single cycles were, when necessary, interpolated (mostly in the later half of the stroke because of evaporating seeding) to obtain the derivatives.

During the recording range, the density change increases continually as the in-cylinder gas densities change according to the volumetric decrease due to the revolving piston. The change rate of $\partial u_y/\partial y$ is only little and shows a retarded cycle-to-cycle variation (relative small error bars). In contrast, the normal strain rate in x-direction and thus also in z-direction show opposite progression curves. Especially during the end of the recording range, the transport of fluid out of the measurement plane increases, as the normal strain rate in x-direction decreases accordingly (see the large scale in-plane flow structures as detailed in section 4.1.2).

Similarly, the normal strain rates of the swirl charge motion (right) also show an increased transport at the end of the recording range. However, the values are much lower indicating a more balanced transport through the measurement plane.

The analysis shown is only valid for the specific field of view (FOV) and can only be used as a qualitative analysis of the velocity gradients. Further, the normal strain rate $\partial u_z/\partial z$ is only estimated, but still suffices to confirm the three-dimensionality of the flow motion.

4.1.2 Analysis of charge motion influences

Three different charge motions were investigated which have the most prominent effect onto the in-cylinder flow motion. In chapter 2.1, the flow field patterns tumble, swirl, and neutral and their respective necessary mechanical adaptations to the intake manifold are presented. The following subchapters describe the spatial-temporal evolution and their characteristics of the flow field with the distinctive charge motion.

Tumble charge motion

The tumble charge motion induces a large scale transient vortex structure rotating clockwise within the symmetry plane (coincidental with the field of view). The flow motion is produced by inserting plates into the intake manifold blocking the lower half of both inlet channels. Three sample sequences of the flow field are shown in figure 4.3. The left column shows the phase-averaged velocity field of 100 cycles (vectors indicate the in-plane velocities u_x and u_y, color scale the out-of-plane velocity u_z), while the middle and right column present two arbitrary single cycles. The axis of the flow motion is perpendicular to the cylinder axis.

At early crank angles (160° BTDC) of the phase-averaged cycle, the tumble vortex center is not yet in the field of view. The location of it can be predicted to be on the left of the symmetry axis at 0 mm. As the compression stroke moves on, the tumble center shifts to the right and emerges into the field of view at a horizontal position of $\sim$10 mm at 100° BTDC. The movement then proceeds in reverse direction towards the symmetry axis of the FOV. Obviously, the trajectory of the tumble center is diagonally directed towards the inlet valves. Additionally, the out-of-plane velocity component of the phase-averaged data tends to be close to zero (within the limits of accuracy). This is expected for this specific field of view, albeit in other measurement planes within the cylinder different flow structures are possible. Especially the trajectory of the tumble center will differ, as will its orientation and velocity magnitude as described by Voisine [31].

In comparison to the phase-average data, two explicit compression strokes (cycle 15 and 72) are shown in the middle and right columns of figure 4.3. Albeit local flow differences are noticeable, the tumble vortex structure is clearly identifiable. The benefit of the time-resolved data is

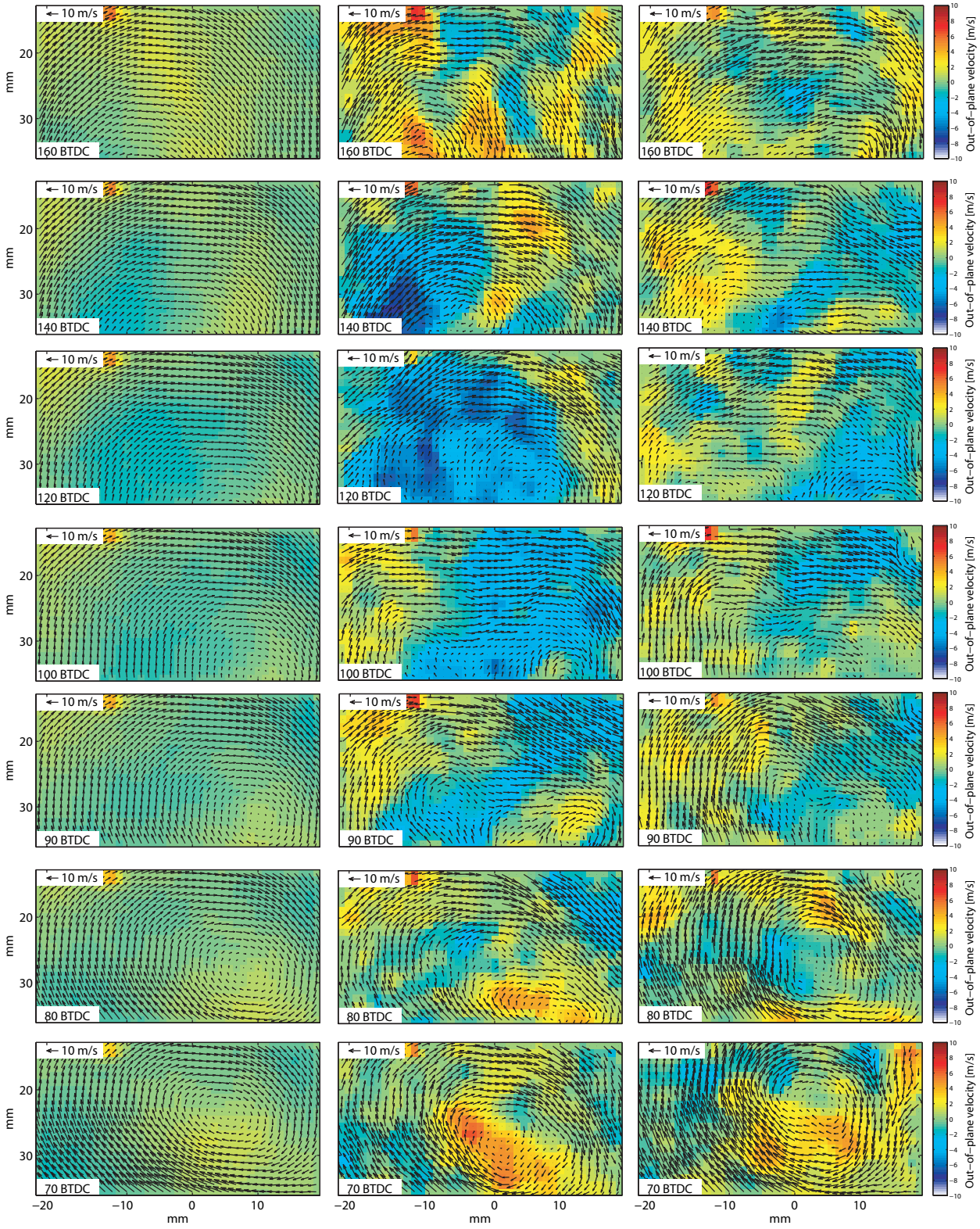

Figure 4.3: Velocity vector fields at an engine speed of 1000 rpm, tumble charge motion. Left: phase-averaged flow fields; middle: instantaneous velocity vector fields of cycle 15, right: cycle 72. Positive values of u_z are oriented out of the plane, negative values into the plane.

shown, as the rotating motion can be tracked throughout the individual cycles. In cycle 15, the inward velocities dominate during the early phase of the compression stroke (140° - 120° BTDC). Subsequently, the fully developed vortex core is visible at 90° BTDC. At 70° BTDC, the outward velocities increase at the lower portion of the tumble vortex structure. The same behavior is noticeable in cycle 72, although the vertical position of the tumble vortex center is closer to the cylinder head. In contrast to cycle 15, the strong inward velocities during the early stages of the cycle are not present.

The consistency of the recordings without sudden magnitude offsets in any of the three velocity components ensures a high level of repeatability of the flow field data. However, limiting the significance of it is the unfeasible differentiation between turbulent flow structures and cyclic variations, as both are superpositioned on each other. The intensity of the turbulent structures of the flow field influence the mixing processes of fuel and air, as well as the flame propagation. Isolating the origins of both would result in more predictability over the subsequent processes. Currently, this is matter of on-going research.

Using statistical tools, the crank-angle resolved, spatially-averaged kinetic energy along with the corresponding turbulent kinetic energy (see equation 3.1 and 3.2) of the presented cycles are shown in figure 4.4. In black, the spatially, phase-averaged kinetic energy shows decreasing values reaching a minimum at 90° BTDC, followed by a steep increase till $\sim$45 m^2/s^2. This behavior is expected as in later stages of the compression stroke the velocities increase due to the revolving piston (and so do the gas densities), thus the kinetic energy increases as well [14]. The temporal evolution of the flow field presented here cannot be generalized, since it is highly sensitive to the field of view. However, relative to the mean, the level of fluctuations (including cyclic variations and measurement in-precision) is around $\sim$30% as shown by the error bars[1] (1-σ deviation). This behavior is relatively independent of the crank angle and of the specific appearance of kinetic energy.

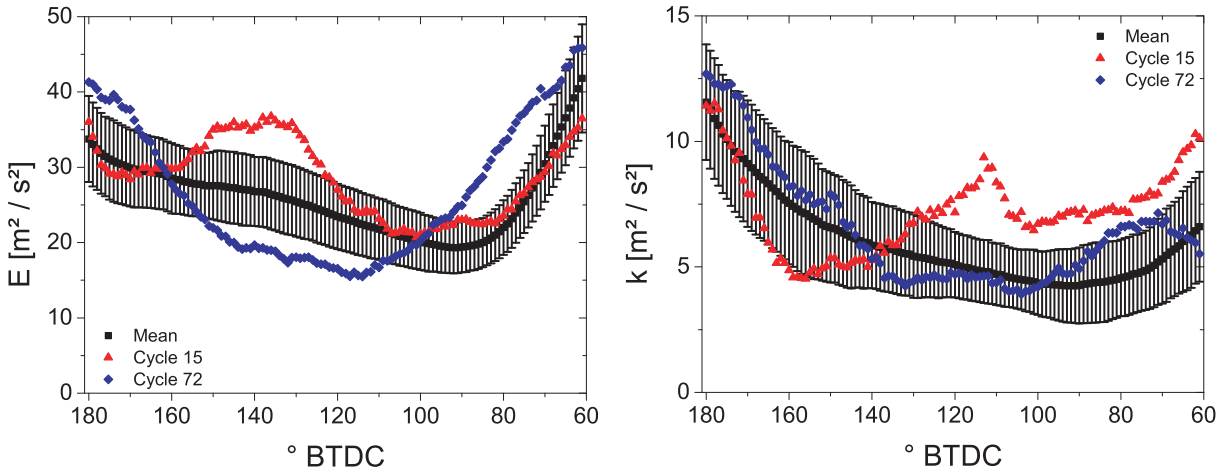

Figure 4.4: Left: Spatially-averaged kinetic energy E calculated from data recorded at an engine speed of 1000 rpm with a tumble charge motion. Phase-average data is presented in black (including 1-σ deviations), individual cycles 15 (red) and 72 (blue) are selected because of their significant deviations from the mean between 150°and 120° BTDC; right: corresponding turbulent kinetic energies

[1]The term 'error bars' is used due to its wide spread use, albeit the fluctuation level of the quantities is characterized.

Corresponding to the course of the kinetic energy, a similar progression is presented by the turbulent kinetic energy (figure 4.4, right). In contrast, the fluctuations shown by the error bars (1-σ deviation) are larger and reach $\sim$50%. This indicates increased cycle-to-cycle variations (ccv) compared to the large scale tumble motion, as the fluctuating velocities are directly linked to the turbulence field.

Cycles 15 and 72 were selected because of their unique deviation of the phase-averaged results, especially during 150° - 110° BTDC. Considering the recording range, these deviations are attributed to the turbulent intake flow. The above average level in kinetic energy between 150° and 110° BTDC of cycle 15 is due to a more uniform large scale flow structure (in the FOV). This anomaly is also noticeable by the level of turbulent kinetic energy. A similar behavior (level above average) is shown by cycle 72 at the end of the recording range. The large scale flow structure as shown at 70° BTDC in figure 4.3 is also reflected by an above average level of kinetic energy. Its prominent position within the recorded number of cycles however is retarded by the low level of turbulent kinetic energy in the same recording range.

Additionally to the inspection of the individual kinetic and turbulent kinetic energy levels of cycles 15 and 72, figure 4.5 shows histograms of the absolute velocity distribution for each crank angle. Noticeable in the early stages of the compression stroke, the velocity distribution of cycle 72 is broader with velocities ranging from $\sim$-5 to $\sim$15 $^{m}/_{s}$. Cycle 15 exhibits a narrower distribution clustered around 10 $^{m}/_{s}$. In the mid-section of the recording range, the velocity distribution of cycle 15 broadens and, hence a higher level of kinetic energy is presented. At the end of the recording range, both cycles exhibit broad velocity distributions.

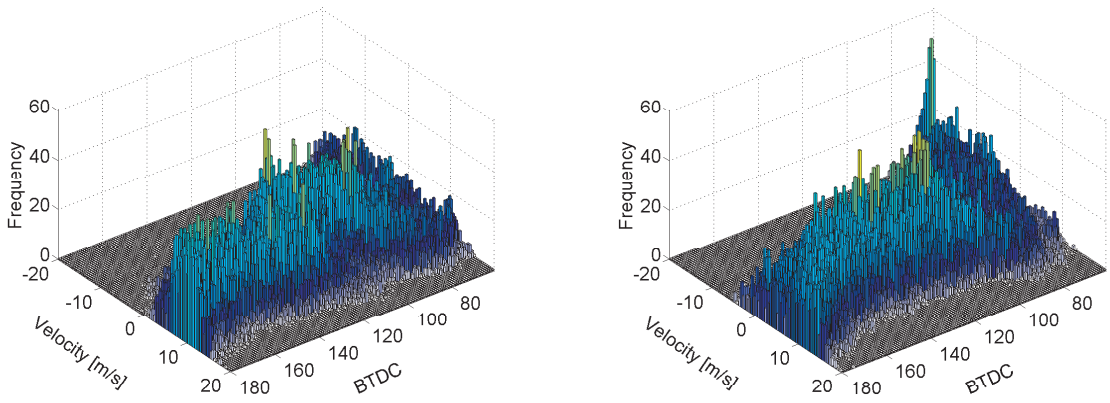

Figure 4.5: Histograms of the absolute velocity distribution of cycles 15 (left) and 72 (right).

Analysis of the influence of u_z

The contribution of the out-of-plane velocity u_z to all three measured velocity components is investigated by altering the calculation of the kinetic and turbulent kinetic energies. The use of the out-of-plane component to calculate the kinetic and turbulent kinetic energies is split into a) calculation of the statistics with all three velocity components (3C), b) calculation only with the in-plane components (2C), and c) linear superposition of u_x and u_y to form u_z (2C-iso).

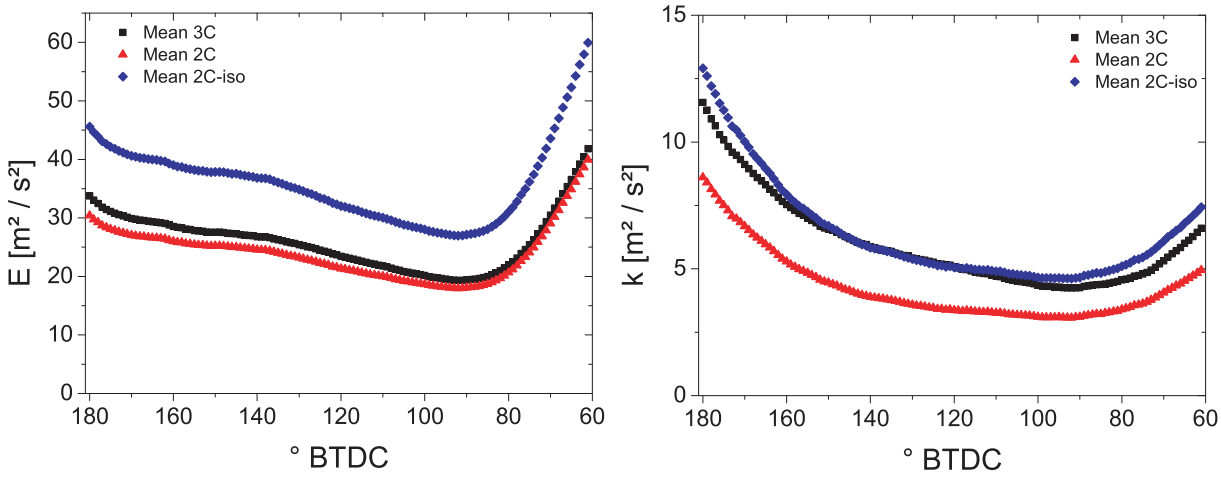

Figure 4.6: Comparison of spatially, phase-averaged kinetic energies E and k calculated with different methods. Engine speed: 1000 rpm, tumble charge motion.

In figure 4.6 the crank-angle resolved, phase-averaged kinetic and turbulent kinetic energies are shown. As shown clearly, the contribution of the out-of-plane component to the calculation of the kinetic energy is rather low (3C vs. 2C). This is expected, since the out-of-plane velocity distribution throughout the field of view is near zero (see figure 4.3, left column). Using the linear superposition of the in-plane velocities u_x and u_y, the kinetic energy levels are significantly higher ($\sim$30%). Accordingly, this overestimation is due to the higher structured flow field of the tumble charge motion, although this is only true for this specific FOV located in the symmetry plane of the cylinder. Thus, when only the kinetic energy is viewed, the effort for a three-dimensional PIV setup is unnecessary. In contrast though, the turbulent kinetic energy displays a different behavior as shown in figure 4.6, right. The fluctuations of the velocity field are present at all scales and compared to the mean flow field, their individual orientation is more isotropic (3C vs. 2C-iso). In turn, the turbulent kinetic energies calculated with only the in-plane velocities underestimate the values calculated with all velocity components. Depending on crank angle, the difference is up to $\sim$35%. The estimation of the fluctuating out-of-plane velocity component by linear superpositioning of the in-plane components shows a much better agreement when calculating turbulent kinetic energies with the actually measured fluctuating velocities. In contrast to the calculation of kinetic energies with superposition (3C vs. 2C-iso), at a fluctuating level, measuring all three-velocity components indicates its importance.

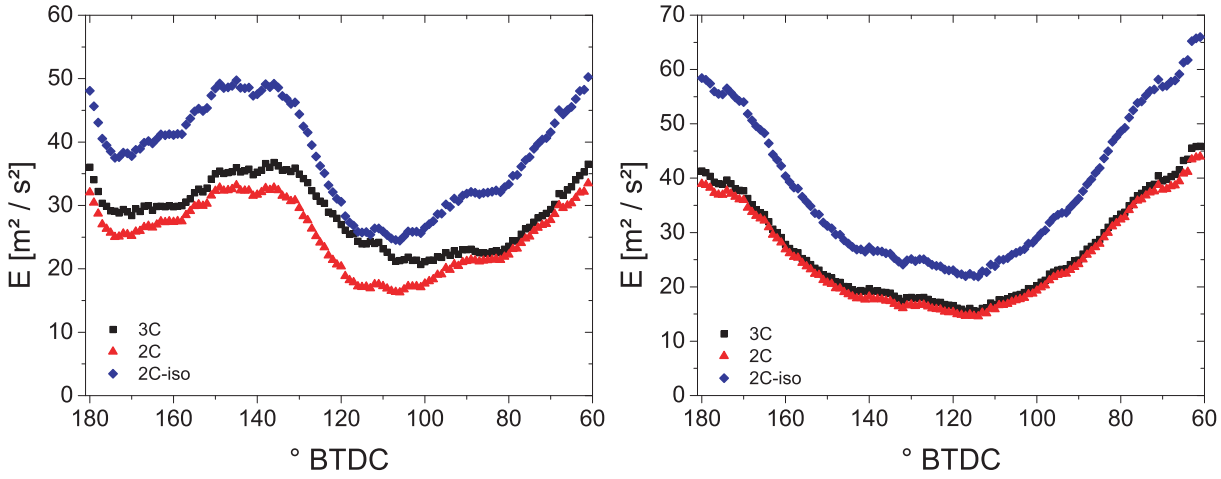

Figure 4.7: Comparison of spatially-averaged kinetic energies E calculated with different methods for cycles 15 (left) and 72 (right). Engine speed: 1000 rpm, tumble charge motion.

The correlation between calculating the kinetic and turbulent kinetic energies with different methods is also true for the individual cycles 15 and 72. Figure 4.7 shows the distribution of kinetic energy for both. Albeit the out-of-plane velocity influences cycle 15 more (3C vs. 2C), cycle 72 shows little separation between 3C and 2C.

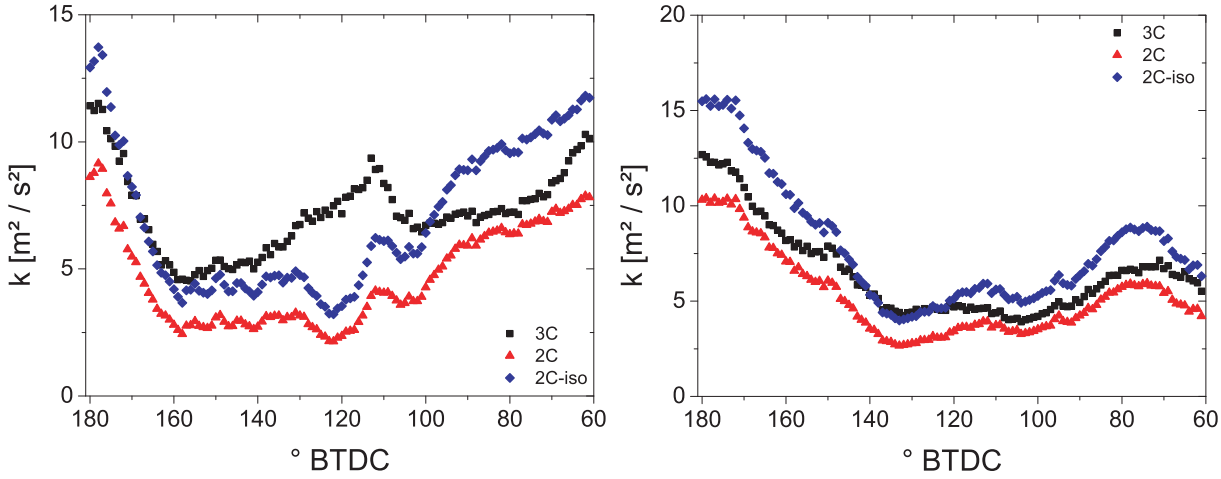

Figure 4.8: Comparison of spatially-averaged turbulent kinetic energies k calculated with different concepts for cycles 15 (left) and 72 (right). Engine speed: 1000 rpm, tumble charge motion.

Corresponding to figure 4.7, the turbulent kinetic energies are shown in figure 4.8. Here, the isotropic orientation of the fluctuating velocities are underestimated in cycle 15. A relative good agreement is noticeable in cycle 72.

Cycle-to-cycle fluctuations of vortex development

By determining the location of the vortex center, the cycle-to-cycle variations are readily identifiable. For this purpose, figure 4.9 presents the in-plane velocity vector fields of the phase-averaged

recording (top row), cycle 15 (middle row) and cycle 72 (bottom row) at 80°and 75° BTDC. Highlighted in blue are the streamlines of the flow motion starting only from the bottom array of vectors.

In the velocity vector field of the phase-averaged data, the vortex center is identified by the continuous smaller spacing of the streamlines. The diagonal trajectory towards the inlet valves (upper left) is also noticeable.

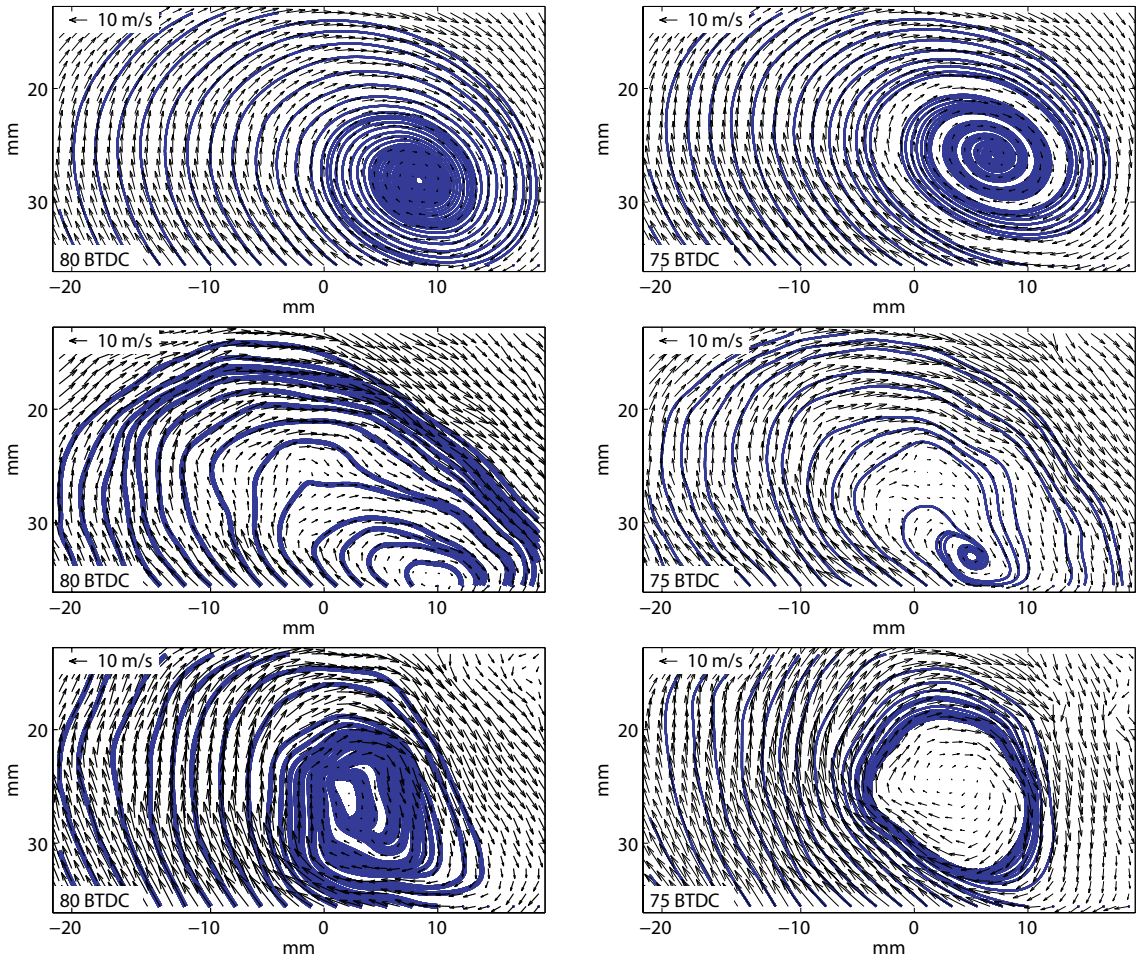

Figure 4.9: Comparison of phase-averaged velocity vector field with cycles 15 (middle) and 72 (bottom) including streamlines.

Cycle 15 and 72 display a very different behavior not only in the spatial location of the center, but also in temporal evolution. At 80° BTDC, the location of the vortex center in cycle 15 is estimated at x = 12, y = 37 mm. Concurrently, the center of cycle 72 is at x = 5, y = 26 mm. Five crank angles later, the center of cycle 15 has moved horizontally towards x = 5, y = 35 mm, while the center of cycle 72 has moved to x = 3, y = 24 mm. At this point, the streamlines only border to the vortex core of cycle 72. This indicates a more uniform, self-contained vortex core.

The spatial resolution of the streamlines and their significance is greatly determined by the resolution of the recorded data (spatial resolution of the PIV was 1 x 1 mm per vector), as well as by the field of view.

The temporal evolution of the vortex center path from 80° to 62° BTDC of the discussed cycles is shown in figure 4.10. In black, the path of the vortex core identified in the phase-averaged data is

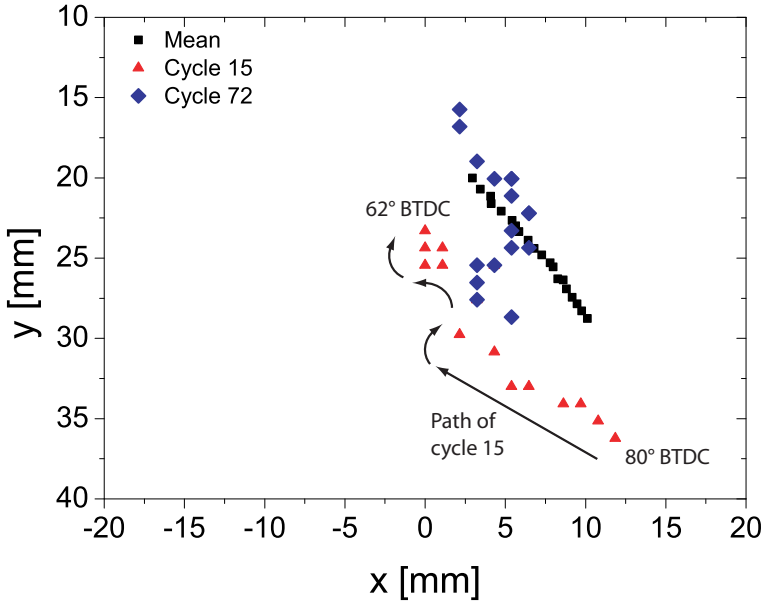

Figure 4.10: Vortex center path of the flow field (phase-averaged, cycles 15 and 72) at 1000 rpm with a tumble charge motion.

presented. The vortex center locations of the cycle 15 and 72 are also plotted. Both clearly show cycle-to-cycle variations (ccv).

Swirl charge motion

The swirl charge motion is generated by blocking one the dual manifold intake channels as described in section 2.1. This preconditioning of the inflow enforces a large scale flow rotation with the rotational axis close to the cylinder axis. The consequent strong out-of-plane velocities are confirmed by the phase-averaged data shown in figure 4.12, left column. A superimposed tumble flow motion generated by the asymmetric inflow and the cylinder head however tilts the axis relatively to the cylinder axis diagonally in the field of view. The results are strong out-of-plane velocities in opposing corners throughout the recording range.

Compared to the velocity magnitudes of the tumble charge motion, the in-plane velocities of the corresponding crank angles are significantly reduced. The out-of-plane velocities dominate the flow field. Viewing the flow motion from the piston (compare experimental setup, figure 3.2), the swirl charge motion rotates clockwise.

In comparison to the phase-averaged data, the explicitly chosen cycles 12 (middle column) and 83 (right column) are used to emphasize the occurrence of cycle-to-cycle variations. More small-scale flow patterns are shown at early crank angles by the in-plane velocity components, as an overall structured tumble formation is not observed. However, the primary flow structure dominated by the out-of-plane component, is present similar to the phase-averaged data.

Along the same statistical evaluation of the velocity fields like with the tumble charge motion, the kinetic energy E and turbulent kinetic energy k distribution are shown in figure 4.11. The spatially-averaged kinetic and turbulent kinetic energies of the individual cycles are compared to the energies of the phase-averaged data.

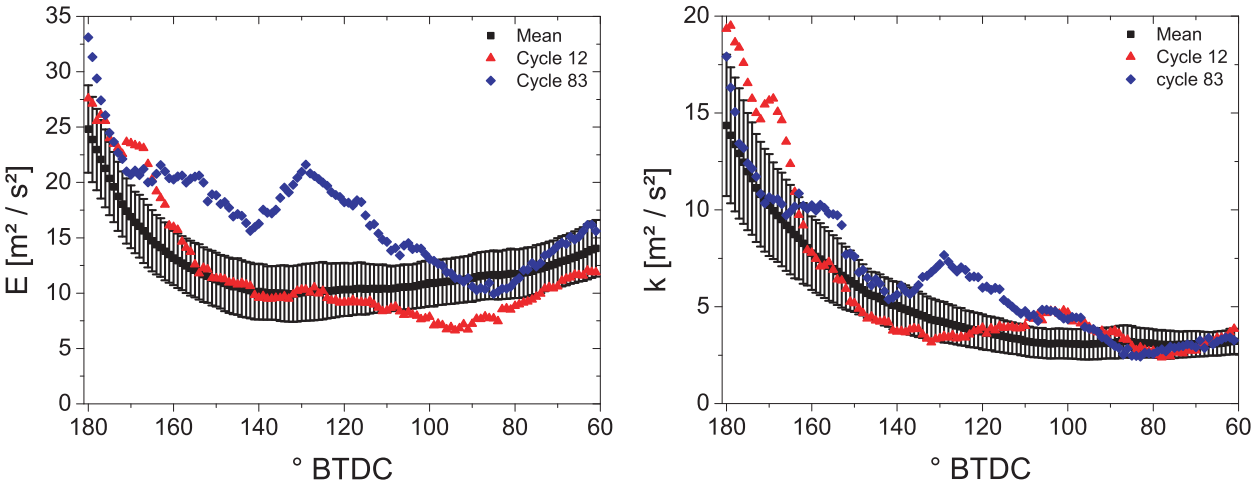

Figure 4.11: Left: Spatially-averaged kinetic energy E calculated from data recorded at an engine speed of 1000 rpm with a swirl charge motion. Phase-averaged data is presented in black (including 1-σ deviations), individual cycles 12 (red) and 83 (blue) are selected because of their significant deviations from the mean; right: corresponding turbulent kinetic energies.

Although the kinetic and turbulent kinetic energy progressions are sensitive to the considered FOV, a comparison between tumble and swirl charge motion is possible (identical FOV's). In general, the kinetic energies are lower than of the tumble charge motion, hence the lack of the structured flow field. However, a similar progression of the spatially-averaged, phase-averaged curve including an

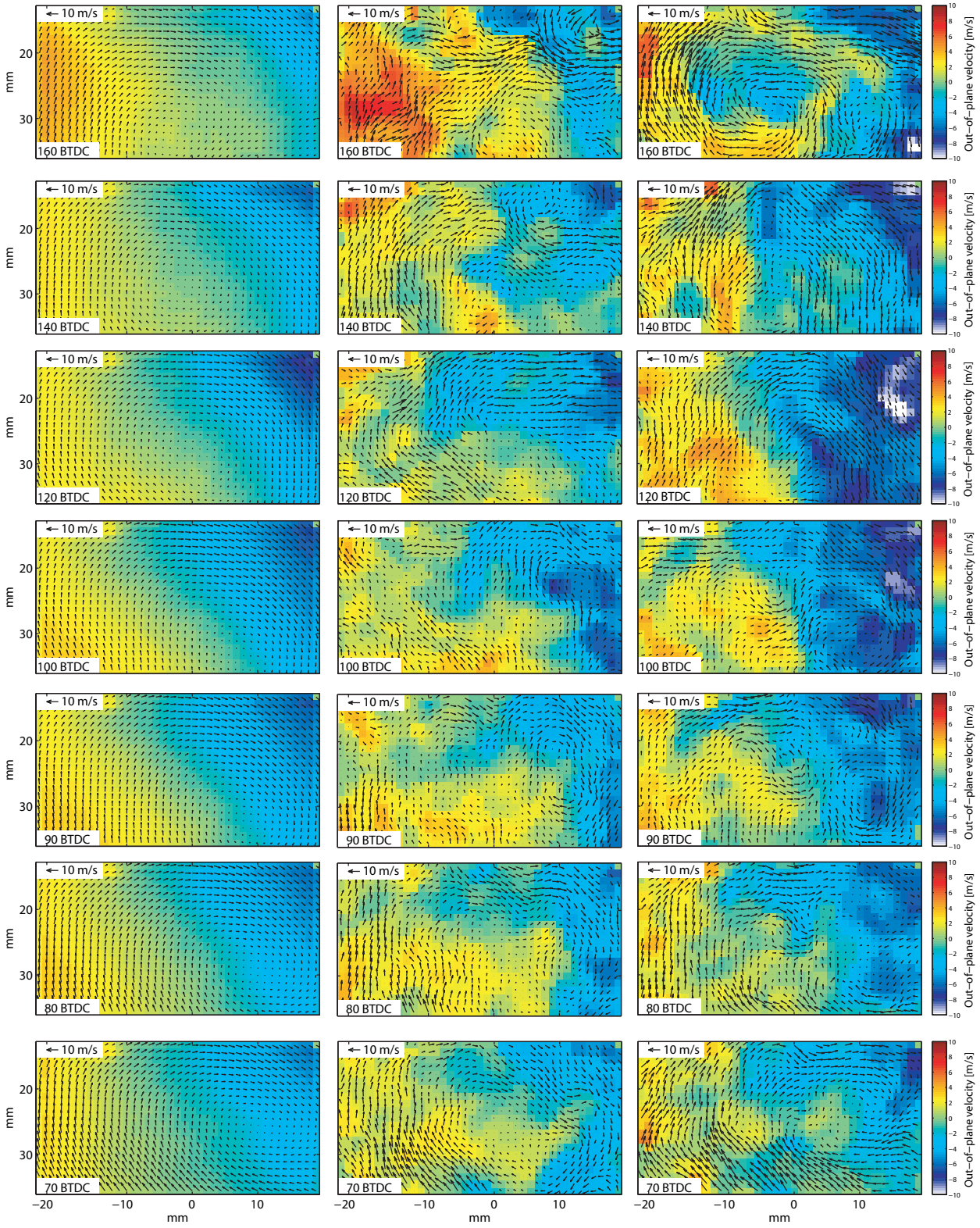

Figure 4.12: Example velocity vector fields at an engine speed of 1000 rpm with a swirl charge motion. Left: phase-average flow fields, middle: instantaneous velocity vector fields of cycle 12, right: cycle 83.

increase towards TDC is noticeable. Despite the lower kinetic energies, the fluctuations show a similar level of intensity.

The individual cycles 12 and 83 exhibit above / below average kinetic energies. Both can be used to visualize the intensity of the cycle-to-cycle variations.

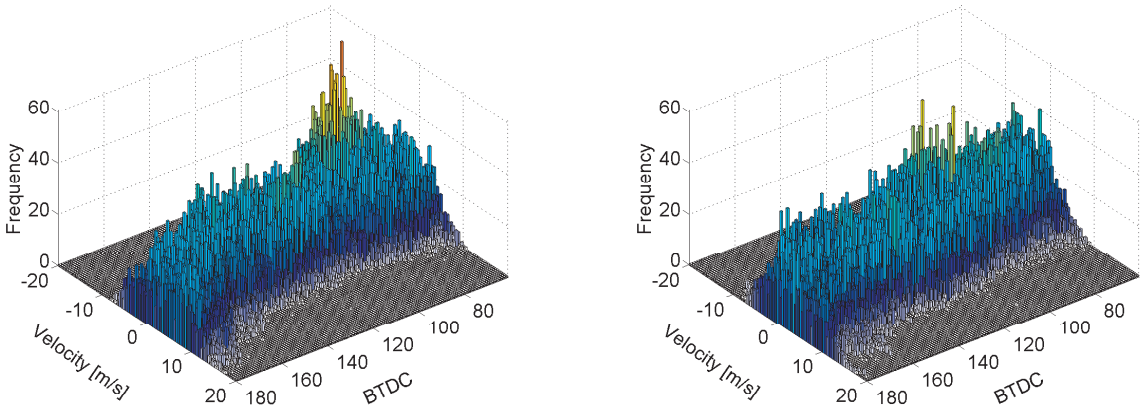

Figure 4.13: Histogram of the absolute velocity distribution of cycles 12 (left) and 83 (right).

In figure 4.13, the absolute velocity distribution of cycles 12 and 83 is shown. In comparison to the velocity distributions with a tumble charge motion, the velocity values tend to be lower to $\sim$0 - 2.5 $^{m}/_{s}$. In comparison to each other, cycle 12 presents a broader distribution at the end of the recording range. Cycle 83 variates only little around 0 $^{m}/_{s}$.

Analysis of the influence of u_z

As the influence of the out-of-plane velocity component is much higher with a swirl charge motion (compared to a tumble charge motion), the effect of neglecting u_z results in significantly lower spatially-averaged kinetic energies. This fact is shown for the kinetic energy (left) and the turbulent kinetic energy (right) in figure 4.14 (same notation as in the tumble charge motion section).

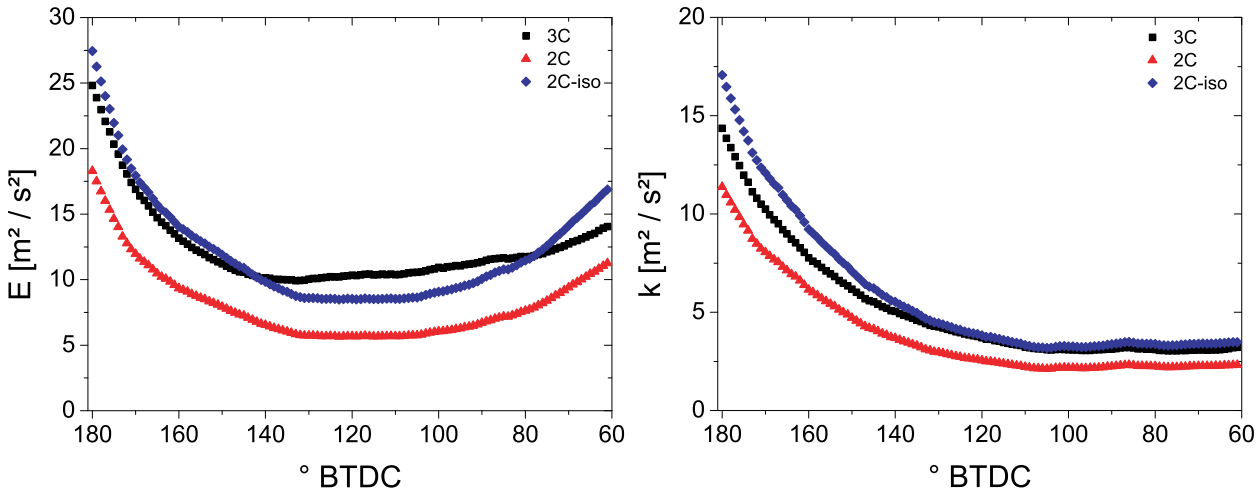

Figure 4.14: Comparison of spatially, phase-averaged kinetic energies E and k calculated with different methods. Engine speed: 1000 rpm, swirl charge motion.

The kinetic energy calculated with all three velocity components compares closely to the distribution calculated by substituting u_z equally with u_x and u_y (3C vs. 2C-iso). Using only the in-plane velocity components underestimates the level of kinetic energy completely. However, at late crank angles, the levels of kinetic energy calculated with only the in-plane velocities and all three velocity components decreases (2C vs. 3C), thus the influence of the out-of-plane component decreases.

The turbulence field (characterized by the fluctuating velocities) behaves similarly as with the tumble charge motion. The orientation of the small scale structures is close to isotropic.

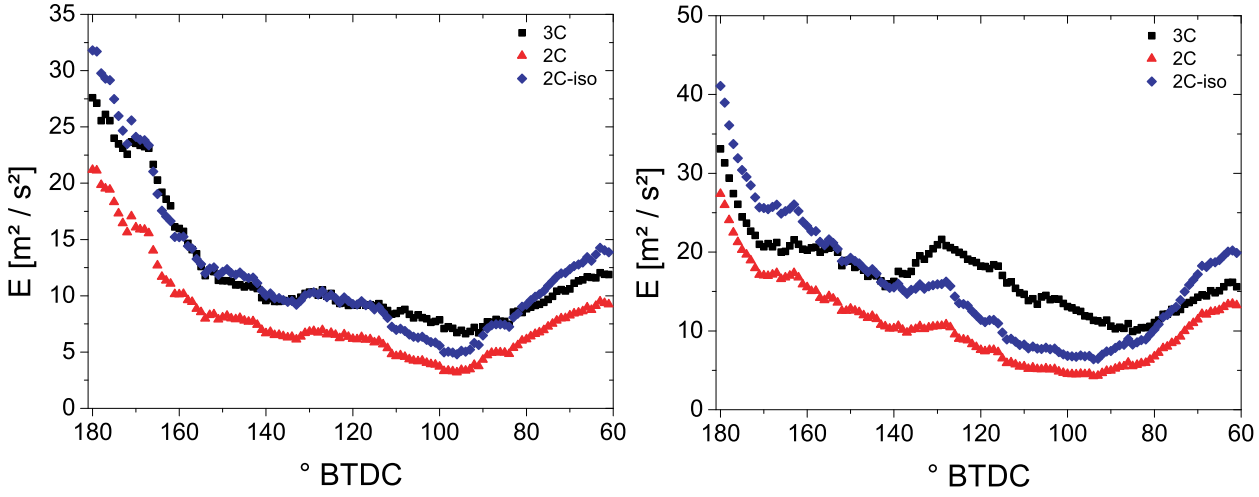

Figure 4.15: Kinetic energy E of cycle 12 (left) and 83 (right).

In figure 4.15, the kinetic energy distribution of the individual cycles is shown. Similar to the phase-averaged data in figure 4.14, the level of kinetic energy calculated with all three velocity components is in agreement with the calculation substituting u_z (3C vs. 2C-iso). Cycle 83, however, shows a crank angle range, 140° - 80° BTDC, in which even the substitution does not attribute the intensity levels. In this region, the out-of-plane component has a significant influence.

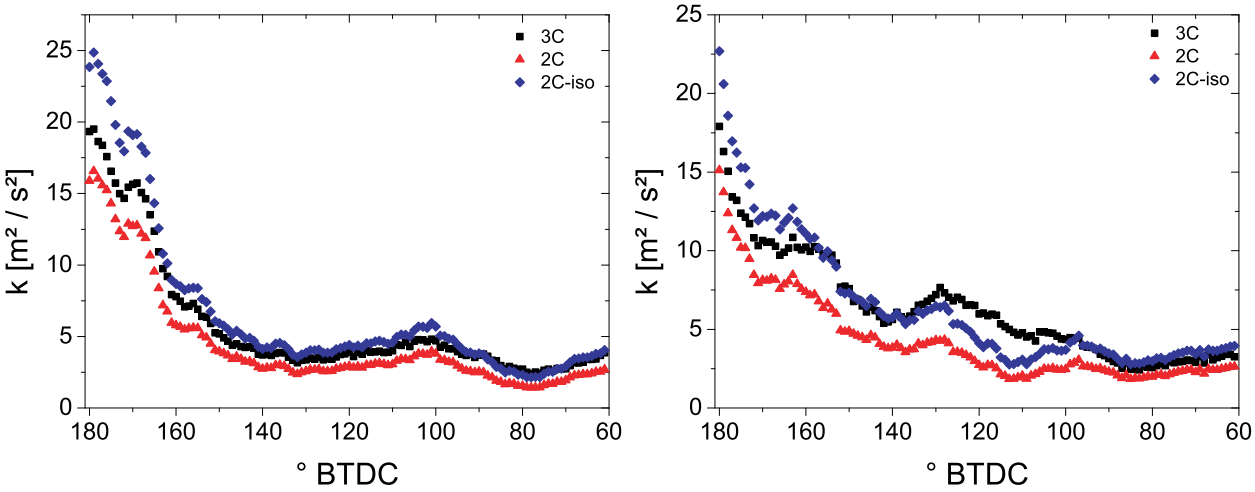

Figure 4.16: Turbulent kinetic energy k of cycle 12 (left) and 83 (right).

Analogously to figure 4.15, figure 4.16 presents the turbulent kinetic energy k of the single cycles. Both show the expected progression, as the isotropic orientation of the fluctuating velocity vectors dominates.

Notice, the above presented results are only valid within the field of view and the considered in-cylinder geometry. For a general assertion of the kinetic energy distributions, the whole flow motion has to be analyzed, e.g. with multiple measurement planes or ideally with a volumetric measuring technique.

Neutral charge motion

The neutral charge motion marks a non-conditioned manifold inlet flow, hence both manifold inlet pipes have no insertions and only the geometry of the cylinder head and valve openings influence the flow structure. In figure 4.18, the phase-averaged flow field (left column) as well as two explicit individual cycles (middle: cycle 24; right: cycle 86) are shown.

No distinctive flow structures are identifiable. The out-of-plane velocity components are near zero for the phase-averaged data. Additionally, as expected, the velocity magnitude is lower than for the guided intake flows.

In figure 4.17, the corresponding kinetic (left) and turbulent kinetic energy (right) are presented. In black, the spatially-averaged, phase-averaged energies including their respective error bars (1-σ deviation) are shown. Similar to the above sections, the two explicit cycles 24 and 86 were chosen because for their above / below average energy distribution. Noticeable is the steep increase in kinetic energy for cycle 24, as the directed flow structures also appear in figure 4.18 at the corresponding crank angles.

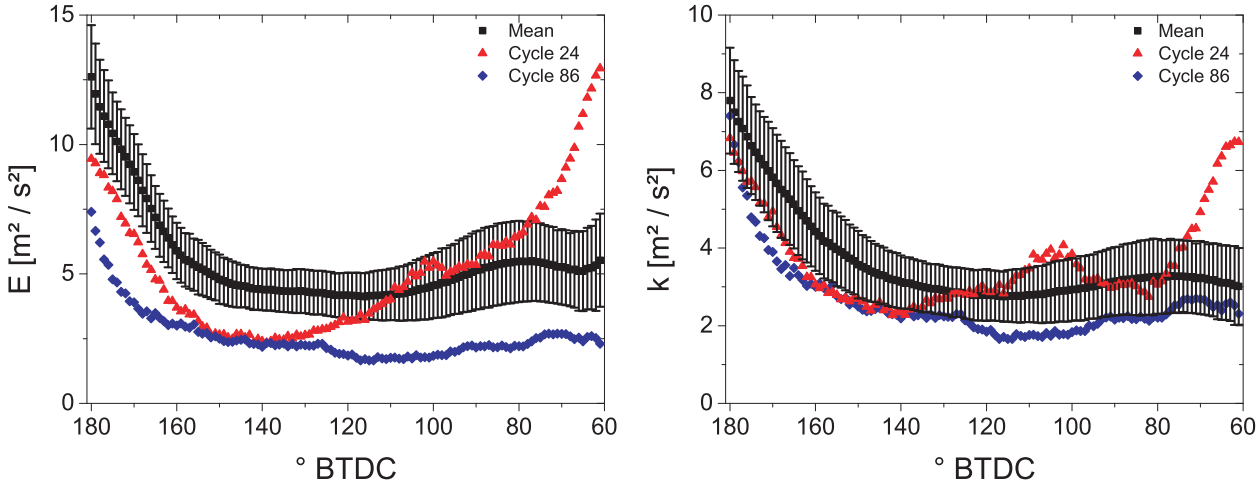

Figure 4.17: Kinetic energy E and turbulent kinetic energy k at 1000 rpm with a neutral charge motion.

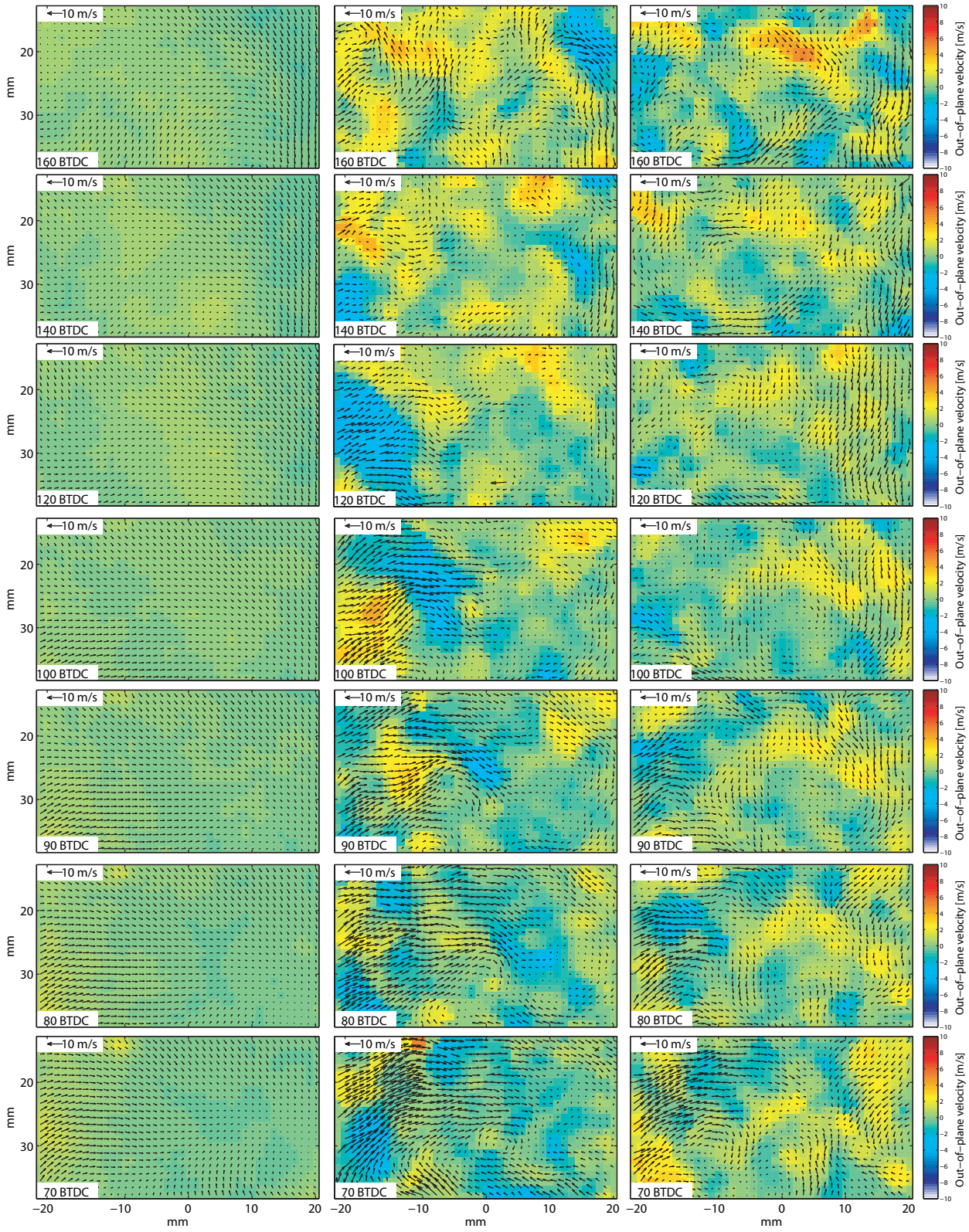

Figure 4.18: Example velocity vector fields at an engine speed of 1000 rpm with a neutral charge motion. Left: phase-average flow field, middle: instantaneous velocity vector fields of cycle 24, right: cycle 86.

Comparison of charge motion influences

For a more clear comparison, the spatially, phase-averaged kinetic and turbulent kinetic energies for each charge motion are shown in figure 4.19.

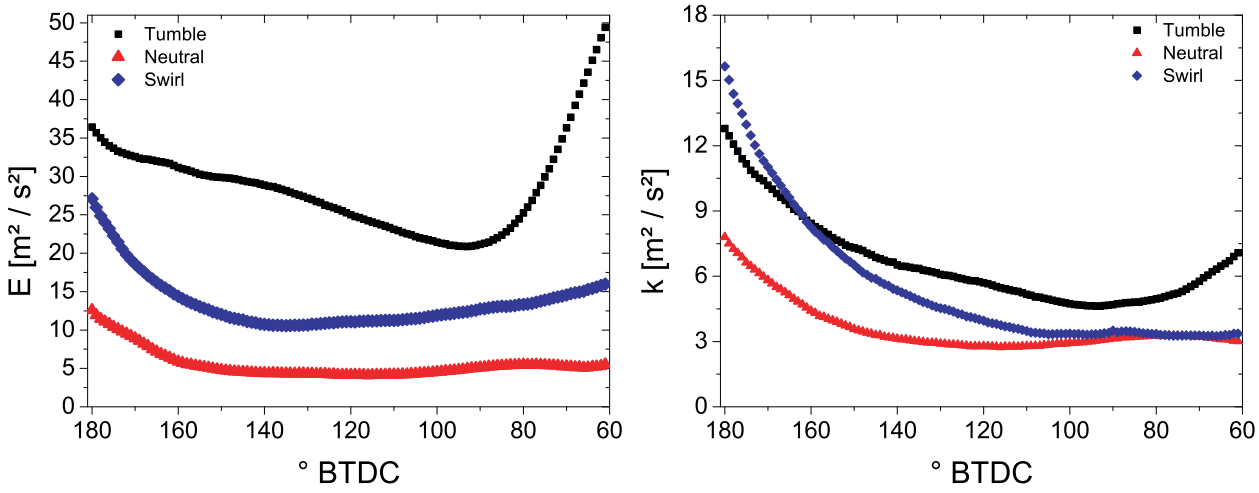

Figure 4.19: Comparison of spatially-averaged, phase-averaged kinetic and turbulent kinetic energies of different charge motions at 1000 rpm.

As clearly noticeable, the directed flow structure of the tumble charge motion exhibits the highest level of kinetic energy. The influence of the out-of-plane component during the swirl charge motion also contributes to a higher level of kinetic energy compared to the neutral charge motion. However, the fluctuations shown by the turbulent kinetic energy of both are comparable at late crank angles. Only the tumble charge motion shows higher fluctuations, which are attributed to the formation of the tumble vortex which has been shown to be highly dependent on the form of the cycle-to-cycle variations.

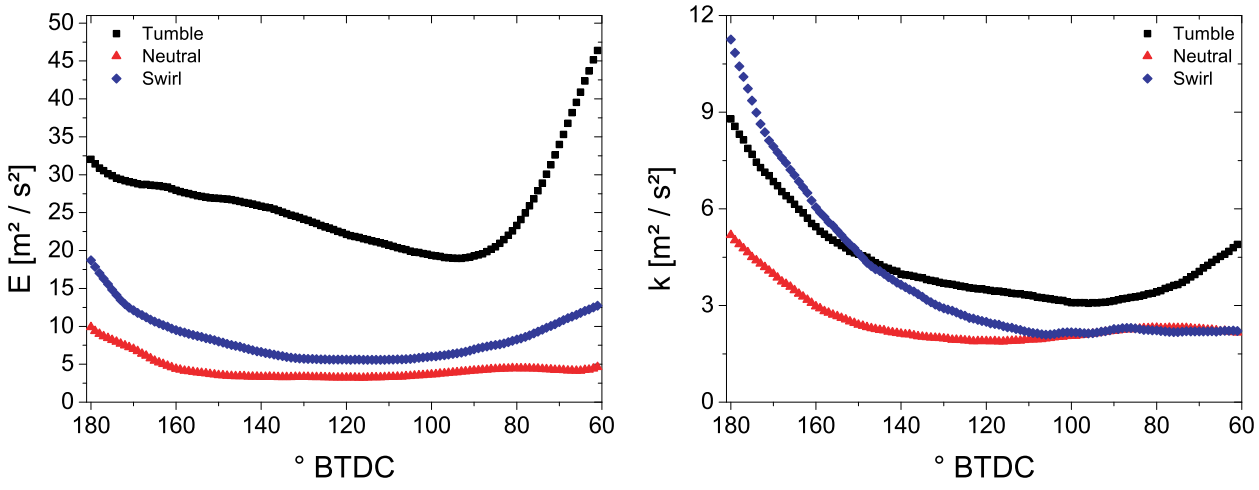

Figure 4.20: Comparison of kinetic energy E and k at 1000 rpm with a different charge motions using only the in-plane velocity components.

Similar to the data shown by Müller [14] and Gleißner [67], the spatially-averaged, phase-averaged kinetic energy and turbulent kinetic energy for each charge motion is plotted in figure 4.20, using

only the in-plane velocity components. As mentioned in the distinctive sections, the in-plane velocity components dominate the tumble and neutral charge motion. The swirl charge motion however is dominated by the out-of-plane velocity u_z, as the offset displays. Additionally, the fluctuations are underestimated for each charge motion when using in-plane components only.

4.1.3 Analysis of engine speed

The spatially-averaged, phase-averaged kinetic energies of different engine speeds with a tumble charge motion are shown in figure 4.21.

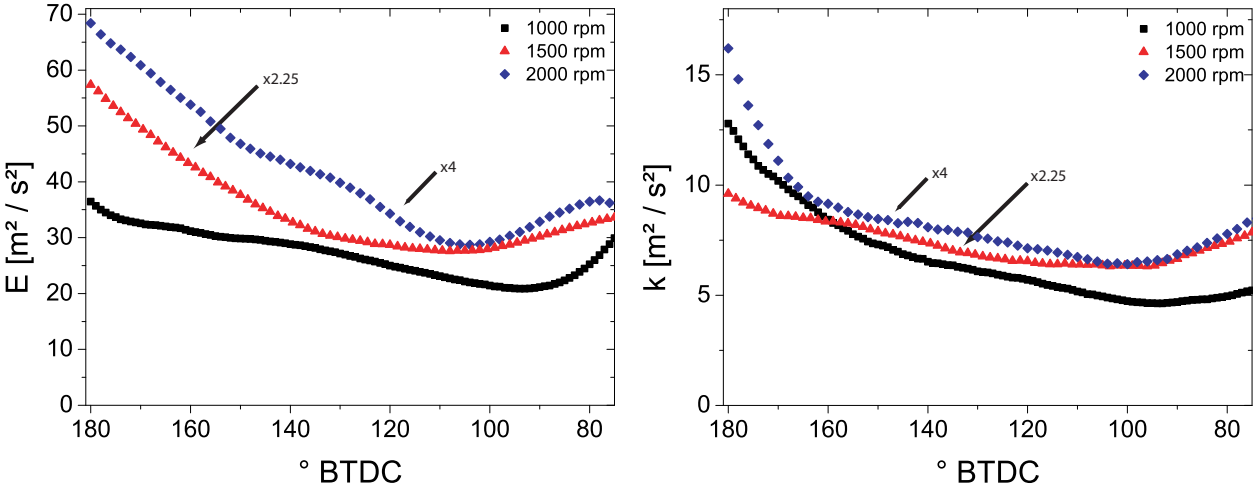

Figure 4.21: Comparison of spatially-average, phase-averaged kinetic and turbulent kinetic energies at different engine speeds with a tumble charge motion normalized to the reference engine speed of 1000 rpm.

To compare the phase-averaged kinetic energies, the values at higher engine speeds were normalized by the quadratic ratio to the reference engine speed of 1000 rpm, resulting in a factor of 2.25 for 1500 rpm and a factor of 4 for 2000 rpm. The reason for this is the assumption of a linear correlation between the in-cylinder flow velocity and the engine speed. As the kinetic energy is proportionate to the velocity squared, so is the engine speed squared proportional to the kinetic energy. This is the same as normalizing to the mean piston speed, which is only a multiplication with a constant factor.

The progression of the kinetic energy for all three engine speeds is similar. At ∼90° - 100° BTDC a minimum of kinetic energy is passed with a subsequent increase. The previous temporal gradient of the kinetic energy differs in magnitude. This is mainly due to the increased in-cylinder velocities produced by the faster revolving piston as well as the increased intake flow velocities due to the shorter valve timings.

On the right-side, the phase-averaged turbulent kinetic energies for each engine speed are plotted likewise. They show an analog distribution, as the engine speed also increases the fluctuations, hence the level of turbulent energy is also increased.

Following the previous arrangement, figure 4.22 shows the influence of the engine speed on the phase-averaged kinetic energies with a swirl charge motion.

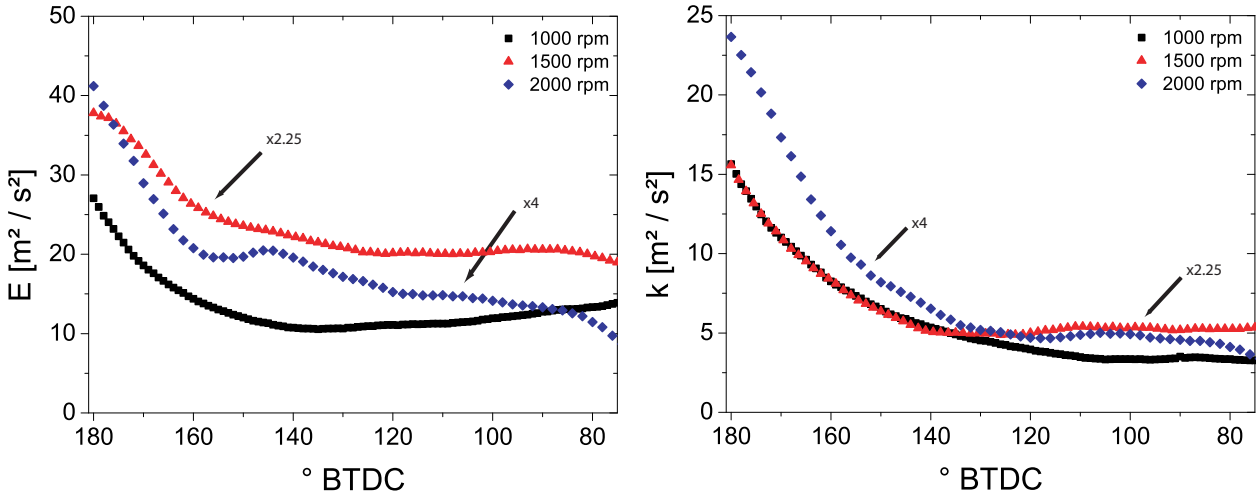

Figure 4.22: Comparison of spatially-averaged, phase-averaged kinetic and turbulent kinetic energies at different engine speeds with a swirl charge motion normalized to the reference engine speed of 1000 rpm.

Clearly visible is the decreased intensity of the phase-averaged kinetic energy at 2000 rpm as normalized values are below the values for 1500 rpm. Thus, in assumption the in-plane velocities remain equal, the higher engine speed influences the rotation speed of the swirl charge motion dominated by the out-of-plane velocity only little. This is only valid for the specific FOV and confirmation with multiple-plane or volumetric measurements is needed. The progression of the turbulent kinetic energy is similar for all three engine speeds.

Finally, the phase-average kinetic and turbulent kinetic energy distributions with a neutral charge motion are presented in figure 4.23.

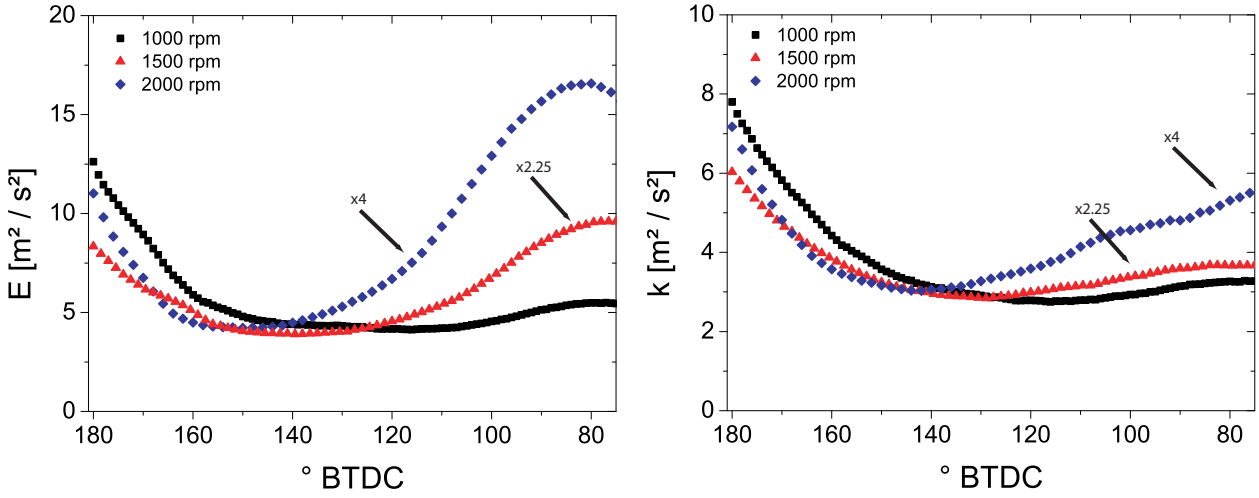

Figure 4.23: Comparison of spatially-averaged, phase-averaged kinetic and turbulent kinetic energies at different engine speeds with a neutral charge motion normalized to the reference engine speed of 1000 rpm.

A reverse behavior of the kinetic energy can be observed as a minimum occurs for each engine speed ∼150° BTDC. The subsequent increase in kinetic energy is prominently displayed with an

engine speed of 2000 rpm. The turbulent kinetic energy also displays this progression. However, in comparison to the other charge motions, the magnitude of the distributions are significantly reduced.

4.1.4 Conclusions

In this section the flow field structures were isolated from the rest of the engine cycle and viewed in detail. Using the method of stereoscopic PIV, the three dimensional velocity distribution over a FOV of 20 x 30 mm^2 was recorded. The temporal resolution of 6 kHz (i.e. one image per crank angle at 1000 rpm) enabled an in-depth investigation of the cycle-to-cycle variations as consecutive cycles were recorded.

Example phase-averaged as well as instantaneous velocity vector fields are shown for different charge motions (tumble, swirl, neutral) and engine speeds. The kinetic energy and turbulent kinetic energy are used as statistical tools to compare the individual recordings. The expected behavior that the large scale directed structures of the tumble charge motion comply to the highest kinetic energy levels is in agreement. However, the influence of the out-of-plane velocity component is underestimated with swirl charge motion, when only conventional two-component PIV is used. A second measuring plane rotated by 90°would be necessary to capture its influence, resulting in increased experimental complexity. Especially interesting is the substitution of the out-of-plane velocity component by superposition of the in-plane velocity. Here, the orientation of the fluctuating velocities show a more isotropic behavior. Additionally, the vortex center path was deduced from instantaneous recordings with the tumble charge motion. This enabled a clear identification of the cyclic variations as the large scale vortex structures forms.

4.2 Spray / flow field interaction dynamics

Overview

As presented in [117], one main focus of modern internal combustion engine development is the reduction of fuel consumption. Using the direct-injection method described in section 2.1.2, an intake independent fuel injection and thus a precise amount of fuel can be injected. Further, the injection timing can be freely set and enables late injection during the compression stroke at low- to mid-loads [118, 35]. Hence, a stratified air / fuel mixture is produced. At the spark plug location and during spark timing the stratified air / fuel mixture needs to be within its flammability limits. Therefore, mutual interactions between in-cylinder flow field and spray cone need to be understood [118, 119]. The method of choice used in this section is conventional PIV while additionally capturing the subsequent Mie-scattering of the spray in a single cycle at high repetition rates.

As mentioned in section 4.1, the phase-averaged flow field of the transient compression stroke does not provide a comprehensive view because of cycle-to-cycle variations that are common in DISI engines [14, 10, 9]. These variations do not only affect the interaction of the flow fields and the spray, but also the orientation and expansion of the flame kernel as shown in section 4.4. Therefore, the following investigation was also recorded at 6 kHz using a single CMOS camera. The recording range from $\sim$90° - $\sim$50° BTDC included the flow field prior to injection and the subsequent spray injection (more details about the setup are presented in section 3.4).

The measurements were performed in motored operation mode. The characterization of the flow field and its cycle-to-cycle variations are presented using sample images. A more quantitative view is discussed by the use of the kinetic energy of the flow field. With this method, the flow fields of different engine operation modes are compared. The second aspect addressed is two-component PIV and subsequent spray Mie-scattering measurements studying the influence of the in-cylinder flow upon the spray cone development. These studies are performed at different charge motions and three different injector types.

4.2.1 Influence of the charge motion

The focus of this study was on stratified fuel injection conditions. Therefore, only late injection timings within the compression stroke were investigated. An arbitrary cycle of a typical measurement is shown in figure 4.24.

The quality of the vector fields was comparable to previous studies using two-dimensional, high-speed PIV [14, 15]. In general, a temporal resolution of $166.\bar{6}\,\mu$s (6 kHz) was sufficient to reasonably resolve the temporal dynamics of the in-cylinder processes. An engine speed of 1000 rpm and tumble charge motion served as a reference case. The recordings of the flow field spanned from 90° BTDC until start of injection at $\sim$54° BTDC, followed by tracking spray dynamics for another 5° CA. For all experiments the end of injection timing for the spray was set to 50° BTDC. The injection time was dependent on the injector type. For an injection pressure of 10 MPa the following injection times were used: multi-hole injector: 750 μs; swirl injector: 1120 μs; annular orifice injector: 568 μs. Thus, the amount of injected fuel was constant.

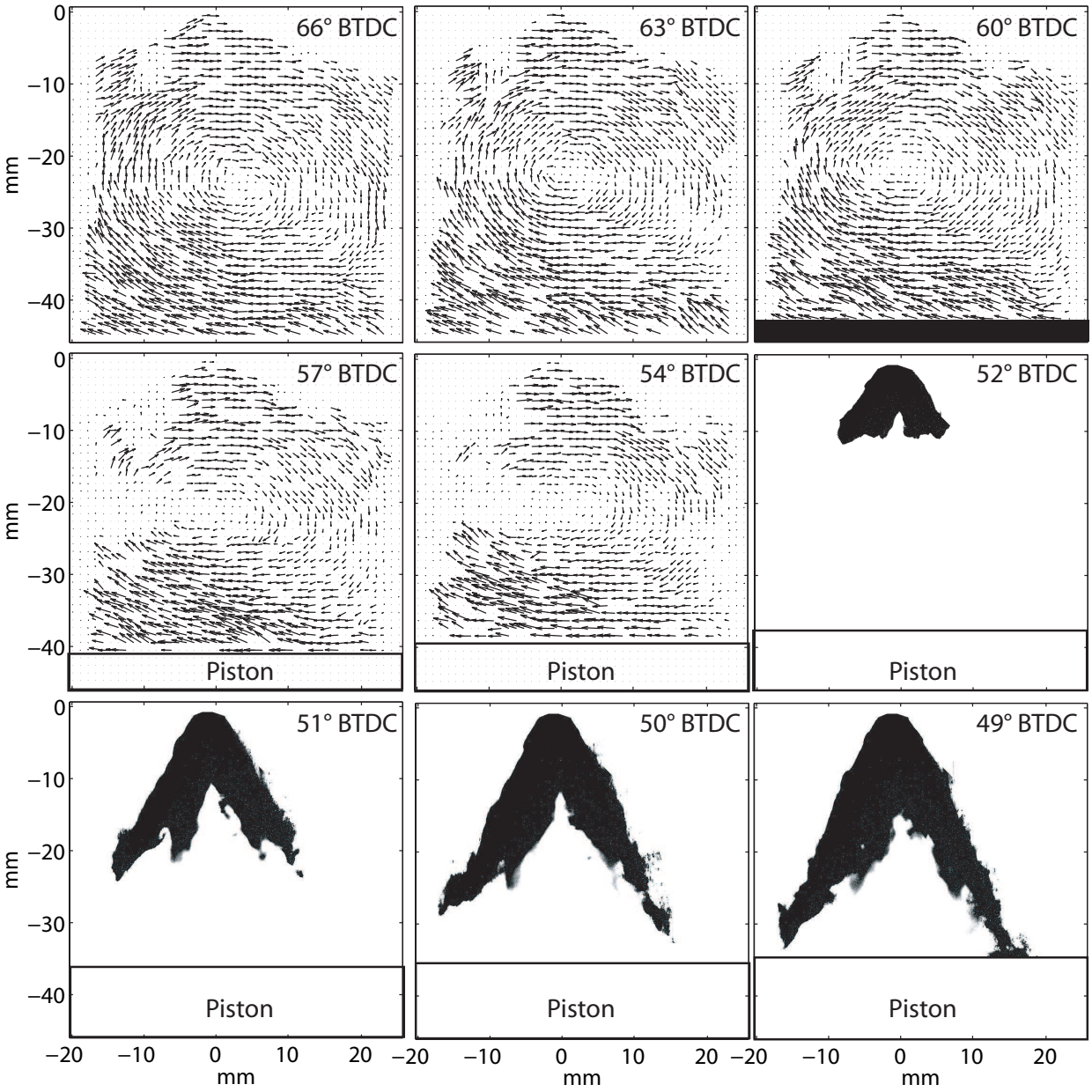

Figure 4.24: Example flow field / spray injection sequence. Engine parameters: 1000 rpm, tumble charge motion, multi-hole injector, injection pressure 10 MPa, end of injection at 50° BTDC. The black rectangle represents the piston.

The vector field presented in figure 4.24 shows a strong vortex center that moves diagonally towards the upper left of the field of view. This large scale flow structure dominates and small structures are barely visible. The horizontal cut-off observable in the lower part of images starting at 60° BTDC is due to the upward moving piston. Fuel spray is observed starting at 52° BTDC. At 49° BTDC the right hand side of the spray hits the piston surface causing wall-wetting.

The multi-hole injector (8 holes) features a symmetric geometry and symmetric spray patterns for undisturbed conditions. During in-cylinder operation, however, the cones observed in the field of view are increasingly asymmetric. At early stages (52° BDTC), the spray expanded ∼10 mm

downstream and both "legs" appear symmetric. This indicates that the initial spray momentum dominates and in-cylinder flows are of minor impact. Only 2° CA later, at 50° BTDC, an asymmetric pattern has formed. The right hand side of the spray shows increased penetration depths and different geometric shapes. This observation is caused by the clockwise rotating tumble charge motion. For an improved understanding of these mutual interactions, the flow field prior to injection and the spray dynamics itself need to be characterized. Therefore, flow field features are statistically analyzed.

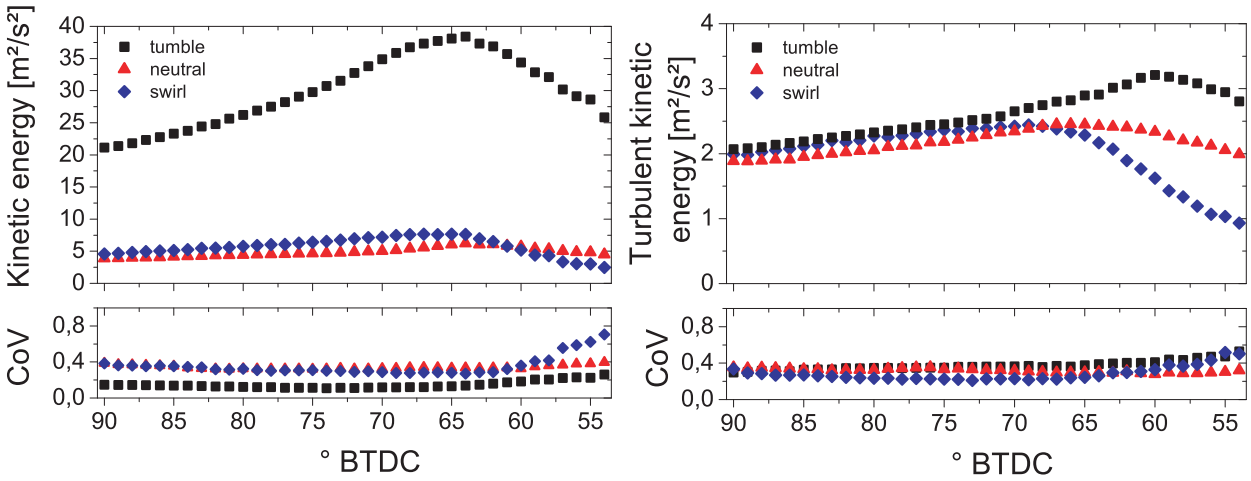

Figure 4.25: Ensemble-averaged, phase-averaged kinetic (left) and turbulent kinetic energy (right) of the flow field. Engine parameters: 1000 rpm, multi-hole injector, injection pressure 10 MPa, end of injection at 50° BTDC.

Kinetic (left) and turbulent kinetic energies (right) are shown in figure 4.25. The normalized variation of each measuring point is presented by the coefficient of variation (COV), which is defined as 1-σ deviation over absolute mean. For tumble charge motion, the charge accelerates during compression significantly. Correspondingly, the kinetic energy increases, passes through a maximum at 65° BTDC, and finally dissipation dominates. Contrary to swirl and neutral charge motions, the flow structures show a very different temporal evolution. More small scale structures are produced that are more easily dissipated as the piston revolves. Therefore, corresponding kinetic energies stay approximately flat up to ∼65° BTDC and then dissipate. The production of turbulent kinetic energy up to 70° BTDC is very similar for all cases and independent of the charge motion. At later stages, however, significant differences in the turbulence levels occur with highest turbulence levels for tumble and lowest turbulence levels for swirl motion. Assuming that small scale turbulent structures do not have a preferential direction and are isotropically distributed, the vertically orientated field of view is of secondary role. In this respect production of turbulence is clearly enhanced for the tumble charge motion within this engine (see section 4.1.2).

In comparison to the results presented in section 4.1, the kinetic energies distributions show a similar distribution (for their respective recording range) and are within the same magnitude. However, discrepancies cannot be avoided as two different PIV algorithms were used to calculate the velocity vectors.

Figure 4.26 presents the penetration depth (left) and spray drift (right) of the spray depending on the crank angle. Notice that the spray depth as defined in section 3.4 does not provide the longest extension of the spray but an average fuel spreading in vertical direction. Individual spray features

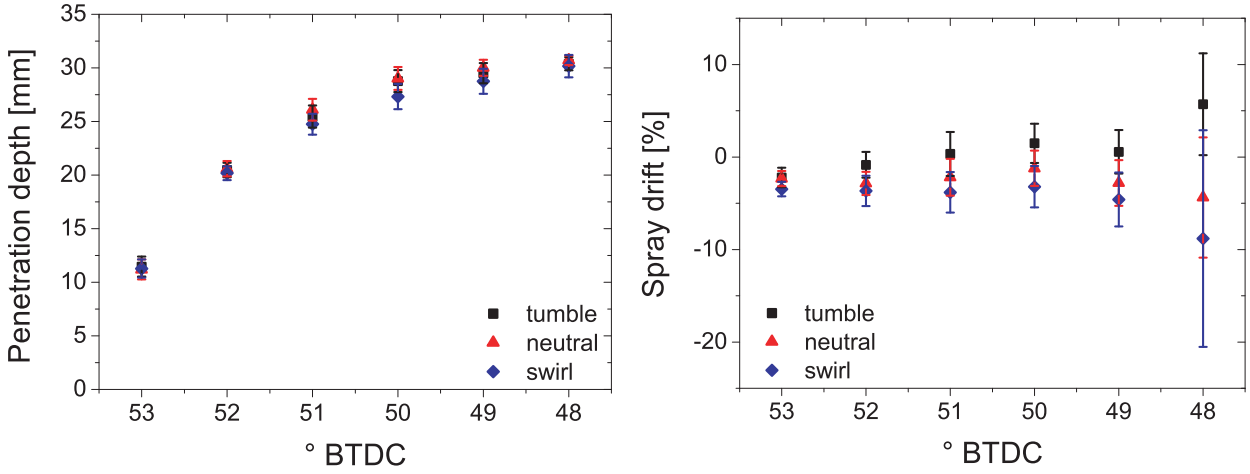

Figure 4.26: Penetration depth (left) and spray drift (right) of the spray injection at 1000 rpm, tumble charge motion, multi-hole injector, injection pressure 10 MPa, and an end of injection at 50° BTDC.

at the leading edge (such as elongated strains) may deviate from this definition of penetration depth and may already have moved further away from the injector. Considering this definition, the charge motion in general has no significant influence on the penetration depth. As can be seen in figure 4.26, left, the error bars representing the (1-σ) fluctuations of the multiple cycles indicate that the cyclic variations are rather small. A significant deceleration of droplets is observed for times after 51° BTDC. Shear stress and droplet evaporation promote decreasing droplet momentum.

The penetration depth according to the present definition does not provide a good measure for the impact of the in-cylinder flow that is visually apparent in figures 3.9 and 4.24. The asymmetry caused by the directed component of the in-cylinder flow is measured instead by the "spray drift" that already was defined in section 3.4. Looking at the tumble charge motion in figures 3.9 and 4.24, the spray cone at the right hand side is significantly extended. In consequence, positive values of the spray drift are observed as shown in figure 4.26, right. Switching from tumble to neutral or swirl charge motion, a very different observation is made. Up to 49° BTDC, corresponding sprays approximately keep their symmetry and subsequently are deformed to the left as indicated by negative values of the spray drift. The fluctuations (indicated by error bars) increase slightly, independent of the charge motion until 49° BTDC and then double during the following CA. Particularly for the swirl charge motion, fluctuations of the spray drift reach a maximum at 48° BTDC. A reason for this strong increase of fluctuation between 49°and 48° BTDC may be an increased impact of in-cylinder gas flow due to decreasing droplet momentum resulting in evaporation (reduced velocities and reduced droplet diameters), albeit further investigation is required.

4.2.2 Influences of the engine speed

By varying the engine speed, the kinetic energy of the in-cylinder flow is increased and an influence upon penetration depth and spray drift is observed. In figure 4.27, the kinetic (left) and turbulent kinetic energies (right) are compared for the tumble charge motion at 1000 and 1500 rpm, respectively. The end of injection was kept constant at 50° BTDC and the injection timing at 750 μs. Correspondingly, the start of injection shifts from 54.5° BTDC at 1000 rpm to 56.8° BTDC at

1500 rpm. Because the engine load for higher rpm was unchanged gas velocities and kinetic energies are increased correspondingly at 1500 rpm. A maximum is reached at 63° BTDC, a little earlier than at 1000 rpm. The subsequent dissipation, however, is more pronounced.

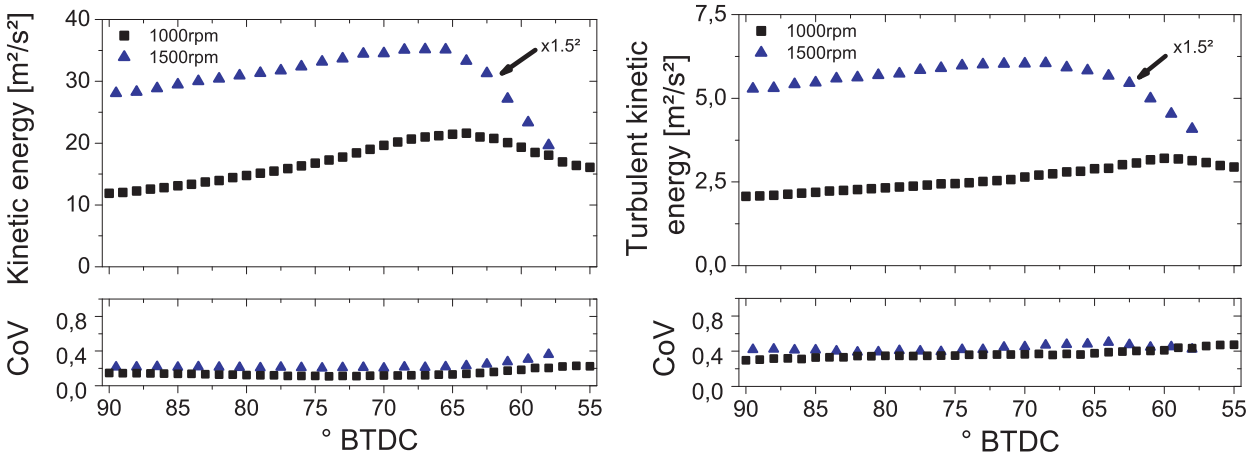

Figure 4.27: Ensemble-averaged, phase-averaged kinetic (left) and turbulent kinetic energy (right) distribution at 1000 rpm and 1500 rpm, tumble charge motion, multi-hole injector, injection pressure 10 MPa and an end of injection at 50° BTDC. The values of the kinetic energy at 1500 rpm are normalized by the square of the engine speed relative to 1000 rpm.

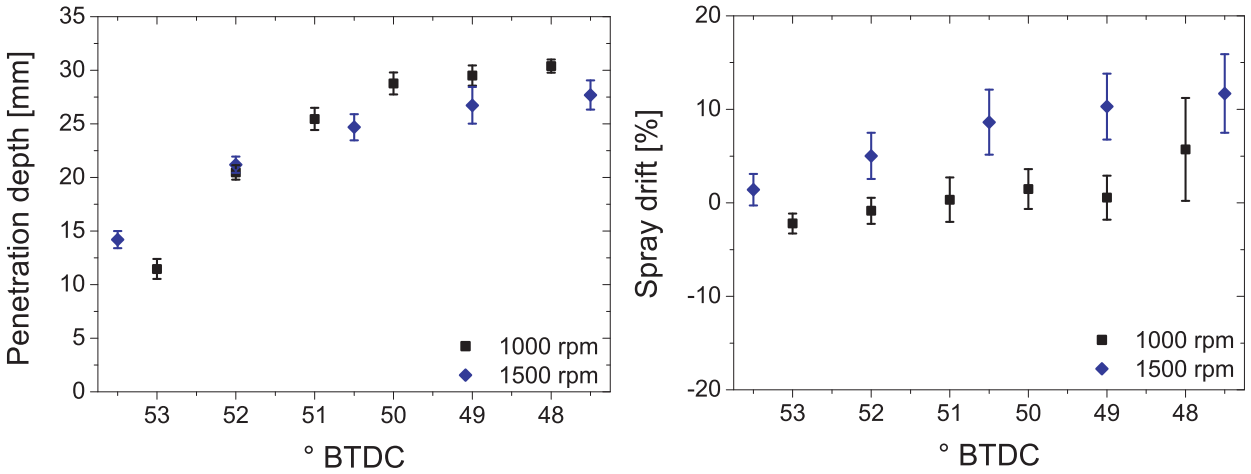

Figure 4.28: Penetration depth (left) and spray drift (right) at 1000 and 1500 rpm, tumble charge motion, multi-hole injector, injection pressure 10 MPa and an end of injection at 50° BTDC.

An increase in turbulence at higher engine speeds is similarly noticeable. The coefficient of variation at the bottom of figures 4.27, however, are only slightly increased for higher engine speeds. From this perspective, cyclic variations for fired conditions should remain unaffected. Penetration depths and spray drifts are presented in figure 4.28. At higher rpm start of injection is earlier. This causes a farther penetration up to 52° BTDC. The vertical displacement speed of the spray is lower at higher rpm (lower temporal gradients shown in figure 4.28, left for 1500 rpm). For engine times later than 52° BTDC, the penetration depth at 1500 rpm is therefore smaller compared to the 1000 rpm operation. In both cases, the injector pressure is kept constant at 10 MPa. The initial

momentum at the injector exit is therefore identical. Higher shear forces due to increased gas velocities lead to increased momentum transfer and decelerate the spray accordingly. For this reason, one similarly expects an increased spray drift. Figure 4.28 (right) exhibits this effect consistently. The spray asymmetry is enhanced significantly for higher engine speeds.

4.2.3 Variation of injector type / spray shape

In figure 4.29, sample sequences of the sprays are shown for a swirl (left), multi-hole (middle) and an annular orifice (right) injector. The engine is operated at 1000 rpm with a tumble charge motion. The injected fuel mass is identical, independent of the injector type. The injection pressure is 10 MPa. End of injection was at 50° BTDC, but injector opening duration was adapted for each injector according to the individual mass flow rates (multi-hole: 750 μs; swirl: 1120 μs; annular orifice: 568 μs).

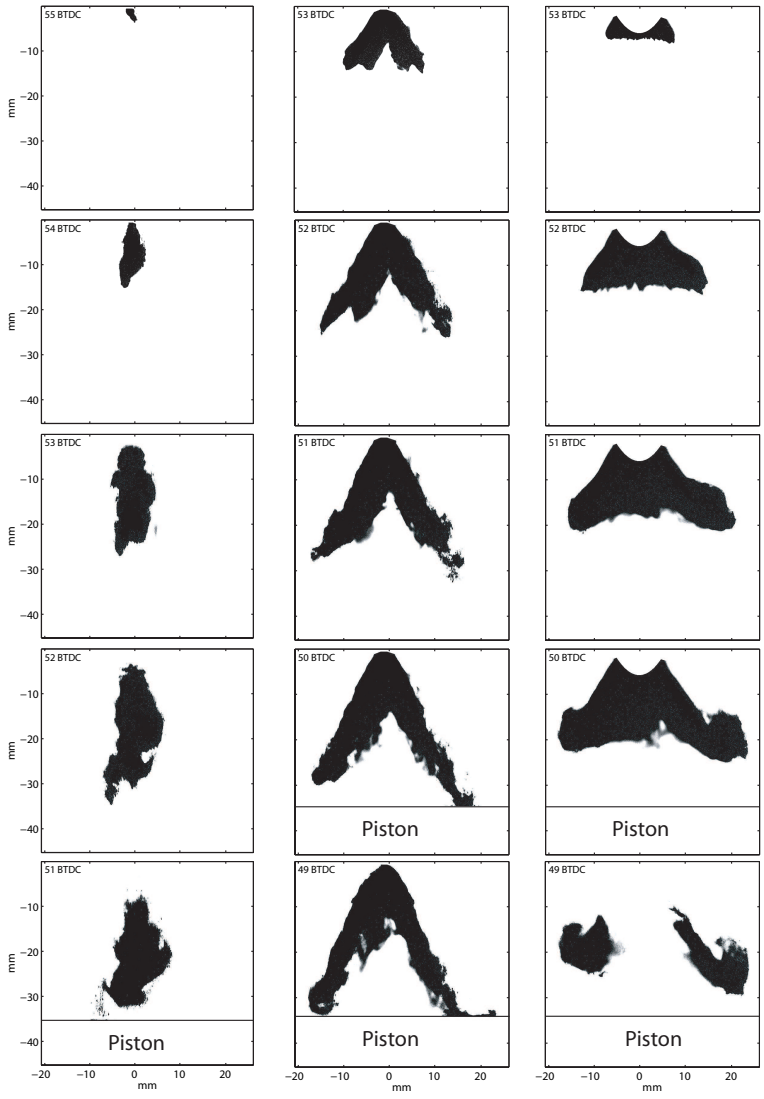

Figure 4.29: Overview of spray types. Left: swirl; middle: multi-hole; right: annular orifice.

Each injector type has its own characteristics with respect to fuel distribution and spray cone. As discussed in previous sections, within the field of view, the spray pattern of the multi-hole injector is characterized by two "legs". Initially both legs are fairly symmetric but an asymmetry develops as a result of the in-cylinder flow motion. The swirl injector on the other hand generates a very different spray pattern. The spray appears in the field of view earlier compared to the multi-hole injector because of an earlier start of injection (56.7° BTDC). Only a single cone develops which is fairly compact. Accordingly, spreading of fuel droplets into the entire volume is reduced significantly. The compact appearance is caused by regions of low pressure located inside the spray cone retarding spreading in radial direction. The spray cone collapses. Consequently, one expects comparatively fast displacement speeds in vertical direction (compare discussion of figure 4.26). The probability of the spray impinging onto the piston surface is enhanced. Wetting and in turn incomplete combustion accompanied by enhanced pollutant formation is expected.

The annular orifice injector generates a spray that enters the field of view earliest although start of injection is latest (53.4° BTDC). Unlike the other two injectors, the annular orifice injector is driven by a piezoelectric stack. Response times and inertia are minimized. Radial spreading of the spray is most pronounced but on the expense of fast vertical displacement speeds that are reduced significantly compared to the swirl injector. This lowers the probability of spray impact onto the piston surface. After end of injection around 50° BTDC, the spray patterns are still moving dynamically and the spray is clearly separated from the nozzle. Contrarily, the multi-hole injector exhibits more stagnant spray patterns where, particularly in the vicinity of the injector, spray dynamics are barely visible. Another specific feature of the spray patterns formed by the annular orifice injector is the formation of vortices. These vortices appear at 50° BTDC at the outer perimeter and are more pronounced at the right hand side indicating an asymmetric distribution of shear.

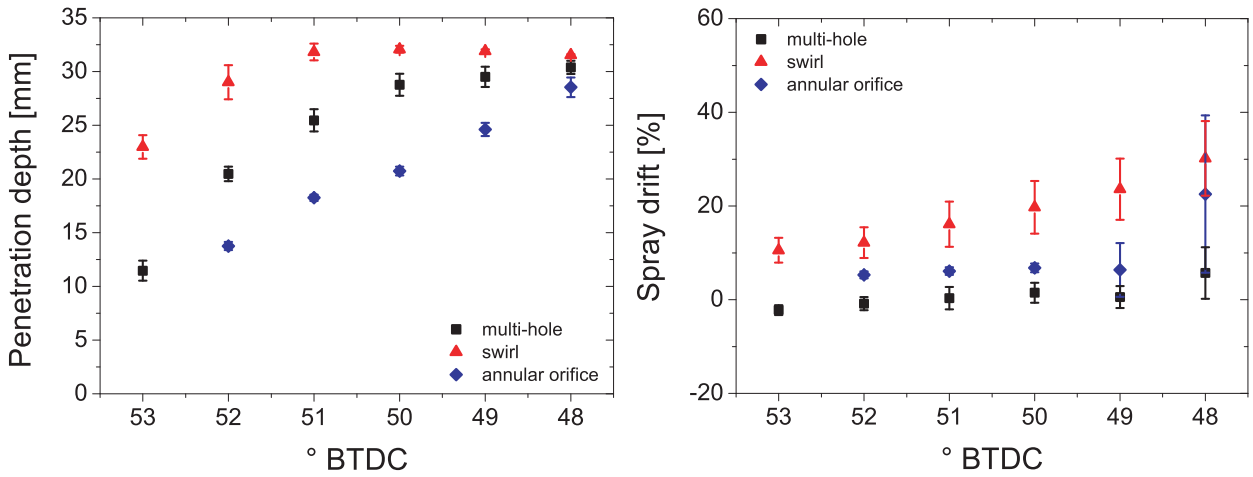

Figure 4.30: Penetration depth (left) and spray drift (right) for different injectors at 1000 rpm, tumble charge motion, injection pressure of 10 MPa and an end of injection at 50° BTDC.

Figure 4.30 compares the penetration depths (left) and spray drifts (right) of the three injector variants. The annular orifice injector shows a near linear expansion rate in the penetration depth. The build up and propagation of the annular spray pattern is not interrupted by the charge motion, although the spray drift exhibits significant asymmetries. The temporal evolution of the penetration depth of the multi-hole injector is faster during the initial phase but decelerates such that the penetration depth at 48° BTDC closely matches that of the annular orifice injector. In contrast, the swirl

injector shows the highest penetration depth at all times. At 51° BTDC, however, the penetration stagnates and the probability of piston wetting is most likely.

The spray drifts of the different sprays are compared on the right in figure 4.30. Relative to the multi-hole injector, spray drifts at 48° BTDC are increased up to a factor of 5 for the swirl and annular orifice injectors. In case of the annular orifice injector, this increase develops during only 2° CA. Accordingly, the impact of the in-cylinder flow is enhanced particularly at late stages of the spray penetration process. In terms of rapid air / fuel mixing, the annular orifice injector shows the highest potential.

4.2.4 Variation of injection pressure

Reducing the injection pressure has the general advantage of reducing the required electric energy for the fuel pump. In a parametric variation compared to the standard of 10 MPa, the injection pressure was thus set to 5 MPa. All other engine parameters were equal to the ones given in figures 4.29 and 4.30. The amount of fuel mass per injection was normalized to the injection timing of the multi-hole injector (750 μs). The annular orifice and multi-hole injector provide an approximately static flow rate even at 5 MPa ambient pressure. Hence, the injection time of the annular orifice was set to 778 μs. In contrast, the injection time for the swirl injector was increased to 1590 μs. Temporal evolutions of the penetration depth are shown figure 4.31. As remarked earlier, injection times for the swirl injector are significantly longer but without influence upon the maximum penetration. For the multi-hole and annular orifice injectors, the penetration depth shows a dynamic behavior independent of the surrounding pressure.

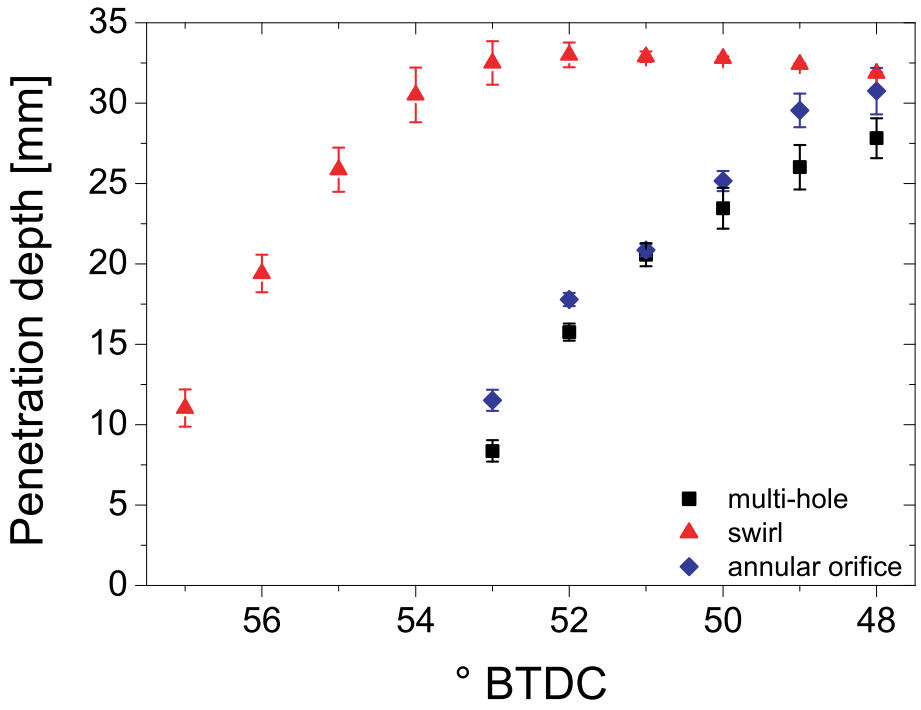

Figure 4.31: Penetration depth for different injectors at 1000 rpm, tumble charge motion, injection pressure of 5 MPa and an end of injection at 50° BTDC.

4.2.5 Conclusions

The interaction between in-cylinder flow field structures and the subsequent spray injection was investigated. The method to capture the instantaneous flow field as well as the spray injection was high-speed two-component PIV at 6 kHz. Single cycles of the flow field and the subsequent injection were recorded. Hence, a direct link between single cycle flow field structures and their influence onto the spray injection is feasible. The influences of different charge motions (tumble, neutral, and swirl), engine speeds, spray shapes, and injection pressures were analyzed in a parametric study.

Only the tumble charge motion with its dominant vortex flow structure (as analyzed in chapter 4.1) shows a strong influence onto the spray evolution, albeit only the drift of the spray is influenced. The momentum forces of the individual spray shapes are not affected as the penetration depth shows no indication. Especially at higher engine speeds than 1000 rpm, the drag forces of the flow field deform the spray shape. The solid-cone injection of the swirl injector is the most susceptible to influences by the flow fields.

Another important aspect of the flow field / spray interaction is the possibility of wall-wetting. Partial spray fractions accumulate on the cylinder wall or piston surface and increase emission of pollutants such as unburned hydrocarbons. Wall-wetting potentially occurs during late injection and can be influenced by in-cylinder flows. This is also detailed in the next section in which the fuel distribution is investigated.

4.3 Air / fuel distribution measurements

Overview

As shown in [2, 68, 120], the fuel distribution within the combustion chamber is especially important when using a direct-injection system. In contrast to section 4.2, in which the spray dynamics during a stratified fuel injection were investigated, this section analyzes the fuel distribution produced by injection during the early intake stroke. The main goal of this is a homogeneous mixture at high loads as this produces the maximum power output. The homogeneity of the mixture (level of molecular mixing between fuel and air) influences the concentrations of unburned hydrocarbons and is inversely linked to the emission of soot particles (the more uniform the mixture, the lower the emission of soot).

The analysis presents the spatial fuel distribution within the field of view. An indication of the equivalence ratio (inverse of air number) is shown, e.g. in figure 4.32. Finally, the dynamics between the flow field and the fuel distribution in form of wall-wetting are analyzed in a parametric study.

The homogeneity of the fuel distribution is investigated with planar laser-induced fluorescence (PLIF). Temporally resolved data of single cycles was recorded at 6 kHz as shown in chapter 3.5. The fluorescence signals of the reference fuel (no additional tracer added) were recorded with a CMOS camera connected to a high-speed multi-channel plate intensifier coupled with a booster. A Nd:YAG laser operating at 6 kHz with light emission at 532 nm was coupled with an externally boxed frequency doubling crystal (BBO) to produce the required radiation at 266 nm with a pulse energy of $\sim$0.5 mJ / pulse. The recording range of 50° - 10° BTDC focused on the conventional boundaries of ignition timing during the compression stroke.

4.3.1 Analysis of charge motion influences

Analysis with neutral charge motion

The flow structures investigated in section 4.1 have a strong influence on the fuel distribution within the combustion chamber. With a neutral charge motion the inflow through the valves produces more small scale flow structures as shown in chapter 4.1.2. No primary flow direction is dominant and fuel distribution least influenced by the in-cylinder charge motion. In figure 4.32, contour plots of the equivalence ratio are shown for a calibrated cycle with port-fuel injection (top row), phase-averaged data with direct-injection (second row) and single cycles with direct-injection (third and fourth row). The calibrated cycle (top row) is an arbitrary single cycle normalized to the phase-averaged data recorded with port-fuel injection (calibration process detailed in section 3.5). The local equivalence ratio distribution shows, within the measurement errors, a spatially homogeneous map. Small discrepancies occur on behalf of multiple errors e.g. increasing number densities, absorption, and self-absorption. The phase-averaged equivalence ratio distribution with a direct-injection of the fuel (second row) shows a stratification within the combustion chamber. A large portion of the field of view is dominated by a rich equivalence ratio throughout the recordings. Early, at 50° BTDC, the stratification is clearly visible as stoichiometric and lean portions are

located just above the piston crown. The rich areas left and right on top of the piston indicate wall-wetting (detailed in the next section).

Below the phase-averaged data with the direct-injection of fuel, figure 4.32 shows instantaneous fuel distributions of arbitrary cycles 71 (third row) and 91 (fourth row) of 100 recorded cycles. At 50° BTDC, both exhibit wall-wetting above the piston crown indicated by the rich mixture regions on the left.

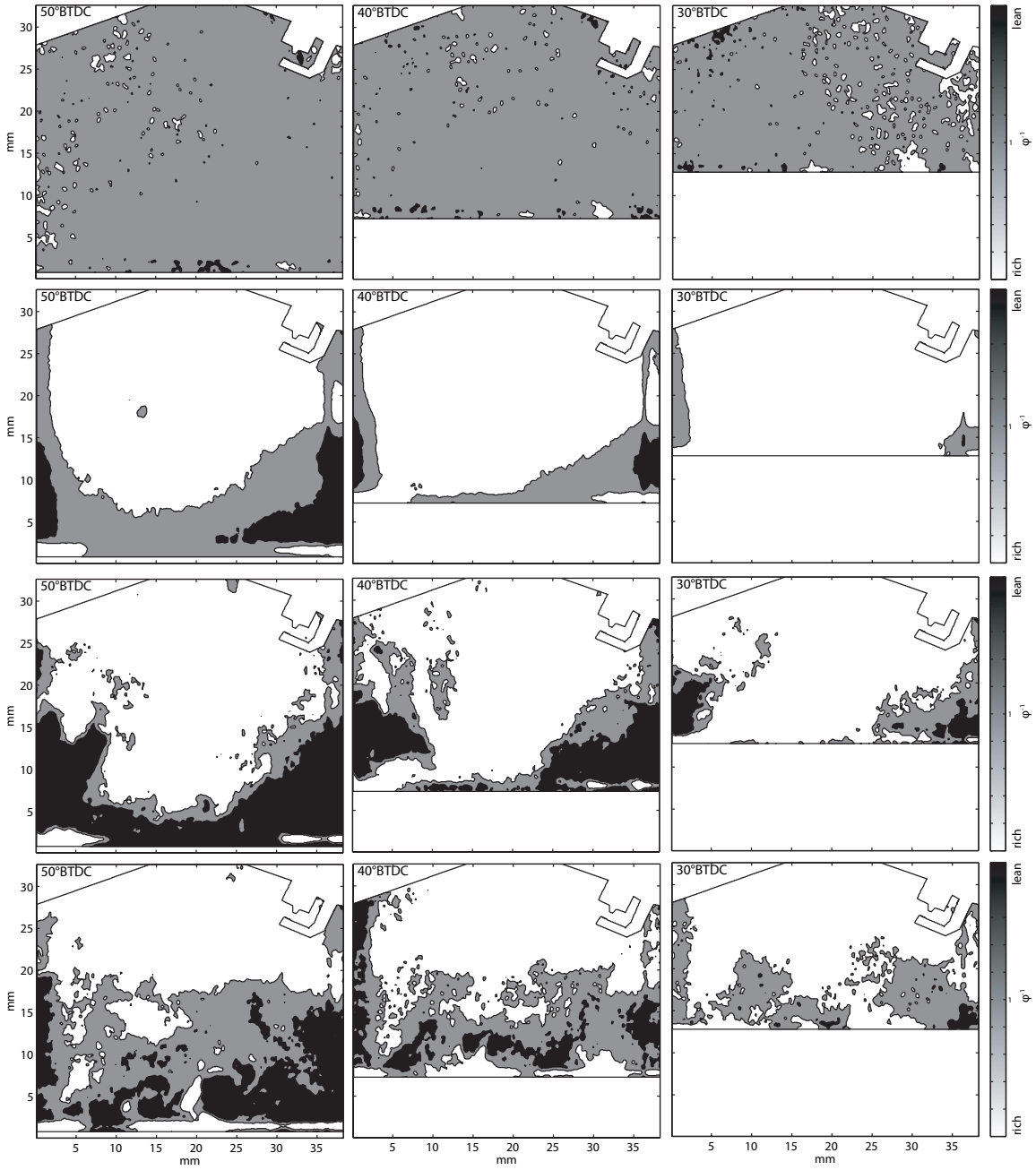

Figure 4.32: Contour plots of the air / fuel ratio distribution within the cylinder. First row: arbitrary calibrated cycle with port-fuel injection; second row: phase-averaged data with direct-injection; third row: cycle 71; fourth row: cycle 91 (both with direct-injection). Engine parameters: 1000 rpm, neutral charge motion, start of injection 300° BTDC.

Quantification of equivalence ratio

One aspect of the recordings was the quantification of the equivalence ratio inside the combustion chamber. In figure 4.33, left, the frequency distribution of the equivalence ratio from data recorded with a port-fuel injection at 1000 rpm with a neutral charge motion and an equivalence ratio of 1 is shown (compare figure 3.10). Clearly noticeable is the Gaussian-like distribution of the PLIF signals as the recorded image suggests. A perfect homogeneous mixture would result in a Dirac delta-function. Inhomogeneity of the mixture as well as unaccounted for diagnostic errors result in a full-width half-maximum of 0.1.

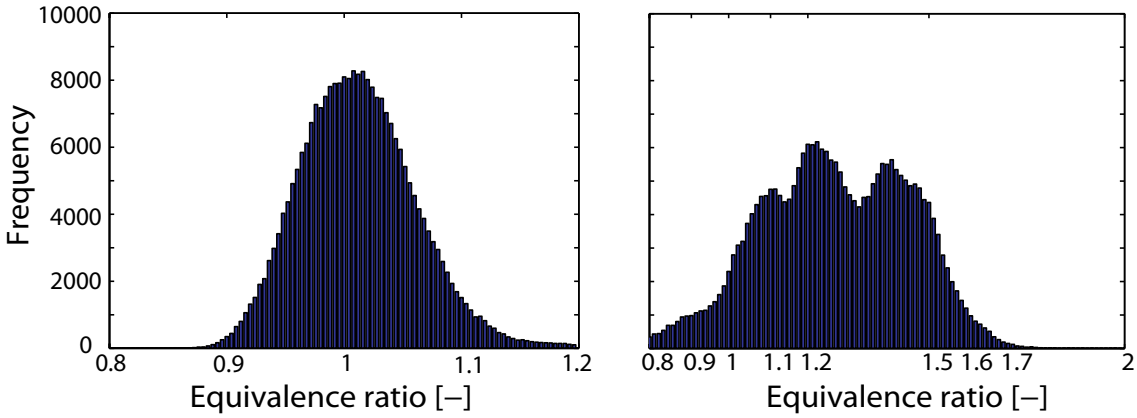

Figure 4.33: Histogram of equivalence ratios from a raw image with port-fuel injection (left) and direct-injection (right). Engine parameters: 1000 rpm, neutral charge motion, injection timing 300° BTDC (direct-injection), global equivalence ratio = 1.

In contrast, a wide distribution appears with direct-injection (same engine operating conditions as above) shown in figure 4.33, right. Here, multiple curve maxima are visible resulting from a locally stratified equivalence ratio distribution. Notice, that in this analysis so far no effects of varying absorption along the laser light path are considered.

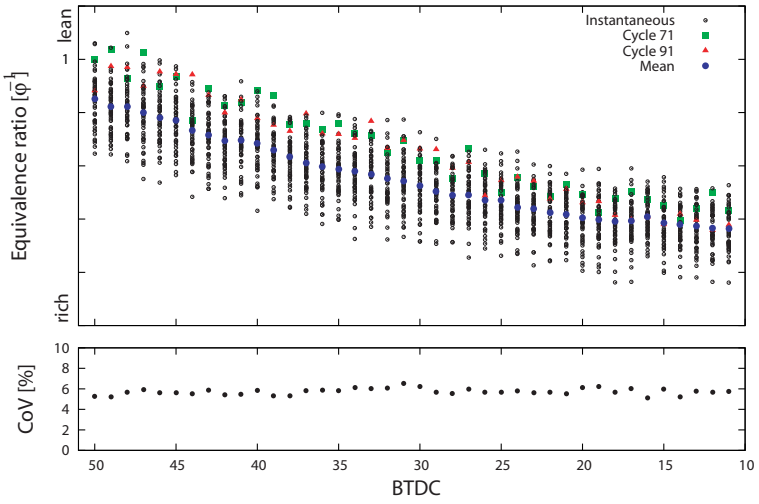

Figure 4.34: Spatial average equivalence ratios of single cycles. Engine parameters: 1000 rpm, neutral charge motion, multi-hole injector (direct-injection), injection timing 300° BTDC.

In figure 4.34, the cycle-to-cycle variations are presented by plotting the ensemble mean equivalence ratio over the corresponding crank angle. Here, the coefficient of variation shows the cyclic fluctuations of ∼5%. The spatial mean equivalence ratios of cycle 71 and 91 are also shown. Both are above average as large portions of the combustion chamber are lean in comparison. Small variations from crank angle to crank angle are prone to detection errors such as out-of-plane motion of flow structures. Notice, the decreasing ensemble mean equivalence ratio over crank angle is due to large amounts of fuel recorded in the field of view, as this indicates inhomogeneities of the fuel distribution. The global equivalence ratio with these engine parameters was set to 1.

Analysis with tumble charge motion

Similar to section 4.1, a tumble charge motion was used to produce a large flow structure rotating clockwise within the field of view. The effects are shown in figure 4.35, as the fluorescence signals show the instantaneous fuel distribution at discrete crank angles. The induced flow structure carries the evaporating fuel in a clockwise direction towards the inlet valves (left). The transient process is superimposed by increasing pressure and temperature as well as convection and diffusion transport processes. Decreasing signal intensities indicate the evaporation process, as fluorescence signal levels of liquid tracer are magnitudes higher than gaseous. The sequence of raw images only shows a 10 mm slice above the piston crown where evaporation of liquid fuel occurs.

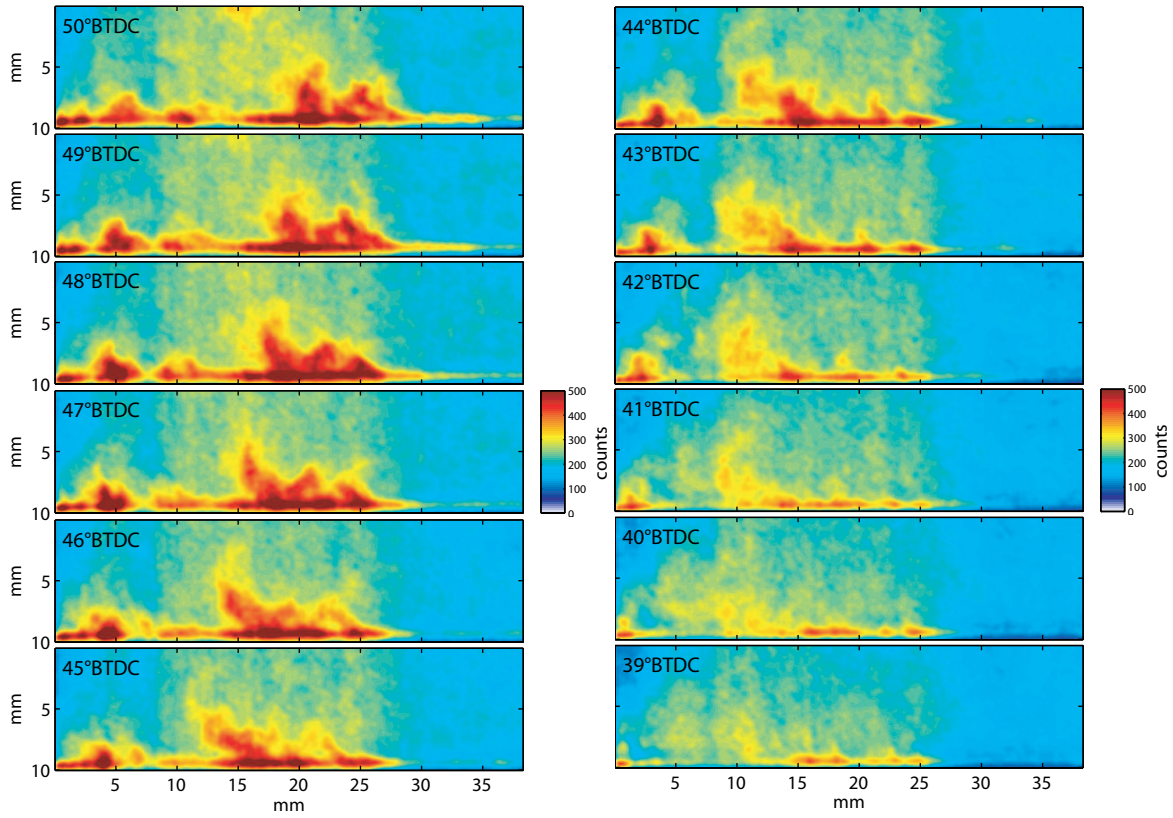

Figure 4.35: Temporal evolution of piston wetting and fuel film evaporation within a single cycle. Engine speed: 1000 rpm, tumble charge motion.

4.3.2 Analysis of wall-wetting effects

Wall-wetting in an engine environment is an unintentional wetting of in-cylinder components (piston crown, liner, spark-plug, etc.) with liquid fuel. These deposits influence the wall-heat conductivity and increase the production of unburned hydrocarbons as well as soot particles. Ignited deposits on cylinder components are called pool fires and are non-premixed flames. Pool fires exhibit rather long residence times because of diffusion and evaporation processes.

As shown earlier in figure 4.35, liquid deposits on the piston crown are recorded with PLIF. Cycle-to-cycle variations are determined by calculating the ensemble mean intensity of distinctive regions of the recorded images. A panel, the height of 10 mm above the piston crown, was divided into four equally distanced regions shown schematically in figure 4.36.

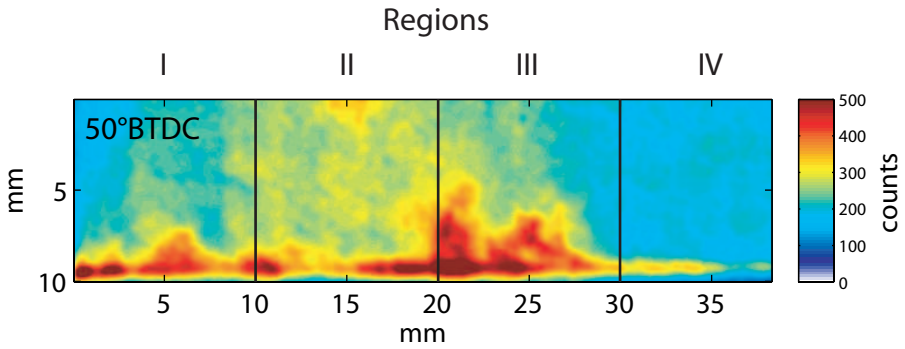

Figure 4.36: Schematic overview of distinctive regions.

Variation of injector / spray shape

In section 4.2 the dynamics of the spray shape and the flow field were investigated. Similarly, this section describes the transient fuel distribution above the piston crown. Figure 4.37 shows the ensemble mean intensities of individual cycles recorded at 1000 rpm with a tumble charge motion. Only 51 cycles of 100 recorded are used in the statistics, as the first 49 cycles are biased due to intensifier instabilities [40]. The strong vortex flow structure forces the fuel distribution in a clockwise rotation and thus, high intensity levels are expected in region 1 and 2.

The spray shape of the multi-hole injector (red) exhibits larger intensities in region 1 and 2 than the annular orifice injector. The main reason for this are the different spray shapes. In reference, the multi-hole injector produces multiple full-cone sprays. These hit the piston crown near the center, increasing the fuel deposits recorded in the field of view. The annular orifice produces a hollow-cone spray, enabling a larger surface to volume ratio. Thus, the deposits on the piston crown are retarded because of the better distribution.

The exponential decrease in intensity over crank angle is subject to evaporation and convective / diffusion transport processes within the cylinder. In regions 3 and 4, as shown in figure 4.37, the differentiation is not so clear. Especially in region 4, the intensities are close together. This indicates a strong deformation of the annular gap orifice spray as shown in the earlier section.

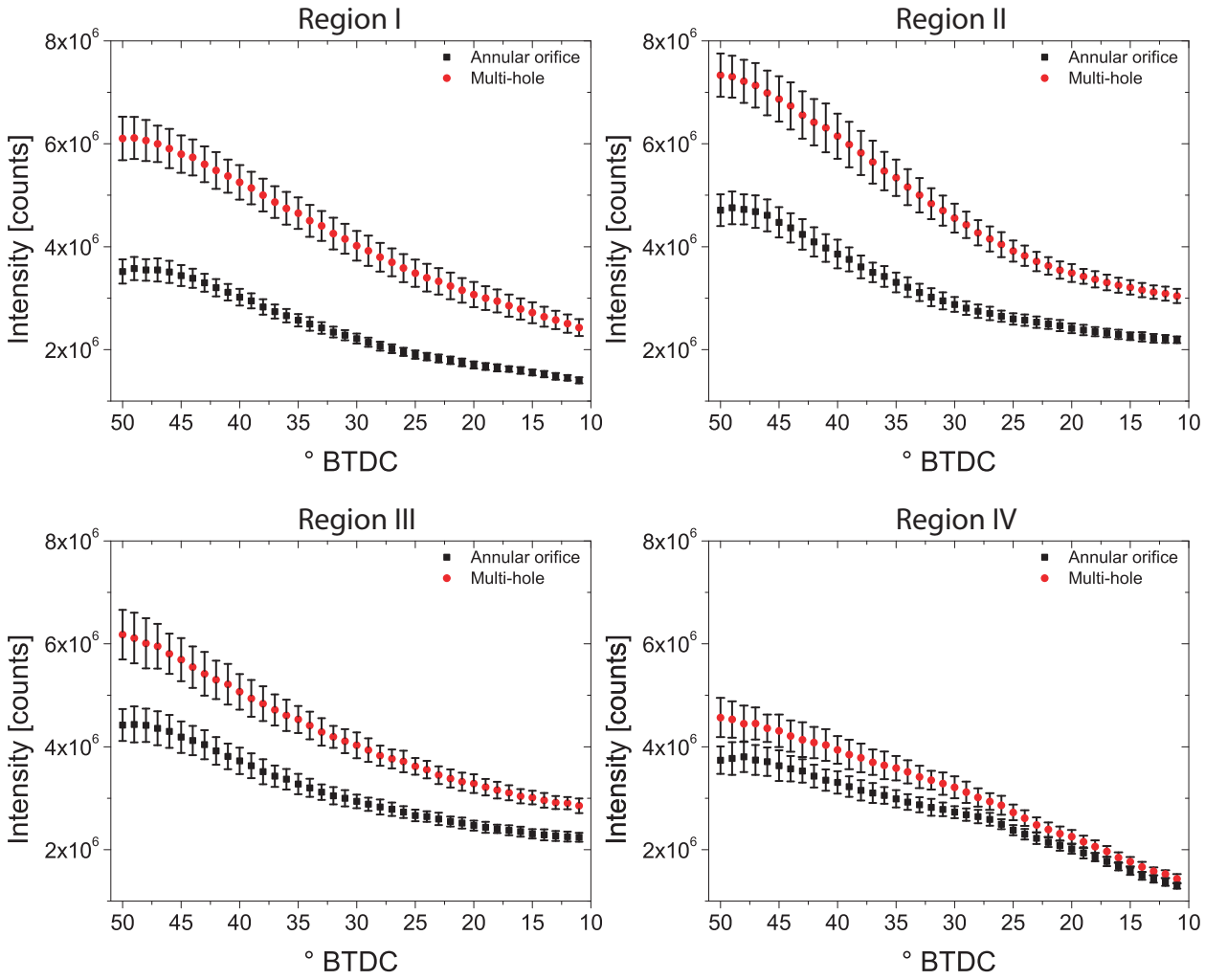

Figure 4.37: Ensemble mean intensities of PLIF signals. Engine parameters: 1000 rpm, tumble charge motion, equivalence ratio = 1. Red: multi-hole injector; black: annular orifice.

In figure 4.38, the fuel distribution above the piston crown of the multi-hole and annular orifice injectors of arbitrary cycles are compared. The three-dimensional plot comprises the temporal evolution (x-axis), its intensity compared to the phase-averaged fuel distribution (z-axis) and the horizontal resolution of the fuel distribution (y-axis). An engine speed of 1000 rpm with a tumble charge motion was used for both recordings.

The strong vortex flow structure of the charge motion is noticeable in both plots early during the recording. This is indicated by the above average fuel deposits between 10 and 30 mm from 50° - 40° BTDC. The drift of the fuel in a clockwise rotation (towards the left) is clearly noticeable. The deposits of a second leg (directed oppositely) of the multi-hole injection are also visible between 40 and 45 mm during the same time interval. The annular orifice with its hollow cone spray shows an inverse behavior. Only the left side shows fuel deposits. This is similar to the spray shape shown in figure 4.29. With the continuing evaporation process, the intensities decrease to lower levels.

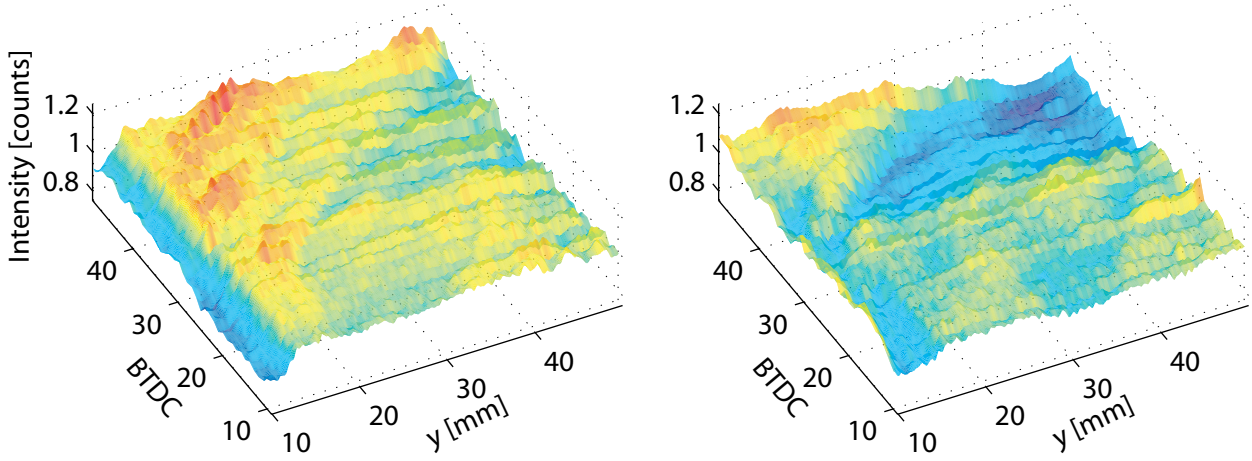

Figure 4.38: Comparison of fuel distribution via intensity (vertically summed). Left: multi-hole injector; right: annular gap orifice; engine parameters: 1000 rpm, tumble charge motion.

Variation of equivalence ratio

The continuous range between low-, mid-, and high-loads during engine operation require distinctive air / fuel mixtures. In the transient section between mid- and high-loads, lower equivalence ratios (leaner mixtures) are used to reduce fuel consumption and the possibility of unburned hydrocarbons. While the engine conditions (engine speed, intake mass flow, etc.) are kept the same, the injected fuel mass directly influences λ.

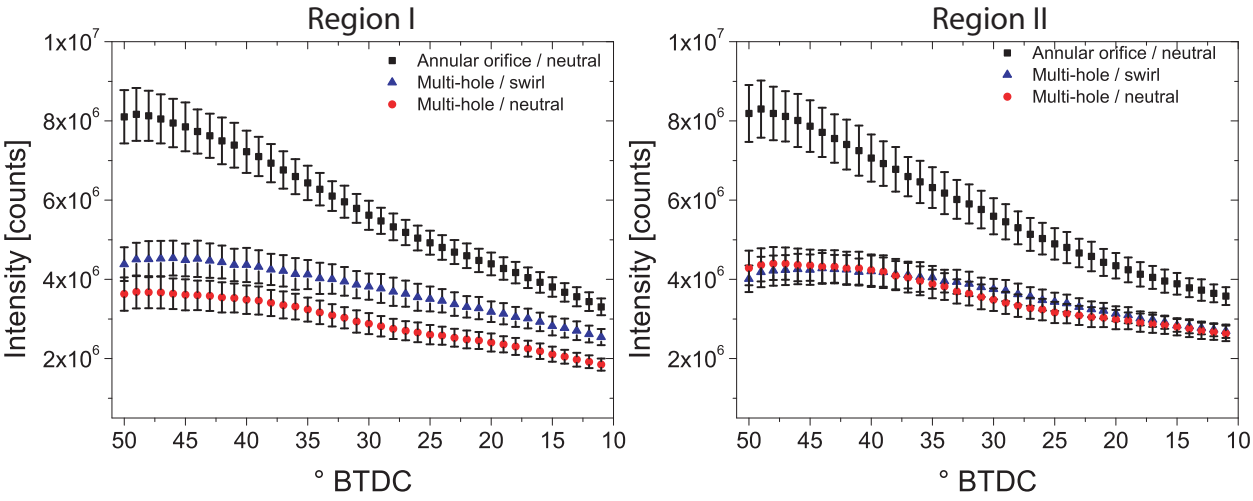

Figure 4.39: Ensemble mean intensities of PLIF signals. Engine parameters: 1000 rpm, equivalence ratio = 1.

In figure 4.39 and 4.40, the ensemble-averaged intensities of the multi-hole and annular orifice injectors at 1000 rpm and an equivalence ratio of 1 are compared. The influence of the flow field structures (neutral and swirl charge motion) is rather low with the multi-hole injector. Both distributions show an approximately equal intensity above the piston crown, albeit the swirl charge motion forces more deposits in region 1 and 4 (as expected). The drift, as shown in figure 4.26, (section 4.2), also indicates this behavior. The annular orifice however, exhibits large intensities

during early crank angles in regions 1 and 2. An influence of the flow motion is not recognized. The fuel distribution, high in region 1 and 2, is attributed to the hollow cone spray shape. Further, the reduced flow convection transport is expected to have little influence because of the undirected, small flow structures which dissipate more easily (see section 4.1.2).

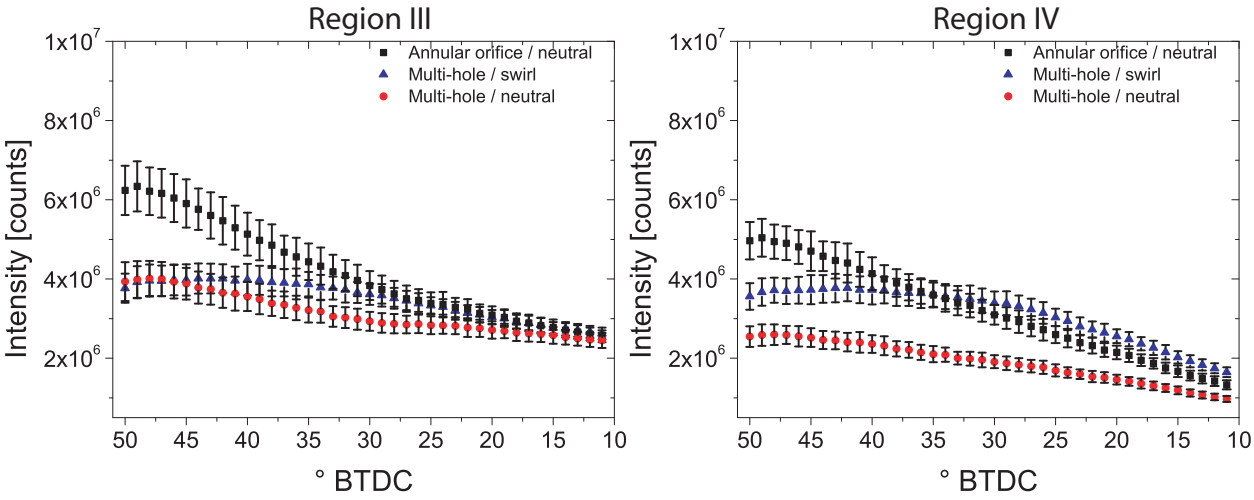

Figure 4.40: Ensemble mean intensities of PLIF signals. Engine parameters: 1000 rpm, equivalence ratio = 1.

In a parametric variation the equivalence ratio was set to 1.2^{-1} (air number of 1.2), retaining all other engine conditions. In figure 4.41 and 4.42, the ensemble mean intensities of the individual regions are shown.

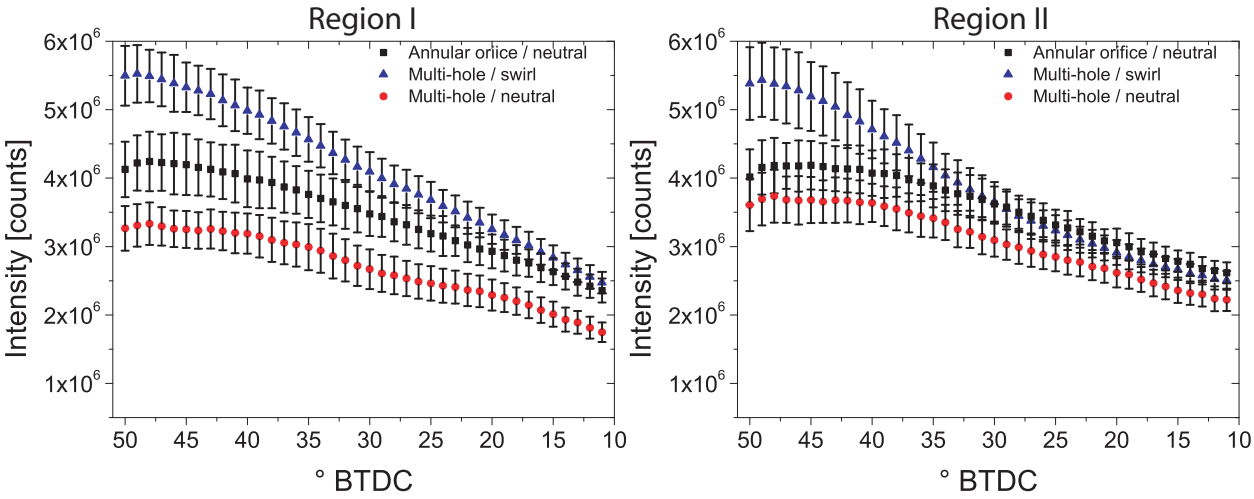

Figure 4.41: Ensemble mean intensities of PLIF signals. Engine parameters: 1000 rpm, equivalence ratio = 1.2^{-1}.

In comparison to the recordings with equivalence ratio of 1, the intensities are lower, as less fuel is injected (as expected). However, the annular orifice injector shows much lower intensities compared to the signal levels of the multi-hole injector.

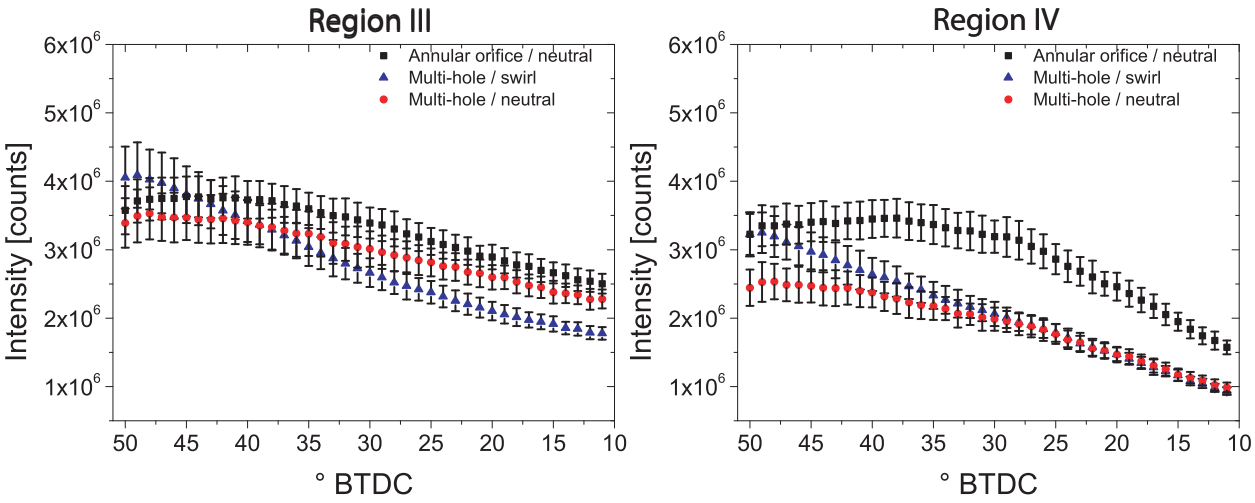

Figure 4.42: Ensemble mean intensities of PLIF signals. Engine parameters: 1000 rpm, equivalence ratio = 1.2^{-1}.

4.3.3 Conclusions

This section presents the feasibility of quantifying the spatial equivalence ratio within an internal combustion engine at a temporal repetition rate of 6 kHz using planar laser-induced fluorescence. Multiple consecutive cycles were recorded to achieve a dataset for statistical evaluation. For a realistic engine operation, a fluorescing reference fuel was used without additional added tracer. To attribute fluorescence signals with equivalence ratios, a calibration process was developed. Strong cyclic variations were identified and analyzed as well as the variability of in-cylinder flow structures and their influence onto the air / fuel mixing process. The charge motions presented a strong influence forcing different spatial distributions of the equivalence ratio within the field of view.

In a parametric study, different injector / flow field combinations were investigated in respect to wall-wetting. Albeit the multi-hole injector presented higher fuel concentrations near the piston crown with a tumble charge motion, an inverse behavior is seen with a neutral or swirl charge motion. The annular orifice injector behaves vice versa. Additionally, the imaging method showed instantaneous fluorescence signals of the transient fuel motion above the piston crown.

4.4 Flame kernel development

Overview

As presented in [58], the information on the transient flame propagation inside the cylinder of an internal combustion engine is a substantial part for an improved understanding guiding the development of higher efficiencies and reduced pollutant emissions. The measurement of the flame kernel development presents the feasibility to temporally resolve the evolution of spark-ignited flame kernels using a single laser / camera system.

In contrast to previous approaches such as recording Mie-scattering of evaporating seeding droplets to mark the flame kernel [50] or using multiple intensified CCD and clustered flash lamp-pumped Nd:YAG laser technology [57], the methodology presented here relies on continuous pulse sequences and intensified CMOS-cameras. This enables a more detailed view upon cycle-to-cycle variations (ccv) because a large number of sequential combustion cycles is recorded. The appearance of ccv is an unwanted disturbance in engines, especially in current spray-guided direct-injection spark-ignition (DISI) engine configurations. To characterize ccv, an adequate temporal resolution is required to comprehend the flame structures and their variability in time and space. Therefore, the flame kernel evolution of sequential cycles is an important cornerstone of understanding the origins of ccv during combustion.

The method of choice to mark the flame front is planar laser-induced fluorescence (PLIF). The excitation of diatomic molecules such as OH is a standard procedure within laser combustion diagnostics and is widely accepted for representing the instantaneous flame front position [121, 122, 82]. High-speed imaging of atmospheric turbulent flames using the steep gradient of OH-radicals as an indicator of the flame front has been demonstrated in [60, 55, 83, 123]. Depending on the time-scales to be resolved, such as the integral time-scale of a turbulent flow, the repetition rate must be chosen accordingly. Integral time-scales in turbulent flames are typically in the millisecond-range [124]. Therefore, repetition rates must be in the kilohertz-range. Time-scales of interest studying flame dynamics and ccv in IC engines are $\sim 1^\circ$ CA and therefore scale with the engine speed. At 1000 rpm, the temporal resolution of 1° CA per image corresponds to 6 kHz. Thus, the techniques developed for studying transients in turbulent flames are transferred and adopted to in-cylinder processes of a DISI engine. The engine specific setup is presented in figure 3.12 with the field of view in figure 3.13 (section 3.6).

Temporal flame kernel development and flame propagation throughout the cylinder is of common interest [54, 57, 56, 49, 50, 4]. Whereas recording OH chemiluminescence within an IC engine at 10 Hz is well established [56], measuring the transient flame front propagation during individual cycles is still a challenge. The benefit of the present approach using OH-PLIF at 6 kHz is temporally resolved imaging of the flame kernel development at a large field of view. From this transient data flame contours and their propagation speeds can be extracted for individual cycles. Parameters such as engine speed, charge motion and timing (injection and ignition) influence the propagation speed and burning time. Especially exhaust gas recirculation (EGR) does strongly impact the engine characteristics. Most notably, EGR at partial load operation is used to reduce NO_x exhaust emissions and increase engine efficiency by mixing intake air with exhaust gas to a ratio of up to 20%. As a result of this mixing process, flame speeds are retarded and burning times increase. Using high-speed flame kernel imaging, this influence can be studied in detail as presented here.

4.4.1 Analysis of single cycles

Figures 4.43 and 4.44 show the temporal evolution of individual flame kernels represented by instantaneous OH-radical distributions at different levels of EGR. Images shown are after post-processing as outlined in section 3.6. They are separated by 1 or 2° CA and only a sector of the full view is presented (see figure 3.13). EGR is varied from 0 - 20% as noted in the figure captions.

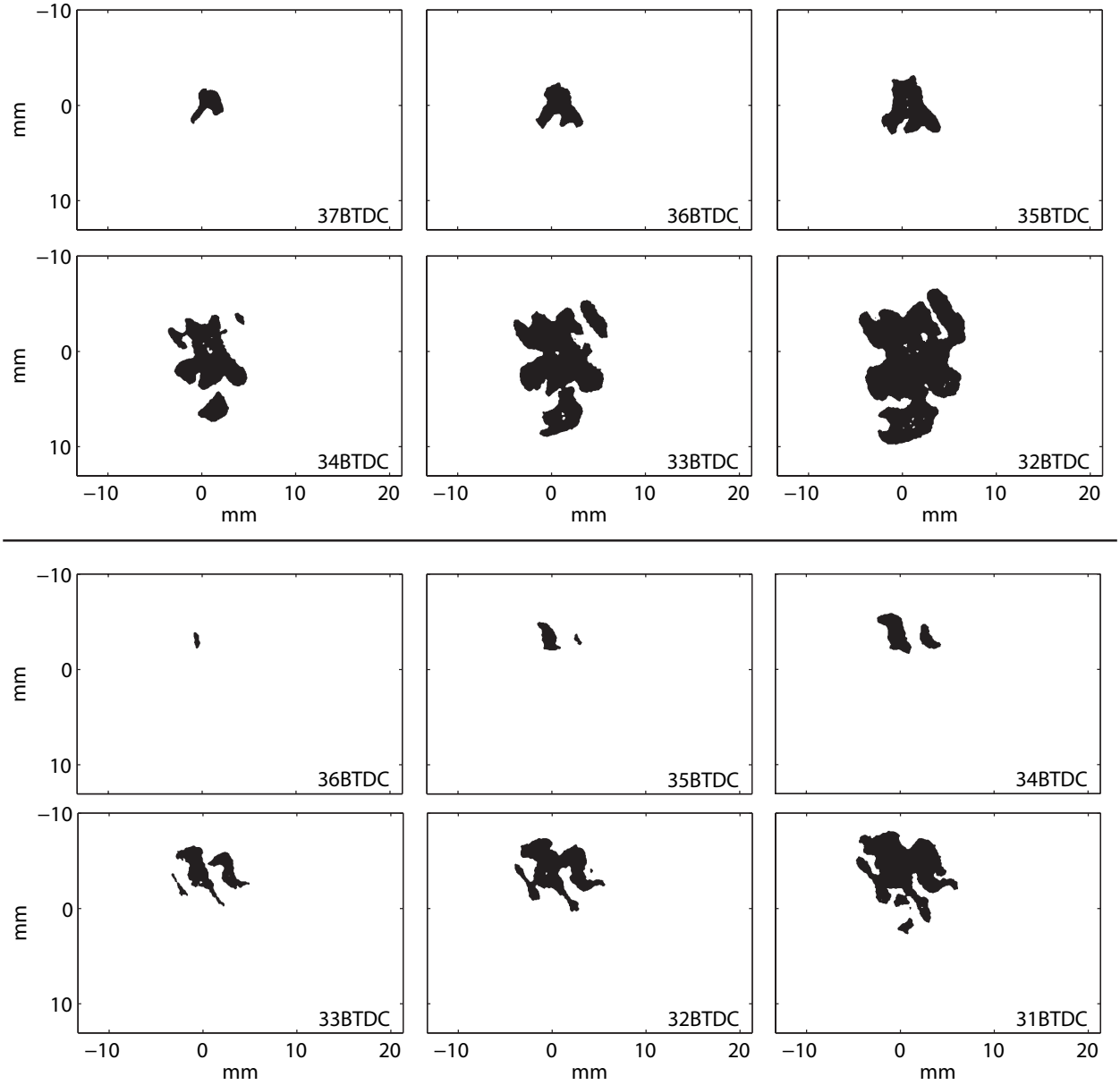

Figure 4.43: Flame kernel development during individual engine cycles at 1000 rpm. The kernel growth is derived from transient OH-radical distributions recorded with a repetition rate of 6 kHz (engine settings are detailed in section 3.6). In the top sequence no exhaust gas was recirculated (0% EGR), in the bottom case 10% EGR was used. The spark plug position is at x, y = 0, 0. The vertical orientation of the laser light sheet is just above the top dead center point of the cylinder.

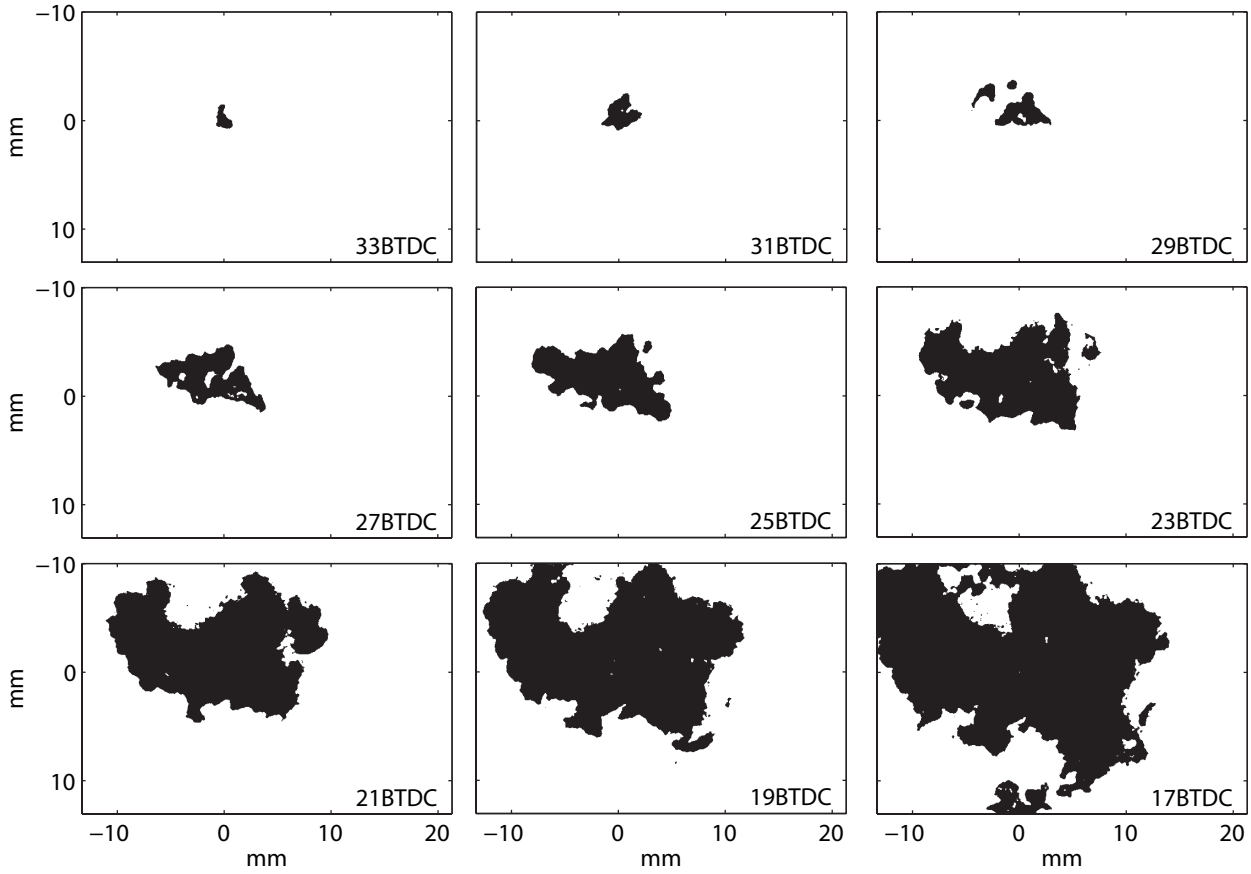

Figure 4.44: Individual engine cycle with 20% EGR. Obviously flame growth is retarded significantly compared to the cases with 0 and 10% EGR.

Obviously, the location of the first entry of the flame front into the laser light sheet plane is near the spark plug (x, y = 0 mm). The size of the flame kernel expands continuously until the edge of the field of view is reached. The PLIF-signal intensity is sufficiently good (SNR of 7) to extract the flame front and its propagation in the measurement plane during individual engine cycles.

A statistical analysis of the flame area propagation is shown in figure 4.45, left. The error bars represent the standard deviation (1-σ range) of the dataset and the central measurement points represent the average flame area growth. The dataset consists of 50 individual cycles which were consecutively recorded. Due to cyclic variations of local turbulence properties and residual gas composition, the flame area scatters significantly. To illustrate the variability of the process two extreme cases with growth rates above and below the 1-σ range are included in figure 4.45, left. Notice that the temporally tracking of the flame growth of individual cycles as demonstrated here is only possible with high-speed technology based on continuous pulse sequences at kHz repetition rates.

In figure 4.45, right, the in-cylinder pressure curves for cycles 13 and 32 of the dataset are shown. The pressure curve of cycle 13 corresponds to the flame area growth rate presenting a steeper gradient than cycle 32. For cycle 32, the growth rate is retarded and the peak is shifted beyond TDC. The integral area below the pressure curve also indicates a shift of the position of the 50% mass fraction burned center towards later crank angles. In comparison to the flow fields (see chapter 4.1)

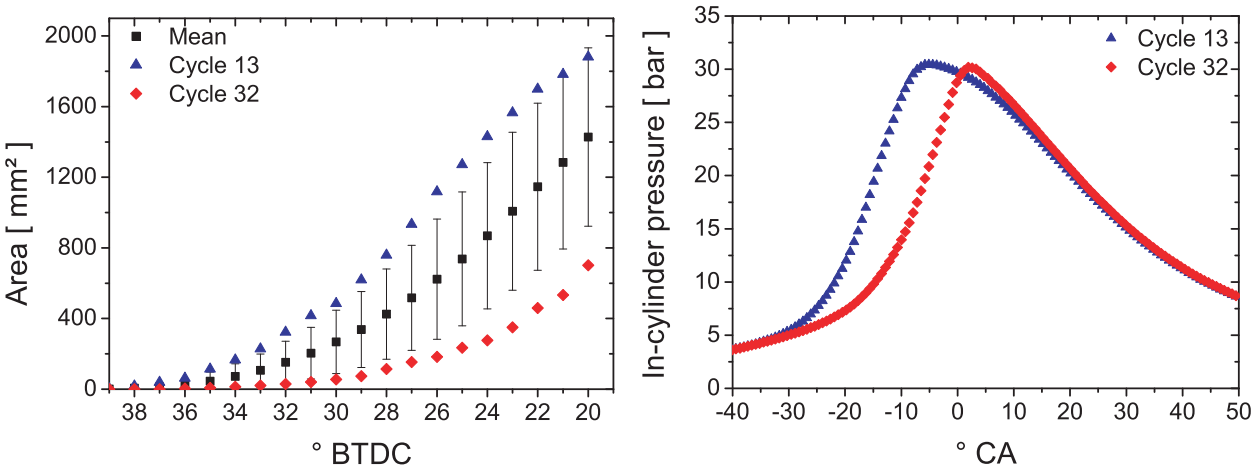

Figure 4.45: Analysis of the flame area propagation at 1000 rpm without EGR (left). The error bars represent the standard deviation of the dataset. The corresponding in-cylinder pressure progress of the single cycles is shown on the right. 0° CA is TDC of the compression stroke.

and fuel distribution (see chapter 4.3), the cyclic variations are prominently noticeable. In a logical consequence, especially the single cycles of the flow fields with a strong tumble vortex (above average kinetic energy) should correlate with an intensified flame growth speed. A homogeneous mixture within the combustion chamber shown by the air / fuel distribution measurements should also indicate this (simultaneous recorded data is required for validation!).

Notice planar imaging of the OH-radicals provides only a quantitative measure of the flame kernel growth inside the laser sheet. Due to the out-of-plane motion (as shown by the flow field analysis in chapter 4.1), they do not give an overall picture of the three-dimensional flame growth as for example pressure based measurements. However, pressure measurements are not as sensitive as OH-PLIF during early flame kernel development where the pressure increase is small [50]. In contrast, the here presented technique provides high temporal and spatial resolution, thus allowing a good characterization of the early flame kernel growth to a wrinkled turbulent flame.

4.4.2 Analysis of EGR influence

For different EGR rates, the temporal development of the initial spark-ignited flame kernel differs significantly. With increasing EGR, the flame growth speed is reduced. For 0% EGR (figure 4.43), the flame kernel grows into the measurement plane approximately at 37° BTDC. Increasing the EGR rate to 10%, the arrival at the measurement plane is delayed by only 1 - 2° CA but at an EGR rate of 20% (figure 4.44), first OH signals appear earliest at ∼33° BTDC. Similarly, the flame kernel growth rate decreases significantly with increasing EGR rate. Differences in the flame area growth rate are most pronounced when switching from 0% to 10% EGR as shown in figure 4.46. For 20% EGR, especially during the initial phase up to 25° BTDC, the flame kernel grows only marginally, whereas without EGR, the kernel increases constantly and much more rapidly. Mean and the according coefficient of variation are computed from 50 cycles at each EGR level.

One reason for the decreasing growth rates with increasing EGR is the decrease in laminar flame speeds due to the increase in mole fraction of inert gases, which also presents decreasing flame

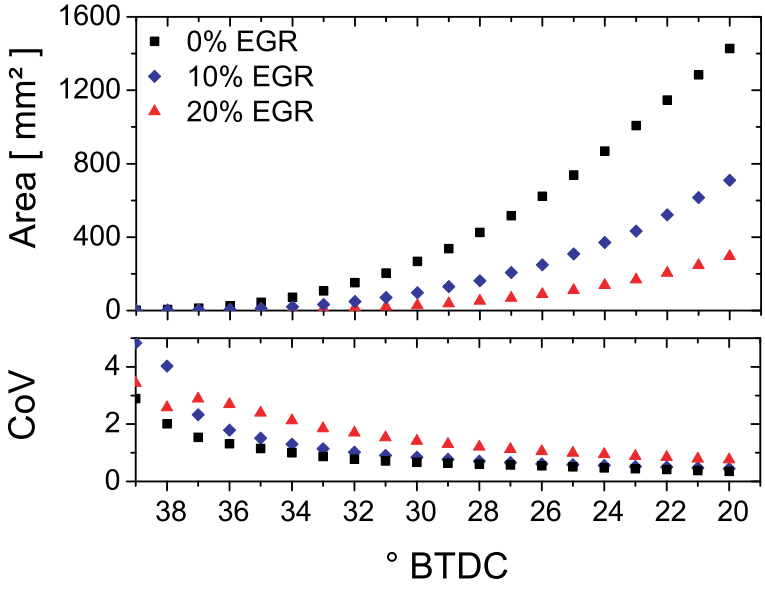

Figure 4.46: Statistical analysis of data at 1000 rpm with different EGR rates. The top graph shows the mean flame area for different EGR rates. The bottom graph represents the associated coefficient of variation.

temperatures. Lower laminar flame speeds in turn reduce turbulent flame speeds that are actually observed here in a two-dimensional projection. A more in-depth analysis with a simultaneous recording of the flow field is thus necessary.

4.4.3 Conclusions

This experiment presents the feasibility to track the transient flame front by recording instantaneous images with planar laser-induced fluorescence of OH-radicals. The repetition rate of 6 kHz enabled the recording of consecutive cycles at a single crank angle resolution.

The presented use of exhaust gas recirculation is a prominent route to reduce NO_x-emissions. The analytical method of the flame area growth rate clearly allows a quantification of how the gas composition impacts the flame propagation dynamics. A correlation to the conventional pressure measurements was also presented.

5 Summary and Outlook

This work investigates the in-cylinder processes of a direct-injection spark-ignition gasoline internal combustion engine using high-speed laser diagnostics. The flow field, the air / fuel mixture formation and in-cylinder distribution, as well as the flame kernel development were analyzed. Using high-speed diagnostics, the temporal and spatial resolution of the recordings suffices the need for a more detailed view of the cause-and-effect chains. Especially the ability to record single cycles exemplified at discrete crank angles shows this progress.

The flow field exhibits an important influence onto the fuel distribution and subsequent flame kernel growth and propagation. Using stereoscopic PIV at single crank angle resolution (6 kHz at 1000 rpm), the in-cylinder flow field was recorded throughout the compression stroke from 180 - 60° BTDC. Single cycles were analyzed for their individual cyclic variation. These are presented by the use of statistical tools like the kinetic energy as well as the instantaneous flow fields.

The novelty of these recordings was the introduction of high-speed stereoscopic PIV to an engine flow field which allowed the recording of all three velocity components within the measuring plane. This especially presented the influence of the out-of-plane within different charge motion configurations which until then was not fully experimentally investigated. The tumble charge motion is only influenced little and data obtained with conventional PIV suffices. The influence during a swirl charge motion is more prominent. Especially the aspect of a tilted swirl axis (not parallel to the cylinder axis) is an important result. With it, the understanding about the influence of the circular drag on the fuel distribution is increased. The transport motion is oriented in multiple directions, rather than perpendicular to the cylinder axis. Additionally, the comparison of the kinetic and turbulent kinetic energies for different charge motions further increased the knowledge about the influence of the out-of-plane component. By substituting the out-of-plane velocity with the in-plane velocities (superposition), the orientation of the fluctuating flow field showed an isotropic behavior for the compression stroke.

The next experiment focused on the interaction of the flow field and the subsequent spray development during stratified fuel injection. Together with conventional PIV (only in-plane velocities are recorded) at 6 kHz, the flow field and the subsequent spray injection were recorded in multiple consecutive cycles. Because of the large spray momentum upon injection, the flow field has no influence on the penetration depth. However, when comparing the spray drift, which focuses on the deformation of the spray by influence of the large scale flow structures, the tumble charge motion presented a large influence. Multiple injector / spray shapes are addressed and their respective characteristic behavior.

The air / fuel distribution during the compression stroke (50° - 10° BTDC) was recorded using laser-induced fluorescence at 6 kHz. The results showed the inhomogenization of the fuel with a standard early injection at 300° BTDC using different injectors and charge motions. The fuel used was a reference fuel without any additional tracer added. This presented a novelty as earlier investigations relied on non-fluorescing fuels (e.g. iso-octane) doped with an additional tracer

(e.g. biactetyl, toluene, etc.). A calibration method of determining the equivalence ratio was developed. Additionally, the wall-wetting effects of individual injector / flow field combinations were investigated upon preferential deposit sections on top the piston crown.

Subsequently, at the height of the in-cylinder pressure curve, the flame kernel development was analyzed using high-speed OH-PLIF. The novelty of this methodology introduced sequential cycles of crank angle ranges in which cyclic variations of the flame kernel growth are identifiable. The influence of using exhaust gas recirculation onto the flame kernel growth was also analyzed. A comparison to conventional in-cylinder pressure measurements and the benefit of using laser diagnostics was shown.

The above mentioned experiments can be used to detail the in-cylinder processes and understand the thermo-fluidic background. Recent research of these methods applied simultaneously show a more comprehensive view. For instance, a future application of 3C-PIV / OH-PLIF inside the combustion chamber combined with solid particle seeding would allow for a complete cycle analysis concerning the intake and compression stroke as well as the combustion phase. The PIV setup can record the flow field and thus describe the convective transport of the flame. With the OH-PLIF setup, the flame front is tracked by recording the intermediate species simultaneously. The flame propagation speed, which is an important quantity when comparing combustion qualities, would be readily available.

Another interesting cause-and-effect chain needing further investigation is the heat transfer at walls. This is possible using thermographic phosphors to measure the wall temperature inside the cylinder at high repetition rates. The gaseous temperature within the boundary layer can be measured with toluene LIF or CARS. Resulting from both measurements recorded simultaneously is the heat flux as an important quantity influencing engine efficiency.

Inside the cylinder, the recording of the transient flow structures is limited with PIV (two- or three-component) to a two-dimensional plane. Adapting tomographic PIV would increase the spatial-temporal recordings to include the distinct three-dimensional flow structures and enable the determination of the deformation tensor. This would improve the understanding of the physical forces which hence control the flow structures.

Returning to the initial consent to improve the efficiency and reduce exhaust gas emissions, the data shown in this work is also useful for the validation of numerical simulations. Especially the decoding of the origins of cyclic variations and its effects are necessary for valid results of these simulations as they can be used to improve the engine development towards more robustness, higher power, and better efficiency.

Bibliography

[1] George Eads. 50by50 Prospects and Progress. Technical report, FIA Foundation for the Automobile and Society, 2011. 1

[2] J.B. Heywood. *Internal combustion engine fundamentals*. McGraw-Hill, 1989. 1, 9, 10, 11, 14, 20, 90, 117

[3] Kyoto protocol. Technical report, United Nations Framework Convention on Climate Change, 1998. 1

[4] V. Sick, M.C. Drake, and T.D. Fansler. High-speed imaging for direct-injection gasoline engine research and development. *Exp. Fluids*, 49:937–947, 2010. 3, 99

[5] G. Rassweiler and L. Withrow. Motion pictures of engine flames correlated with pressure cards. *SAE Paper*, 1938. 3

[6] D.L. Reuss, M. Bardsley, P.G. Felton, C.C. Landreth, and R.J. Adrian. Velocity, vorticity, and strain-rate ahead of a flame measured in an engine using particle image velocimetry. *SAE Paper*, 900053, 1990. 3

[7] D.L. Reuss, R.J. Adrian, C.C. Landreth, D.T. French, and T.D. Fansler. Instantaneous planar measurements of velocity and large-scale vorticity and strain rate in an engine using particle-image velocimetry. *SAE Paper*, 890616, 1989. 3

[8] W. Stolz, J. Köhler, W. Lawrenz, F. Meier, W.H. Bloss, R.R. Maly, R. Herweg, and M. Zahn. Cycle resolved flow field measurements using a PIV movie technique in a SI engine. *SAE Paper*, 922354, 1992. 3

[9] M. Reeves, D.P. Towers, B. Tavender, and C.H. Buckberry. A high-speed all-digital technique for cycle-resolved 2-D flow measurement and flow visualisation within SI engine cylinders. *Optics Lasers Eng.*, 31:247–261, 1999. 3, 81

[10] D.P. Towers and C.E. Towers. Cyclic variability measurements of in-cylinder engine flows using high-speed particle image velocimetry. *Meas. Sci. Tech.*, 15:1917–1925, 2004. 3, 42, 81

[11] S. Jarvis, T. Justham, A. Clarke, C.P. Garner, G.K. Hargrave, and N.A. Halliwell. Time resolved digital PIV measurements of flow field cyclic variation in an optical engine. *J. of Physics: Conf. Series*, 45:38–45, 2006. 4

[12] T. Justham, S. Jarvis, A. Clarke, C.P. Garner, G.K. Hargrave, and N.A. Halliwell. Simultaneous study of intake and in-cylinder IC engine flow fields to provide an insight into intake induced cyclic variations. *J. of Physics: Conf. Series*, 45:146–153, 2006. 4

[13] C.M. Fajardo, J.D. Smith, and V. Sick. Sustained simultaneous high-speed imaging of scalar and velocity fields using a single laser. *Appl. Phys. B*, 85:25–31, 2006. 4, 6

[14] S.H.R. Müller, B. Böhm, M. Gleißner, R. Grzeszik, S. Arndt, and A. Dreizler. Flow field measurements in an optically accessible, direct-injection spray-guided internal combustion engine using high-speed PIV. *Exp. Fluids*, 48:281–290, 2010. 4, 21, 60, 64, 77, 81

[15] C. Fajardo and V. Sick. Development of a high-speed UV particle image velocimetry technique and application for measurements in internal combustion engines. *Exp. Fluids*, 46:43–53, 2009. 4, 81

[16] I. Cosadia, J. Borée, G. Charnay, and P. Dumont. Cyclic variations of the swirling flow in a diesel transparent engine. *Exp. Fluids*, 41:115–134, 2006. 4

[17] I. Cosadia, J. Borée, and P. Dumont. Coupling time-resolved PIV flow-fields and phase-invariant proper orthogonal decomposition for the description of the parameters space in a transparent diesel engine. *Exp. Fluids*, 43:357–370, 2007. 4

[18] L. Graftieaux, M. Michard, and N. Grosjean. Combining PIV, POD and vortex identification algorithms for the study of unsteady turbulent swirling flows. *Meas. Sci. Tech.*, 12:1422–1429, 2001. 4, 18

[19] J.B. Ghandhi, R.E. Herold, J.S. Shakal, and T.E. Strand. Time resolved particle image velocimetry measurements in an internal combustion engine. *SAE Paper*, 2005-01-3868, 2005. 4

[20] J. Vétel, A. Garon, and D. Pelletier. Vortex identification methods based on temporal signal-processing of time-resolved PIV data. *Exp. Fluids*, 48:441–459, 2009. 4

[21] P. Druault, P. Guibert, and F. Alizon. Use of proper orthogonal decomposition for time interpolation from PIV data. *Exp. Fluids*, 39:1009–1023, 2005. 4, 17, 45

[22] D.L. Reuss. Cyclic variability of large-scale turbulent structures in directed and undirected IC engine flows. *SAE Paper*, 2000-01-0246, 2000. 4

[23] C. Funk, V. Sick, D.L. Reuss, and W.J.A. Dahm. Turbulence properties of high and low swirl in-cylinder flows. *SAE Paper*, 2002-01-2841, 2002. 4

[24] I. Grant, S. Fu, X. Pan, and X. Wang. The application of an in-line, stereoscopic, PIV system to 3-component velocity measurements. *Exp. Fluids*, 19:214–221, 1995. 4

[25] K. Hinsch. Three-dimensional particle velocimetry. *Meas. Sci. Tech.*, 6:742–753, 1995. 4, 22, 117

[26] C. Brücker. 3D scanning PIV applied to an air flow in a motored engine using digital high-speed video. *Meas. Sci. Tech.*, 8:1480–1492, 1997. 4

[27] C. Willert. Stereoscopic digital particle image velocimetry for application in wind tunnel flows. *Meas. Sci. Tech.*, 8:1465–1479, 1997. 4, 28

[28] A.K. Prasad. Stereoscopic particle image velocimetry. *Exp. Fluids*, 29:103–116, 2000. 4, 28

[29] L. Kapitza, O. Imberdis, H.P. Bensler, J. Willand, and D. Thévenin. An experimental analysis of the turbulent structures generated by the intake port of a DISI-engine. *Exp. Fluids*, 48:265–280, 2010. 4

[30] P. Guibert and L. Lemoyne. Dual plane image velocimetry for transient flow field measurements. *Exp. Fluids*, 33:355–367, 2002. 4

[31] M. Voisine, L. Thomas, J. Borée, and P. Rey. Spatio-temporal structure and cycle to cycle variations of an in-cylinder tumbling flow. *Exp. Fluids*, 50:1393–1407, 2011. 4, 62

[32] J.A. Mullin and W.J.A. Dahm. Dual-plane stereo particle image velocimetry (DSPIV) for measuring velocity gradient fields at intermediate and small scales of turbulent flows. *Exp. Fluids*, 38:185–196, 2005. 4

[33] G. Elsinga, F. Scarano, B. Wieneke, and B. van Oudheusden. Tomographic particle image velocimetry. *Exp. Fluids*, 41:933–947, 2006. 4, 22

[34] C. Schulz and V. Sick. Tracer-LIF diagnostics: quantitative measurement of fuel concentration, temperature and fuel / air ratio in practical combustion systems. *Prog. Energy Comb. Sci.*, 31:75–121, 2005. 5, 32, 52

[35] K. Kuwahara and H. Ando. Diagnostics of in-cylinder flow, mixing and combustion in gasoline engines. *Meas. Sci. Tech.*, 11:R95–R111, 2000. 5, 81

[36] D. Frieden and V. Sick. Investigations of the fuel injection, mixing and combustion processes in an SIDI engine using quasi-3D LIF imaging. *SAE Paper*, 2003-01-0068, 2003. 5

[37] J.D. Smith and V. Sick. Crank-angle resolved imaging of biacetyl laser-induced fluorescence in an optical internal combustion engine. *Appl. Phys. B*, 81:579–584, 2005. 5

[38] J.D. Smith and V. Sick. Quantitative, dynamic fuel distribution measurements in combustion-related devices using laser-induced fluorescence imaging of biacetyl in iso-octane. *Proc. Comb. Inst.*, 31:747–755, 2007. 5

[39] R. Gordon, C. Heeger, and A. Dreizler. High-speed mixture fraction imaging. *Appl. Phys. B*, 96:745–748, 2009. 5, 50

[40] V. Weber, J. Brübach, R.L. Gordon, and A. Dreizler. Pixel-based characterisation of CMOS high-speed camera systems. *Appl. Phys. B*, 103:421–433, 2011. 5, 32, 51, 94

[41] M. Gold, J. Stokes, R. Morgan, M. Heikal, G. de Sercey, and S. Begg. Air-fuel mixing in a homogeneous charge DI gasoline engine. *SAE Paper*, 2001-01-0968, 2001. 5

[42] S. Einecke, C. Schulz, and V. Sick. Measurement of temperature, fuel concentration and equivalence ratio fields using tracer LIF in IC engine combustion. *Appl. Phys. B*, 71:717–723, 2000. 5

[43] B. Williams, P. Ewart, R. Stone, H. Ma, H. Walmsley, R. Cracknell, R. Stevens, D. Richardson, J. Qiao, and S. Wallace. Multi-component quantitative PLIF: Robust engineering measurements of cyclic variation in a firing spray-guided gasoline direct injection engine. *SAE Paper*, 2008-01-1073, 2008. 5

[44] B. Williams, P. Ewart, X. Wang, R. Stone, H. Ma, H. Walmsley, R. Cracknell, R. Stevens, D. Richardson, H. Fu, and S. Wallace. Quantitative planar laser-induced fluorescence imaging of multi-component fuel/air mixing in a firing gasoline-direct-injection engine: Effects of residual exhaust gas on quantitative PLIF. *Comb. Flame*, 157:1866–1878, 2010. 5

[45] R.E. Stevens, H. Ma, C.R. Stone, H.L. Walmsley, and R. Cracknell. On planar laser-induced fluorescence with multi-component fuel and tracer design for quantitative determination of fuel concentration in internal combustion engines. *Proc. IMECHE Part D: J. Automobile Eng.*, 221:713–724, 2007. 5

[46] A. Grosch, V. Beushausen, H. Wackerbarth, O. Thiele, T. Berg, and R. Grzeszik. Calibration of mid-infrared transmission measurements for hydrocarbon detection and propane concentration measurements in harsh environments by using a fiber optical sensor. *J. Quant.Spec.*, 112(6):994–1004, 2011. 5, 50

[47] S.S. Merola, B.M. Vaglieco, G. Formisano, G. Lucignano, and G. Mastrangelo. Flame diagnostics in the combustion chamber of a boosted PFI SI engine. *SAE Paper*, 2007-24-0003, 2007. 6

[48] P. Aleiferis, Y. Hardalupas, A.M.K.P. Taylor, K. Ishii, and Y. Urata. Flame chemiluminescence studies of cyclic combustion variations and air-to-fuel ratio of the reacting mixture in a lean-burn stratified-charge spark-ignition engine. *Comb. Flame*, 136:72–90, 2004. 6

[49] J.D. Smith and V. Sick. Crank-angle resolved imaging of fuel distribution, ignition and combustion in a direct-injection spark-ignition engine. *SAE Paper*, 2005-01-3753, 2005. 6, 99

[50] T.D. Fansler, M.C. Drake, and B. Böhm. High-speed Mie-scattering diagnostics for spray-guided gasoline engine development. In *Proc. of 8th Int. Symposium on Combustion Diagnostics, Baden-Baden*, 2008. 6, 99, 102

[51] M. Knapp, A. Luczak, H. Schlüter, V. Beushausen, W. Hentschel, and P. Andresen. Crank-angle resolved laser-induced fluorescence imaging of NO in a spark-ignition engine at 248 nm and correlations to flame front propagation and pressure release. *Appl. Optics*, 35:4009–4017, 1996. 6

[52] R. Suntz, H. Becker, P. Monkhouse, and J. Wolfrum. Two-dimensional visualization of the flame front in an internal combustion engine by laser-induced fluorescence of OH-radicals. *Appl. Phys. B*, 47:287–293, 1988. 6

[53] A. Arnold, H. Becker, R. Suntz, P. Monkhouse, J. Wolfrum, R. Maly, and W. Pfister. Flame front imaging in an internal-combustion engine simulator by laser-induced fluorescence of acetaldehyde. *Optics Letters*, 15(15):831–833, 1990. 6

[54] H. Becker, A. Arnold, R. Suntz, P. Monkhouse, J. Wolfrum, R. Maly, and W. Pfister. Investigation of flame structure and burning behaviour in an IC engine simulator by 2D-LIF of OH radicals. *Appl. Phys. B*, 50:473–478, 1990. 6, 99

[55] C. Kittler and A. Dreizler. Cinematographic imaging of hydroxyl radicals in turbulent flames by planar laser-induced fluorescence up to 5 kHz repetition rate. *Appl. Phys. B*, 89:163–166, 2007. 6, 21, 99

[56] J. Nygren, M. Richter, J. Hult, C.F. Kaminski, and M. Aldén. Temporally resolved single-cycle measurements of fuel- and OH-distributions in a spark ignition engine using high speed laser spectroscopy. In *Proceedings of the Fifth International Symposium on Diagnostics and Modeling of Combustion in Internal Combustion Engines (COMODIA)*, pages 572–580, Nagoya, Japan, July 2001. 6, 99

[57] J. Hult, M. Richter, J. Nygren, M. Aldén, A. Hultqvist, M. Christensen, and B. Johansson. Application of a high-repetition-rate laser diagnostic system for single-cycle-resolved imaging in internal combustion engines. *Appl. Optics*, 41(24):5002–5014, 2002. 6, 99

[58] S.H.R. Müller, B. Böhm, M. Gleißner, S. Arndt, and A. Dreizler. Analysis of the temporal flame kernel development in an optically accessible IC engine using high-speed OH-PLIF. *Appl. Phys. B*, 100:447–452, 2010. 6, 99

[59] I. Boxx, C. Heeger, R. Gordon, B. Böhm, M. Aigner, A. Dreizler, and W. Meier. Simultaneous three-component PIV/OH-PLIF measurements of a turbulent lifted, C3H8-Argon jet diffusion flame at 1.5 kHz repetition rate. *Proc. Comb. Inst.*, 32:905–912, 2009. 6

[60] I. Boxx, M. Stöhr, C. Carter, and W. Meier. Sustained multi-kHz flamefront and 3-component velocity-field measurements for the study of turbulent flames. *Appl. Phys. B*, 95:23–29, 2009. 6, 99

[61] W. Meier, I. Boxx, M. Stöhr, and C.D. Carter. Laser-based investigations in gas turbine model combustors. *Exp. Fluids*, 49:865–882, 2010. 6

[62] B. Böhm, D. Geyer, A. Dreizler, K.K. Venkatesan, N.M. Laurendeau, and M.W. Renfro. Simultaneous PIV/PTV/OH PLIF imaging: Conditional flow statistics in partially premixed turbulent opposed jet flames. *Proc. Comb. Inst.*, 31:709–717, 2006. 6, 48

[63] S.A. Filatyev, M.P. Thariyan, R.P. Lucht, and J.P. Gore. Simultaneous stereo particle image velocimetry and double-pulsed planar laser-induced fluorescence of turbulent premixed flames. *Comb. Flame*, 150:201–209, 2007. 6

[64] C.M. Fajardo, J.D. Smith, and V. Sick. PIV, high-speed PLIF and chemiluminescence imaging for near-spark-plug investigations in IC engines. *J. of Physics: Conf. Series*, 45:19–26, 2006. 6

[65] G. Hartung, J. Hult, R. Balachandran, M.R. Mackley, and C.F. Kaminski. Flame front tracking in turbulent lean premixed flames using stereo PIV and time-sequenced planar LIF of OH. *Appl. Phys. B*, 96:843–862, 2009. 6

[66] S. Kaiser and C.M. White. PIV and PLIF to evalute mixture formation in a direct-injection hydrogen-fueled engine. *SAE Paper*, 2008-01-1034, 2008. 6

[67] M. Gleißner. *Analyse von Brennraumströmung, Gemischbildung und Verbrennung am Transparentmotor mit Benzindirekteinspritzung und strahlgeführtem Brennverfahren*. PhD thesis, TU-Darmstadt, 2011. 11, 37, 38, 40, 56, 77, 117

[68] H. Zhao et. al. *Advanced direct injection combustion engine technologies and development. Volume 1: Gasoline and gas engines*. Woodhead Publishing, 2010. 12, 13, 90, 117

[69] H. Bauer. *Gasoline-engine management - Basics and components*. Robert Bosch GmbH, 2001. 12, 13, 117

[70] U. Spicher, H. Kubach, and J.P. Häntsche. Die strahlgeführte Direkteinspritzung als Zukunftskonzept für Ottomotoren. In *MTZ Konferenz Stuttgart*, 2006. 12

[71] R. van Basshuysen and F. Schäfer. *Handbuch Verbrennungsmotor*. Vieweg Verlag, 2002. 14, 18, 19

[72] Prof. Dr.-Ing. M. Bargende. Berechnung und Analyse innermotorischer Vorgänge. Institut für Verbrennungsmotoren und Kraftfahrwesen - Universität Stuttgart, 2011. 14

[73] Prof. Dr.-Ing. G. Hohenberg. Verbrennungskraftmaschinen I und II. Fachgebiet für Verbrennungskraftmaschinen - TU Darmstadt, 2007. 14

[74] H. Eichlseder, M. Klüting, and W.F. Piock. *Der Fahrzeugantrieb - Grundlagen und Technologien des Ottomotors*. Springer Wien New York, 2008. 14

[75] J.H. Spurk and N. Aksel. *Strömungslehre*. Springer New York, 2007. 14

[76] S.B. Pope. *Turbulent Flows*. Cambridge University Press, 2000. 14

[77] H. Tennekes and J.L. Lumley. *A first course in Turbulence*. The MIT Press, 1972. 14, 15

[78] J. Warnatz, U. Maas, and R.W. Dibble. *Combustion*. Springer, 2006. 14, 19, 20

[79] J. Jeong and F. Hussain. On the identification of a vortex. *J. Fluid Mech.*, 285:69–94, 1995. 18

[80] R.J. Adrian, K.T. Christensen, and Z.-C. Liu. Analysis and interpretation of instantaneous turbulent velocity flows. *Exp. Fluids*, 29:275–290, 2000. 18

[81] N. Peters. *Turbulent Combustion*. Cambridge University Press, 2000. 20

[82] J.W. Daily. Laser induced fluorescence spectroscopy in flames. *Prog. Energy. Comb. Sci.*, 23:133–199, 1997. 21, 22, 29, 30, 32, 99

[83] C. Heeger, B. Böhm, I. Boxx, W. Meier, S.F. Ahmed, E. Mastorakos, and A. Dreizler. Planar laser diagnostics at high repetition rates: Acquisition and analysis of transient combustion processes. In *ASME Turbo Expo, Berlin, GT2008-50152*, 2008. 21, 99

[84] M. Raffel, C. Willert, S. Wereley, and J. Kompenhans. *Particle Image Velocimetry*. Springer, 2. edition, 2007. 22, 23, 25, 26, 27, 28, 29, 43, 117

[85] J. Westerweel. *Digital Particle Image Velocimetry*. PhD thesis, Technical University of Delft, 1993. 22, 26

[86] J. Westerweel. Fundamentals of digital particle image velocimetry. *Meas. Sci. Tech.*, 8:1379–1392, 1997. 22

[87] R.D. Keane and R.J. Adrian. Theory of cross-correlation analysis of PIV images. *Appl. Sci. Res.*, 49:191–215, 1992. 22, 25

[88] J. Duncan, T. Bryce, H. Thomsen, D. Dabiri, J.R. Hove, and M. Gharib. An extended study of a generalized digital particle image velocimetry (DPIV) processing technique. *Meas. Sci. Tech.*, 20, 2009. 22

[89] B. Böhm. *Experiments for the Validation of Large Eddy Simulations: Turbulence Flame Interactions in Extinguishing Turbulent Opposed Jet Flames*. PhD thesis, TU-Darmstadt, 2008. 23, 48, 60

[90] A. Melling. Tracer particles and seeding for particle image velocimetry. *Meas. Sci. Tech.*, 8:1406–1416, 1997. 24

[91] M.F. Reeder, J.W. Crafton, J. Estevadeordal, J. DeLapp, C. McNeil, D. Peltier, and T. Reynolds. Clean seeding for flow visualization and velocimetry measurements. *Exp. Fluids*, 48:889–900, 2010. 24

[92] LaVision. *Flowmaster - Product Manual for Davis 7.2*, July 2010. 25, 26, 117

[93] R.E. Altenhofer. *Manual of Photogrammetry*, chapter Rectification, page 457. American Society of Photogrammetry, 1952. 27

[94] M. Pilar Arroyo and K.D. Hinsch. *Particle Image Velocimetry*, chapter Recent developments of PIV towards 3D Measurements, pages 127–154. Springer, 2008. 28

[95] S. Bian, S.L. Ceccio, and J.F. Driscoll. A dual-camera cinematographic PIV measurement system at kilohertz frame rate for high-speed, unsteady flows. *Exp. Fluids*, 48:487–495, 2009. 28

[96] J.A. Mullin and W.J.A. Dahm. Dual-plane stereo particle image velocimetry measurements of velocity gradient tensor fields in turbulent shear flow. II. Experimental results. *Phys. Fluids*, 18(035102):1–27, 2006. 28

[97] C.J. Kähler and J. Kompenhans. Fundamentals of multiple plane stereo particle image velocimetry. *Exp. Fluids*, 29:S70–S77, 2000. 28

[98] F. Pereira, M. Gharib, D. Dabiri, and D. Modarress. Defocusing digital particle image velocimetry: a 3-component 3-dimensional DPIV measurement technique. Application to bubbly flows. *Exp. Fluids*, 29:S078–S084, 2000. 28

[99] A.K. Prasad and K. Jensen. Scheimpflug stereocamera for particle image velocimetry in liquid flows. *Appl. Optics*, 34:7092–7099, 1995. 28, 29

[100] D. Calluaud and L. David. Stereoscopic particle image velocimetry measurements of the flow around a surface-mounted block. *Exp. Fluids*, 36:53–61, 2004. 28

[101] B. Wieneke. Stereo-PIV using self-calibration on particle images. *Exp. Fluids*, 39:267–280, 2005. 28, 41

[102] B. Ganapathisubramani, E.K. Longmire, I. Marusic, and S. Pothos. Dual-plane PIV technique to determine the complete velocity gradient tensor in a turbulent boundary layer. *Exp. Fluids*, 39:222–231, 2005. 28

[103] D.L. Reuss, M. Megerle, and V. Sick. Particle-image velocimetry measurement errors when imaging through a transparent engine cylinder. *Meas. Sci. Tech.*, 13:1029–1035, 2002. 29, 44

[104] H. Huang, D. Dabiri, and M. Gharib. On errors of digital particle image velocimetry. *Meas. Sci. Tech.*, 8:1427–1440, 1997. 29

[105] R. Fei and W. Merzkirch. Investigations of the measurement accuracy of stereo particle image velocimetry. *Exp. Fluids*, 37:559–565, 2004. 29

[106] N.J. Lawson and J. Wu. Three-dimensional particle image velocimetry: experimental error analysis of a digital angular stereoscopic system. *Meas. Sci. Tech.*, 8:1455–1464, 1997. 29

[107] N.J. Lawson and J. Wu. Three-dimensional particle image velocimetry: error analysis of stereoscopic techniques. *Meas. Sci. Tech.*, 8:894–900, 1997. 29

[108] K. Kohse-Höinghaus and J.B. Jeffries. *Applied Combustion Diagnostics*. Taylor and Francis, New York, 2002. 30

[109] Alan C. Eckbreth. *Laser Diagnostics for Combustion Temperature and Species*. Gordon and Breach Publishers, 1996. 30

[110] W. Demtröder. *Molekülphysik*. Oldenburg Verlag, 2003. 31

[111] C. Tropea, J. Foss, and A. Yarin. *Springer Handbook of Experimental Fluid Mechanics*. Springer Verlag, 2007. 31

[112] N. Clemens. *Flow Imaging*, chapter Flow Imaging. John Wiley and Sons, 2002. 33

[113] J. Kristian Sveen. *An introduction to MatPIV v. 1.6.1*. University of Oslo, Dept. of Mathematics, 2004. 48

[114] J. Dyckmans. Personal communication. 49

[115] M. Luong, R. Zhang, C. Schulz, and V. Sick. Toluene laser-induced fluorescence for in-cylinder temperature imaging in internal combustion engines. *Appl. Phys. B*, 91:669–675, 2008. 52

[116] M. Cundy, P. Trunk, A. Dreizler, and V. Sick. Gas-phase toluene LIF temperature imaging near surfaces at 10 kHz. *Exp. Fluids*, pages 1–8, 2011. 52

[117] S.H.R. Müller, S. Arndt, and A. Dreizler. Analysis of the in-cylinder flow field / spray injection interaction within a DISI IC engine using high-speed PIV. *SAE Paper*, 2011-01-1288, 2011. 81

[118] W. Hentschel. Optical diagnostics for combustion process development of direct-injection gasoline engines. *Proc. Comb. Inst.*, 28:1119–1135, 2000. 81

[119] C. Arcoumanis and J.H. Whitelaw. Fluid mechanics of internal combustion engines - a review. *Proc. Inst. Mech. Eng.*, 201:57–74, 1987. 81

[120] S.H.R. Müller, S. Arndt, and A. Dreizler. Investigation of the fuel / air mixture distribution in an internal combustion enine using high-speed laser induced fluorescene. In *5th European Combustion Meeting Cardiff, Wales*, 2011. 90

[121] B.O. Ayoola, R. Balachandran, J.H. Frank, E. Mastorakos, and C.F. Kaminski. Spatially resolved heat release rate measurements in turbulent premixed flames. *Comb. Flame*, 144:1–16, 2006. 99

[122] R. Abu-Gharbieh, G. Hamarneh, T. Gustavsson, and C.F. Kaminski. Flame front tracking by laser induced fluorescence spectroscopy and advanced image analysis. *Optics Exp.*, 8(5):278–287, 2001. 99

[123] M. Konle, F. Kiesewetter, and T. Sattelmayer. Simultaneous high repetition rate PIV-LIF-measurements of CIVB driven flashback. *Exp. Fluids*, 44:529–538, 2008. 99

[124] C. Schneider, A. Dreizler, and J. Janicka. Fluid dynamics analysis of atmospheric reacting and isothermal swirling flows. *Flow, Turbulence and Comb.*, 74:103–127, 2005. 99

List of Figures

Acknowledgments

This thesis is the outcome of roughly three years as a scientific research member at the Institute of Reactive Flows and Diagnostics of the Technische Universität Darmstadt in cooperation with the Robert Bosch GmbH, Gerlingen-Schillerhöhe.

Foremost, I want to thank Prof. Dr. rer. nat. Andreas Dreizler for the fruitful discussions and the motivation during this time. His overall support during the experiments and the encouragement to take part in multiple international conferences is unparalleled. As an expatriate at Robert Bosch GmbH, I am grateful for the trust and freedom he bestowed in me. I would also like to thank Prof. Dr. rer. nat. Volker Sick for not only being interested in my work at conferences, but also being the co-referee of this thesis. Additionally, I want to thank Prof. Dr.-Ing. Johannes Janicka who first employed me in the Sonderforschungsbereich 568.

Of course I would like to thank all my colleagues in Darmstadt, especially Elias Baum, Guido Künne, Benjamin Böhm, and Markus Schmitt. I was glad to help out with experimental data (an abundance of nearly 6 TB) and other numerous rantings. To great lengths I am indebted to Anna Schwarz as she made the final months while writing this thesis feel like a walk in the park. Her perseverance has paid off, more than she knows.

The experimental work could not have been done without the great help of my colleagues at Robert Bosch. Foremost, I want to thank Dr. Stefan Arndt for his formidable support and ever so friendly atmosphere. The two years I spent in the "Ländle" have been a unique experience. Albeit the long hours in the lab, I want to thank Daniel Hertler, Jan Dyckmans, Vinzenz Neubert, Martin Buschbeck, and all the others for ensuring that time flew by.

Finally, this work could not have been done without the great support of my family and friends. Over the years there have been many ups and downs, but I knew I could always count on everyone. For their relentless support I want to thank Maike Dreuth, Billie Graham, Philippa Chegwin, Dierk Erdmann, Leonard Henkes, Bernhard Wahlig and Florian Müller.

Frammersbach, December 2011 Sebastian H. R. Müller

Publications

Journals

S. H. R. MÜLLER, S. ARNDT, A. DREIZLER: *Analysis of the In-Cylinder Flow Field / Spray Injection Interaction within a DISI IC Engine Using High-Speed PIV*, Society of Automotive Engineering, 2011-01-1288

S. H. R. MÜLLER, B. BÖHM, M. GLEISSNER, S. ARNDT, A. DREIZLER: *Analysis of the temporal flame kernel development in an optically accessible IC engine using high-speed OH-PLIF*, Applied Physics B: Laser and Optics, 100 (3), 2010

S. H. R. MÜLLER, B. BÖHM, M. GLEISSNER, R. GRZESZIK, S. ARNDT AND A. DREIZLER: *Flow field measurements in an optically accessible, direct-injection spray-guided internal combustion engine using high-speed PIV*, Experiments in Fluids, Vol. 48, pp. 281-290, 2010

Conferences

S. H. R. MÜLLER, S. ARNDT, A. DREIZLER: *Analysis of the transient flow structures inside an IC engine using high-speed 3C-PIV*, Gordon Research Conference: Laser Diagnostics 2011, Waterville Valley, New Hampshire, USA

S. H. R. MÜLLER, S. ARNDT, A. DREIZLER: *Investigation of the fuel/air mixture distribution in an internal combustion engine using high-speed laser induced fluorescence*, European Combustion Meeting 2011, Cardiff, Great Britain

S. H. R. MÜLLER, S. ARNDT, A. DREIZLER: *Analysis of the In-Cylinder Flow Field / Spray Injection Interaction within a DISI IC Engine Using High-Speed PIV*, Society of Automotive Engineering, SAE 2011 World Congress, Detroit, USA

S. H. R. MÜLLER, S. ARNDT, A. DREIZLER: *Analysis of the in-cylinder flow field/spray interaction in respect of charge motions using high-speed PIV*, X. Int. Conference of Engine Combustion Processes, Munich, 2011

M. GLEISSNER, S. ARNDT, R. GRZESZIK, T. LINDEMANN, A. DREIZLER, B. BÖHM, S. H. R. MÜLLER: *Analyse der Brennraumströmung eines direkteinspritzenden Ottomotors mittels Hochgeschwindigkeits-Particle Image Velocimetry - Auswirkung auf Gemischbildung und Verbrennung*, 9th Int. Conference of Engine Combustion Processes, Munich, 2009

S. H. R. MÜLLER, B. BÖHM, C. HEEGER, A. DREIZLER: *Advanced diagnostics in turbulent reactive flows*, Conference of Turbulence, Heat and Mass Transfer 6, Rome, 2009